이학석사학위논문

Raman Spectroscopy Study on the Graphene Induced Surface Reconstruction

그래핀에 의해 유도된 표면 재구성에 대한 라만 분광 연구

2015 년 8 월

서울대학교 대학원

화학부 물리화학 전공

강 진 현

M. S. Thesis

Raman Spectroscopy Study on the Graphene Induced Surface Reconstruction

Advisor: Prof. Byung Hee Hong

Major: Physical Chemistry

Jin Hyoun Kang

Department of Chemistry

Graduate School of Seoul National University

August 2015

Abstract

Jin Hyoun Kang
Department of Chemistry
The Graduate School of Seoul National University

The surface morphology of copper (Cu) often changes during graphene synthesis by chemical vapor deposition (CVD); the change is attributed to the thermal expansion coefficient mismatch between graphene and Cu. However, the obvious relationship between the reconstructed Cu surface and graphene is not totally understood yet. Here we synthesized graphene with different layer numbers using a CVD system by controlling the gas flow and time. Atomic force microscopy (AFM) images and the Raman G and 2D peaks show that Cu step edges became noticeably broader with increasing graphene layer number. Furthermore, $\Delta\omega\_G–\Delta\omega\_2D$ plot indicates that the biaxial compressive strain on monolayer graphene was higher than that on bi/trilayer graphene, which agrees overall with topographic AFM images. Our results suggest that stress relaxation from the less strained bi/trilayer graphene crucially affects Cu surface reconstruction.

Keywords: Graphene, Surface reconstruction, Atomic force microscopy, Raman spectroscopy

Student number: 2013-20251

Contents

Chapter 1. Introduction

Chapter 2. Synthesis of Graphene on Cu Foil and Morphology Evolution

Chapter 3. Raman Spectroscopy Study

List of Figures

Chapter 1

Chapter 2

List of Tables and Scheme

Chapter 3

Chapter 1

Introduction

1.1 Brief Introduction of Graphene

Graphene is composed of carbon atoms in 2-dimensional honeycomb structure. Graphene is distinct with graphite, because the partial overlaps between interlayer π-orbitals are absence in graphene. In the view as a chemist, graphene resembles the polyaromatic hydrocarbons with infinite number of interconnected rings. By applying the secular determinants with Hückel approximation resembled with tight-binding approximation in physics, the energy level of π-electronic system could be obtained. To consider lattice symmetry, we need to introduce the tight-binding approach.

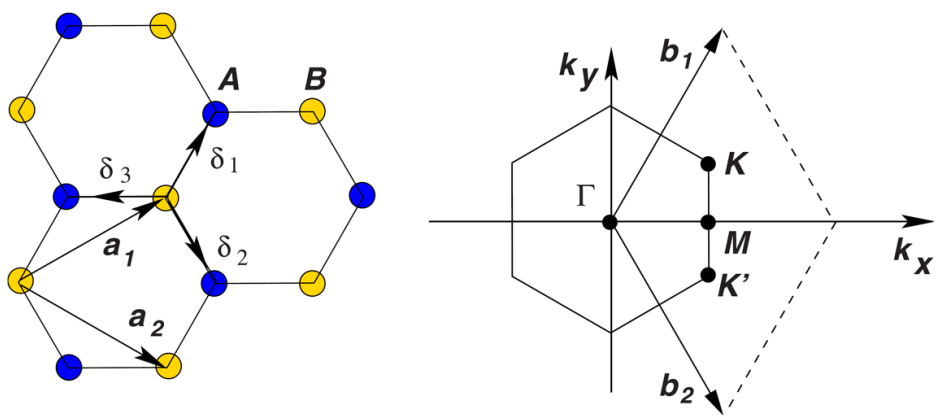

Figure 1 Honeycomb lattice and its reciprocal lattice (first Brillouin zone). The image was adapted from Neto [1].

The honeycomb lattice structure of graphene is triangular lattice with two-atom basis (left, Figure 1)[1]. The lattice vectors and reciprocal vectors are written

as

$$\boldsymbol{a}_1 = \frac{a}{2}(3, \sqrt{3}), \qquad \boldsymbol{a}_2 = \frac{a}{2}(3, -\sqrt{3})$$

$$\boldsymbol{b}_1 = \frac{2\pi}{3a}(1, \sqrt{3}), \qquad \boldsymbol{b}_2 = \frac{2\pi}{3a}(1, -\sqrt{3})$$

where $a =$ 1.42 Å. The corner of the first Brillouin zone of graphene labeled as *K* and *K′*, are specified

$$\boldsymbol{K} = \left(\frac{2\pi}{3a}, \frac{2\pi}{3\sqrt{3}a}\right), \qquad \boldsymbol{K}' = \left(\frac{2\pi}{3a}, -\frac{2\pi}{3\sqrt{3}a}\right)$$

The Hamiltonian for tight-binding model considers the electron hoping to the nearest neighbor atoms (similar to Hückel approximation). If the electron is hopping from *A* site, the nearest atom is located at *B* site. Thus tight-binding Hamiltonian can be expressed simply as[2]

$$H = -t \sum_{\langle i,j \rangle, \sigma} (a^{\dagger}_{\sigma,i} b^{\dagger}_{\sigma,j} + \text{H. c.})$$

where $a_{\sigma,i}$ is annihilation operator for electron with spin configuration σ, and *t* is the nearest neighbor hopping energy. The eigenfunction of the Hamiltonian is Bloch function, and the energy can be obtained by applying the Hamiltonian on eigenfunction. However, rather than, solving the secular equation would give similar result intuitively. The secular equation expressed with tight-binding Hamiltonian *H*, eigenvalue *E*, and overlap matrix *S* is,

$$\begin{vmatrix} H_{AA}(\boldsymbol{k}) - E(\boldsymbol{k}) S_{AA}(\boldsymbol{k}) & H_{AB}(\boldsymbol{k}) - E(\boldsymbol{k}) S_{AB}(\boldsymbol{k}) \\ H^*_{AB}(\boldsymbol{k}) - E(\boldsymbol{k}) S^*_{AB}(\boldsymbol{k}) & H_{AA}(\boldsymbol{k}) - E(\boldsymbol{k}) S_{AA}(\boldsymbol{k}) \end{vmatrix} = 0$$

If the Hamiltonian only considers the nearest neighbor interaction, the electron hopping is only allowed for $A \rightarrow B$ or the reverse. Then the diagonal component of Hamiltonian is [3],

$$H_{AA} = \frac{1}{N}\sum_{\boldsymbol{R}_A}\sum_{\boldsymbol{R}_{A'}} e^{ik(\boldsymbol{R}_{A'}-\boldsymbol{R}_A)}\langle\varphi_A(r-\boldsymbol{R}_A)|H|\varphi_A(r-\boldsymbol{R}_{A'})\rangle$$

$$= \frac{1}{N}\sum_{\boldsymbol{R}_A}\langle\varphi_A(r-\boldsymbol{R}_A)|H|\varphi_A(r-\boldsymbol{R}_A)\rangle = \varepsilon_{2p}$$

giving orbital energy of remaining $2p_z$ orbital. Similarly, from the lattice site *A*, the nearest neighbors *B* lattice sites are separated with vectors (Fig. 1),

$$\boldsymbol{\delta}_1 = a\left(\frac{1}{2},\frac{\sqrt{3}}{2}\right) \quad \boldsymbol{\delta}_2 = a\left(\frac{1}{2},\frac{\sqrt{3}}{2}\right) \quad \boldsymbol{\delta}_3 = a\left(\frac{1}{2},\frac{\sqrt{3}}{2}\right)$$

The interaction between the nearest atoms is [3],

$$H_{AB} = \frac{1}{N}\sum_{\boldsymbol{R}_A}\sum_{\boldsymbol{R}_B} e^{ik(\boldsymbol{R}_B-\boldsymbol{R}_A)}\langle\varphi_A(r-\boldsymbol{R}_A)|H|\varphi_B(r-\boldsymbol{R}_B)\rangle$$

$$= \sum_j e^{ik\boldsymbol{\delta}_j}\langle\varphi_A(r-\boldsymbol{R}_A)\big|H\big|\varphi_B\big(r-\boldsymbol{R}_A-\boldsymbol{\delta}_j\big)\rangle = \gamma_0(e^{ik\boldsymbol{\delta}_1}+e^{ik\boldsymbol{\delta}_2}+e^{ik\boldsymbol{\delta}_3})$$

$$S_{AB} = \frac{1}{N}\sum_{\boldsymbol{R}_A}\sum_{\boldsymbol{R}_B} e^{ik(\boldsymbol{R}_B-\boldsymbol{R}_A)}\langle\varphi_A(r-\boldsymbol{R}_A)|\varphi_B(r-\boldsymbol{R}_B)\rangle$$

$$= \sum_j e^{ik\boldsymbol{\delta}_j}\langle\varphi_A(r-\boldsymbol{R}_A)\big|\varphi_B\big(r-\boldsymbol{R}_A-\boldsymbol{\delta}_j\big)\rangle = s_0(e^{ik\boldsymbol{\delta}_1}+e^{ik\boldsymbol{\delta}_2}+e^{ik\boldsymbol{\delta}_3})$$

Then we can obtain energy by solving secular equation with defined components

$$E_{\pm}(\boldsymbol{k}) = \frac{\varepsilon_{2p} \mp \gamma_0\sqrt{f(\boldsymbol{k})}}{1 \mp s_0\sqrt{f(\boldsymbol{k})}}$$

where

$$f(\boldsymbol{k}) = 3 + 2\cos \boldsymbol{k} \cdot \boldsymbol{a}_1 + 2\cos \boldsymbol{k} \cdot \boldsymbol{a}_2 + 2\cos \boldsymbol{k} \cdot (\boldsymbol{a}_1 - \boldsymbol{a}_2)$$

If we express the vector $\boldsymbol{k}$ as $\boldsymbol{k} = \boldsymbol{K} + \boldsymbol{q}$, for small $\boldsymbol{q}$,

$$E_{+}(\boldsymbol{k}) \approx E_{-}(\boldsymbol{k})$$

Therefore, intrinsic graphene with tight-binding assumption has zero band gap energy. More explicitly, energy band structure around $\boldsymbol{K}$ point is [4],

$$E_{\pm}(\boldsymbol{q}) \approx \pm v_F|\boldsymbol{q}|$$

where v_F is Fermi velocity. The entire energy band can be derived by the similar method, and can be visualized as Figure 2 [1].

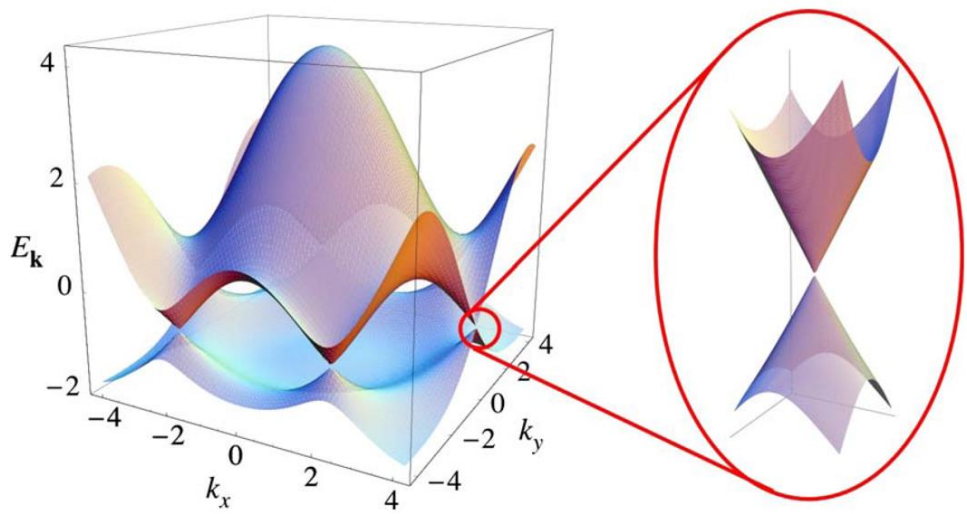

Figure 2 Schematic energy band diagram of graphene. The image was adapted from Neto [1].

1.2 Synthesis of Graphene

For electronic application, high quality graphene should be prepared by scalable method. The mechanical exfoliation of graphene from graphite produces a superior quality graphene, but the size is limited to micrometer [5]. Large scale graphene was first grown by using silicon carbide (SiC) substrate. The graphene can be epitaxially grown on Si-terminated (0001) face by successive annealing process at high temperature up to 1450℃ [6]. However, strong interaction between SiC surface and graphene introduces large density of the defects [7].

Graphene can be prepared using metal substrate through the thermal decomposition of hydrocarbons or surface segregation of carbon atoms. Graphene has been synthesized on various metals, such as Co[8], Ni[9-11], Pt[12-14], Pd[15], Ru[16-18], Ir[19-21], or Cu [22]. Among these, the polycrystalline Ni and Cu have triggered the industrial interests in these days due to the low cost and scalable production. The graphene deposition on Ni have been successfully prepared, but the main limitation of the utilizing Ni is the layer controllability. The fundamental mechanism of graphene growth on Ni substrate has been explained that the carbon segregation on the surface from bulk during cooling, owing to the stable formation of the Ni-C solution at the high temperature. Therefore rapid segregation of the carbon partially limits the layer control. On the contrary, the uniform high quality single layered graphene have been prepared on polycrystalline Cu [22]. This is due to the different mechanism of the graphene deposition, so the large area of the graphene can be prepared with layer number control. In addition, the thin copper

foil can be easily etched by chemicals, so graphene can be transferred onto desired substrates.

Graphene deposition on copper involves the decomposition of carbon precursor on a copper substrate typically held at high temperature usually up to 1000℃. The carbon precursor can be gas phase such as methane, ethylene, and acetylene, or liquid precursor such as hexane [23]. Schematically, the whole process can be divided as annealing, growth, and cooling step. The residual copper oxide on copper foil is removed at high temperature treatment under hydrogen atmosphere, and the average grain size of Cu is increased in the annealing step (Figure 3). When carbon precursor is collided on the catalysts, it is catalytically decomposed in active carbon which can be attached with other active carbon. This active carbon diffuses on surface, and successive collision with other active carbon grows the graphene lattice (Figure 3d). After the thermal quenching, the graphene can be visualized by the microscopy (Figure 3e), and finally can be transferred to the desired substrates.

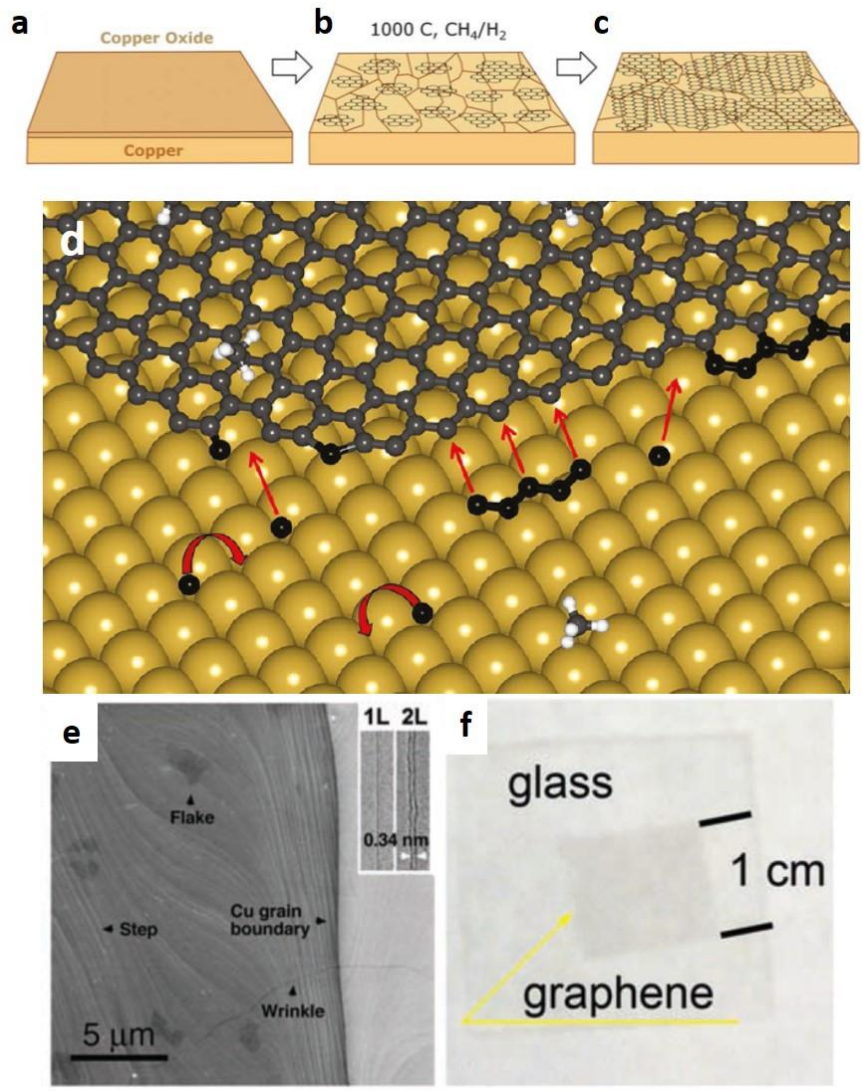

Figure 3 The overview of the graphene deposition on Cu. a-c. Schematic process of the chemical vapor deposition (CVD) of graphene. d. Schematic illustration of the graphene growth. e. Scanning electron microscope (SEM) image of the graphene grown on polycrystalline Cu foil. f. Photo of the graphene transferred on the glass substrate. The images were adapted from [22].

1.3 Interaction between Graphene and Metal substrate

1.3.1 Adsorption and charge transfer of graphene on metal

In many experimental situation, the graphene is placed on the substrate owing to the thin film structure. The atomic and the molecular impurities can induces the change of the electronic properties on the graphene sheet. The properties of the interface between graphene and the metals has been systematically investigated. For example, the transport phenomena was changed with the contact materials due to the work function difference between the graphene and metal contact, which induces the Schottky contact. The weak adsorption of graphene on Al, Ag, Cu, Au, and Pt preserves the band structure of graphene, but in contrast, the strong chemisorption of graphene on Ti, Ni, Co, Pd surfaces perturbs the electronic structure of graphene [24-30].

1.3.2. Surface Reconstruction of Metal Surfaces induced by Graphene

The transferred graphene grown on metal substrate has show the wrinkles which has height and width of several nanometer scale [31-33]. These corrugation of wrinkles strongly influences the properties of the graphene [34]. Although the origin of the wrinkles of graphene grown by CVD technique is not fully understood yet, but the compressive stress during cooling owing to the difference of the thermal expansion coefficients between graphene and metals has been regarded as a main cause of the wrinkle formation [35]. The thermal annealing of graphene sample grown on Cu surface at 400℃ in the ultrahigh vacuum (UHV) condition

induces the surface reconstruction of the Cu [36]. The authors suggested that the residual stress during cooling step after growth is released by the Cu surface atom reconstruction at the annealing, so the periodic stripe pattern was observed.

The direct observations of the wrinkle formation of graphene on Cu have been reported recently [37-40]. The detailed surface topology measured by atomic force microscope (AFM) and scanning electron microscope (SEM) revealed the periodic wrinkles were formed after the CVD synthesis of graphene on Cu foil, which is the result of the Cu step construction in graphene/Cu system [38-40]. The Cu step bunching in the graphene grown system shows significantly different surface morphology, while the Cu annealed at same temperature and cooled with same cooling rate without deposited graphene showed the smooth and flat surface [37]. The periodically formed wrinkle-like Cu step and the thermally induced graphene wrinkle which is non-parallel to the Cu step were suggested as origin of the wrinkle of graphene after transfer [39,40]. However, the mechanism of the wrinkle-like Cu step formation is not fully revealed.

Recently, several groups reported the wrinkle-like structure formation of the Cu step. The vermicular ripple formation was observed by Paronyan *et al.*, which suggests the instability of the dilute Cu-C phase during cooling starts from high temperature is the origin of the ripple-like Cu step bunches formation [41]. In addition, the grain-dependent surface step formation was observed by Kim *et al.*, who suggest that the strain relaxation between graphene and the Cu lattice induces the Cu step [42]. Considering these results, copper surface morphology would be

reconstructed by the minimizing the entire energy of the graphene-copper interface. Although surface reconstruction has been regarded to occur during cooling stage, but in recent, the surface reconstruction of graphene/Cu was directly observed by Wang *et al*. using *in situ* environmental scanning electron microscope (ESEM) [43]. The direct observation by ESEM shows the surface reconstruction of copper occurred at the temperature range of 750℃ to 520℃.

1.4 Raman Spectroscopy of Graphene

Interest in studying the fundamental properties of graphene has grown in recent years since the discovery of method to identify the structure of graphene. Raman spectroscopy in graphene has been investigated thoroughly, and as a results, the structural information and behavior of electrons and phonons in graphene can be characterized by the simple method.

The interaction between the electron-hole pair and the phonon in graphene has critical role for Raman scattering in graphene. To understand the mechanism of the Raman scattering, the phonon dispersion of graphene is essential. The unit cell of monolayer graphene contains two distinct carbon atoms, thus there are six phonon dispersion bands (Figure 4). Each phonon branch is assigned as in-plane (i) or out-of-plane (o), transverse (T) or longitudinal (L), acoustic (A) or optic (O). The Raman active modes for the planar graphene are the in-plane iTO and iLO modes, which are degenerate at the zone center (Γ). The phonon modes around the *K* are important, because the resonant Raman bands in graphene are related to

phonon modes around at *K* point [44].

The characteristic features in the Raman spectra of monolayer graphene are the *G* band located at around 1580 cm^{-1} and the 2*D* band located at about 2700 cm^{-1}. In the case of the disrupted samples with defects, the *D* band which has half of frequency of the 2*D* band (~1350 cm^{-1}) is activated (Figure 5). Each of the band is related to the different phonon modes. The *G* band is associated with the doubly degenerate phonon mode at the Brillouin zone center [44]. On the other hand, *D* and 2*D* bands are originated from a second-order process, involving two iTO phonons near the *K* point for the *2D* band or one iTO phonon and one defect in the case of the *D* band. Each process can be schematically expressed as Figure 6. In a pristine graphene without defect, the *G* and the 2*D* bands are only measurable, since the 2*D* bands can be activated without defect owing to the two iTO phonons only responsible for the scattering process [45].

The Raman process can also occur by scattering of holes. In graphene with imbalanced electron-hole density, the triple resonance condition can be achieved. The electron-hole excitation followed by the phonon scattering by both electron and holes, and finally recombination between electron and hole can also activate the 2*D* band [46] (Figure 6b bottom). The triple resonance condition might explain why the 2*D* band is more intense than the *G* band in monolayer graphene [44].

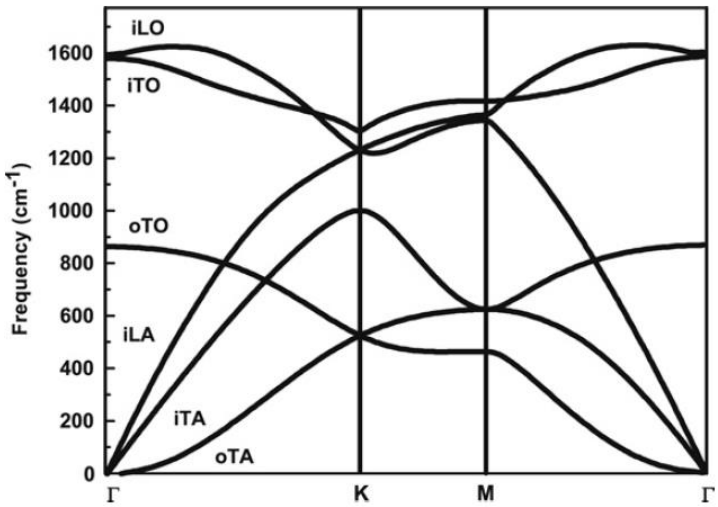

Figure 4 Calculated phonon dispersion relation of graphene. The image is adapted from the Malard *et al*. [44].

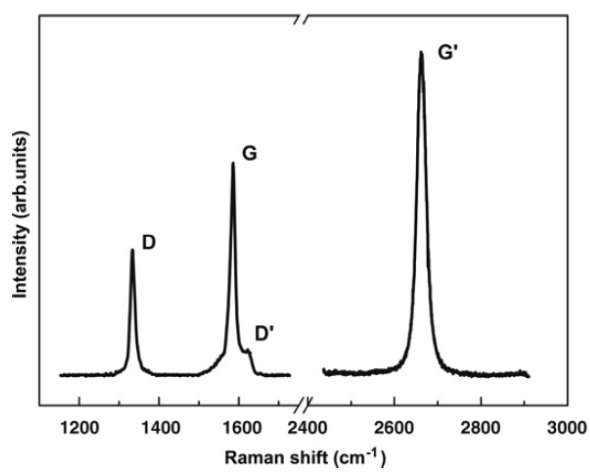

Figure 5 Characteristic Raman spectrum of a defected graphene. The spectrum was collected at the graphene edge, which has defects in lattice. The image is adapted from the Malard *et al*. [44].

1.4.1. Characterizing the number of layers

The structure information of the graphene can be investigated by the Raman spectroscopy. Starting from the monolayer graphene, the double resonance process of the monolayer graphene (Figure 6b) activates the 2*D* band of the graphene. In defect-free pristine graphene, the double resonance and the triple resonance process of the 2*D* band shows larger peak of 2*D* band than G peak, and *D* peak is not activated due to absence of the defect (Figure 7, top).

In the case of bilayer graphene, the structural difference changes the Raman scattering process. The electronic band structure of the bilayer graphene is composed of the parabolic bands, the two conduction bands and two valence bands (Figure 7, bottom). The interlayer interaction affects the electron motion, so the band split into symmetric and anti-symmetric components. As a result, the double resonance conditions are more complex than that of monolayer graphene. The schematic illustration of the double resonance process in bilayer graphene is showed in Figure 7. Owing to the split of the electronic bands, the double resonance process split into four modes. These four different process contributes each modes with different frequency, thus the 2*D* band of the bilayer graphene is composed of four peaks, which can be deconvoluted by the Lorentzian function [47].

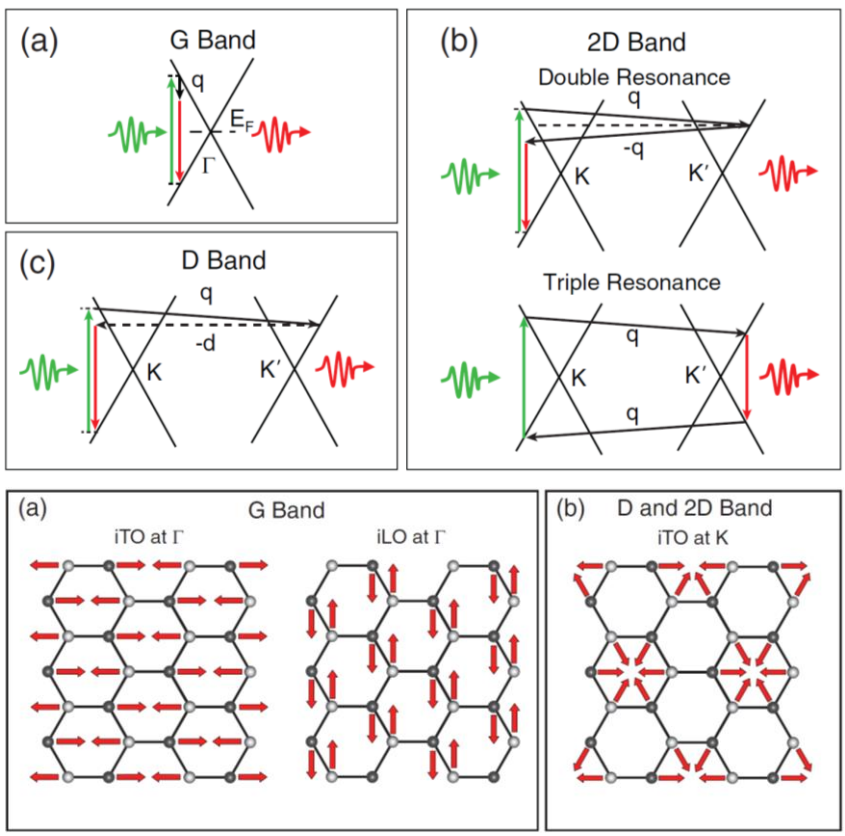

Figure 6 Schematic illustration of the Raman scattering process. a-c. the Raman process of the *G*, *2D*, and the *D* bands. (bottom) a-b. the schematic vibration modes of each band. The image is adapted from the Beams *et al*. [45].

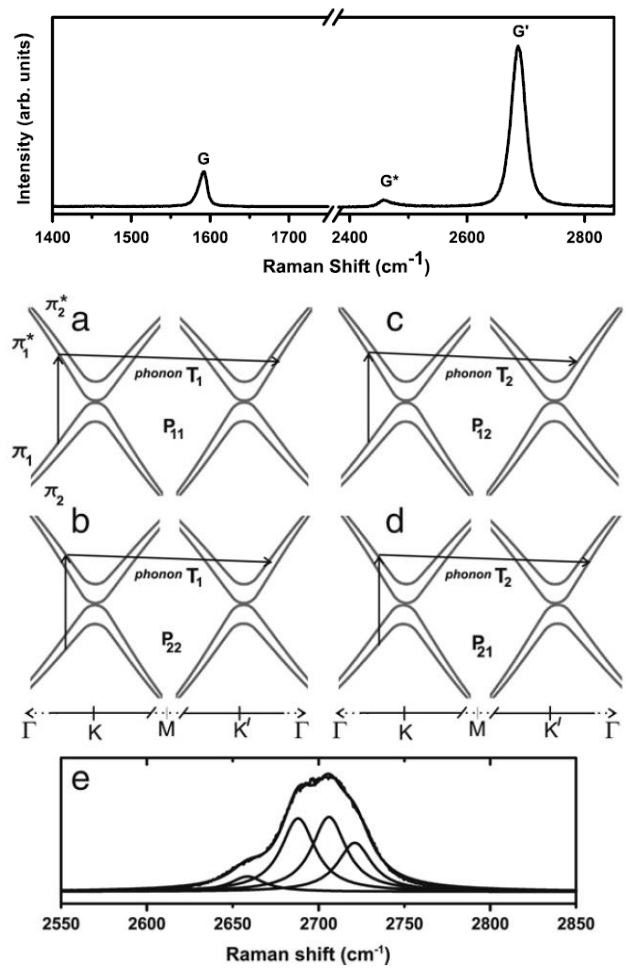

Figure 7 The spectrum of pristine monolayer graphene, and schematic illustration of the double resonance Raman process of bilayer graphene. (upper) The spectrum of defect-free monolayer graphene. (bottom) a-d. Double resonance process of bilayer graphene. e. Raman spectrum of 2*D* band of bilayer graphene. The image is adapted from the Malard *et al*. [44].

1.4.2. Estimation of charge doping on graphene

Graphene is sensitive to changes in carrier concentration owing to the linear electronic dispersion of the band structure. The doping level in graphene can be characterized by Raman spectroscopy. The G and 2D bands are both strongly depends on the carrier concentration of graphene.

The position and the width of the G band change with doping level. When the Fermi level is shifted from the origin, two effects are occurred. First, the Fermi level upshift/downshift changes the equilibrium constant, which induces the phonon stiffening and softening [48]. The second effect is related to the Kohn anomaly at the zone center of Brillouin zone in the phonon dispersion [49]. Increasing Fermi level reduces the number of electronic states that are available as decay pathways due to the Pauli exclusion principle, thus the result makes linewidth of the G band narrow [50]. The experimental demonstration by electric field effect doping clearly showed the dependence of the position and the FWHM of the G peak (Figure 8). Both electron and hole doping, the position of the G peak was upshifted, and the FWHM decreases with the increase of the carrier concentration [50].

The position of the 2D band also depends on the Fermi level. As well as the G band, the phonon stiffening/softening makes the change in the position of 2D band. The 2D band is increased for both electron and hole concentration increases, but 2D band goes soften and frequency decreased at the high electron density (Figure 8c).

In addition to the width and the position of the bands, the relative intensity of the G to 2D bands also changes. At low doping levels the G band intensity is independent of Fermi level, while the 2D band intensity decreases as Fermi level increases [51]. Since all the intermediate states of the 2D band are resonant with electronic levels, the intensity is sensitive to electron-phonon coupling [51]. Therefore, by tuning Fermi level and measuring the intensity of the 2D band, the electron-phonon scattering rate can be determined [52]. It will be discussed in more detail in chapter 3.

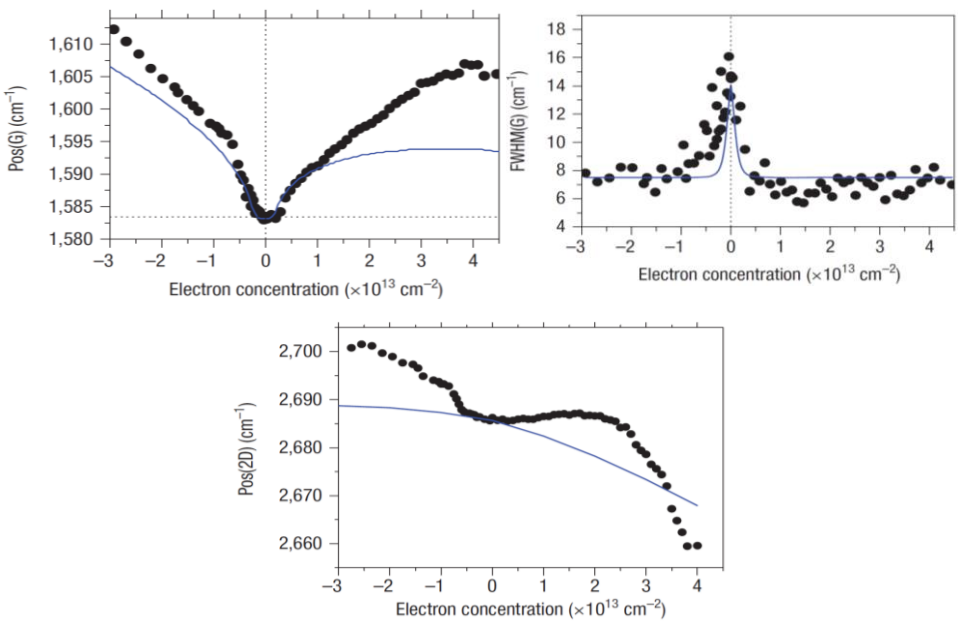

Figure 8 The position and the FWHM of the peaks to the carrier concentration. a. position and the b. FWHM of the G peak. c. position of the 2D peak. The image is adapted from the Das *et al*. [50].

Chapter 2

Synthesis of Graphene on Cu Foil and Morphology Evolution

2.1 Synthesis of graphene on Cu foil

Graphene was synthesized by CVD method using Cu foil as a catalytic substrate. The rolled Cu foil has high purity (99.9%) with dilute concentration of residual metals such as Fe, Ti, Sn, Mo, Sb, Ag. The total concentration of residual metals was under 700 ppm. The Cu foil was used as received without any treatment. The Cu foil was placed in quartz tube, and the chamber was under vacuum with background pressure under 2.3×10^{-4} Torr which is the lower bound of the pressure gauge. After that, hydrogen gas was introduced with flow rate of 5 sccm, and chamber pressure was constantly kept at 42 mTorr. The temperature of the chamber was linearly increased with programmed furnace in 1h. At the high temperature under hydrogen atmosphere reduces the residual oxide on Cu surface and grows average grain size of the Cu. The programmed final temperature of the furnace at the annealing step was 1000℃, and was kept during the growth step. After the annealing step, the flow rates of the hydrogen and the methane were 5 sccm and 35 sccm at total pressure of 5.4×10^{-1} Torr , which correspond to hydrogen partial pressure of 68 mTorr and methane partial pressure of 473 mTorr. The temperature and the flow rates were kept constant for 30 min to ensure the full growth of graphene. After the growth step, the methane flow was terminated and the furnace was slid to the other side of the chamber to cool Cu foil rapidly. The temperature and the gas composition was summarized in Figure 9.

The temperature of the chamber was measured by thermocouple. The temperature outside of the chamber was 1000℃ as we programmed, but the temperature was

about 70℃ lower at the inside of the chamber. This is because our system has large diameter of chamber, so heat loss was significant. Although the temperature significantly deviates to position, the temperature was stable ~935℃ at the center of the furnace (Figure 10a). Therefore, the Cu foil was strictly placed at the center of the furnace. The cooling rate was also measured with thermocouple, and the half of the growth temperature was reached within ~ 5 min (Figure 10b).

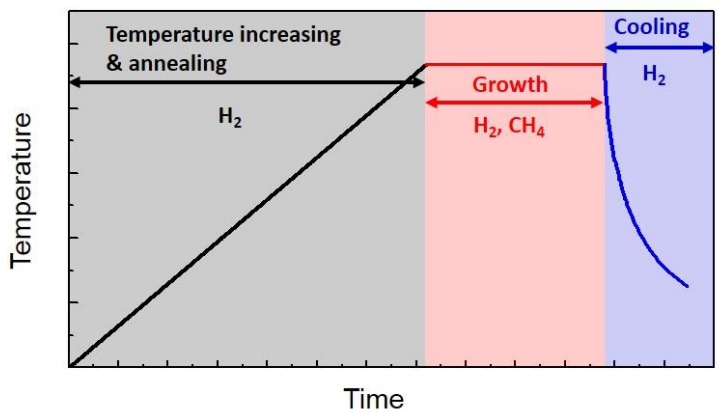

Figure 9 The temperature profile and gas composition at the annealing, growth, and the cooling step of the CVD process. Time and the temperature are expressed in arbitrary unit.

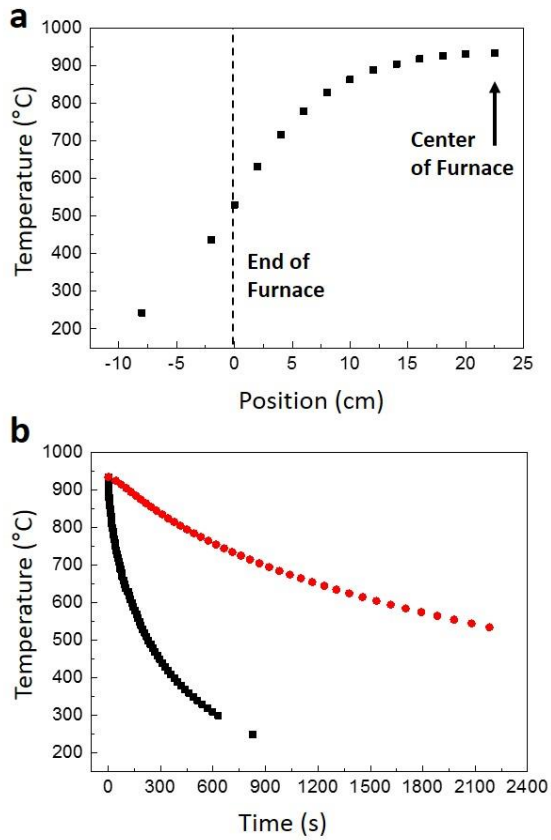

Figure 10 The temperature variation to the position and the cooling profile. a. Temperature variation was measured by thermocouple inside the chamber. At the center of the furnace, about 10 cm of the zone shows low temperature variation. b. Cooling profile of the rapidly cooled case (black dot) and the slowly cooled case (red dot).

2.2 Morphology change of the Cu foil

After the graphene synthesis, the Cu foil was shinier and softer than the untreated bare Cu foil observed with naked eye. The optical microscope images show the surface of the Cu foil has significantly changed after the graphene synthesis (Figure 11). The optical microscope image of bare Cu foil showed rolling mark and invisible grain. On the contrary, the optical microscope image of graphene grown Cu foil clearly showed enlarged Cu grain which size is up to ~ 100 μm separated by grain boundary. This is the result of the high temperature at the annealing and growth step which proceeds Cu recrystallization [37]. At the high magnification, the detailed microstructure of the Cu surface was visualized. Under the dark field microscope, the distinct feature was observed in the 4-fold shaped region (Figure 12). The size of each 4-fold shaped region was about 5 μm, and the wave-like structure was inferred by the image. The dark field optical microscope image of other sample grown in similar condition clearly confirms the wave-like structure in the 4-fold shaped region (Figure 12c). The shape of the 4-fold region is similar to the shape of the graphene islands grown in low pressure condition [53,54], so these regions might be covered with the bilayer graphene, which will be thoroughly discussed later.

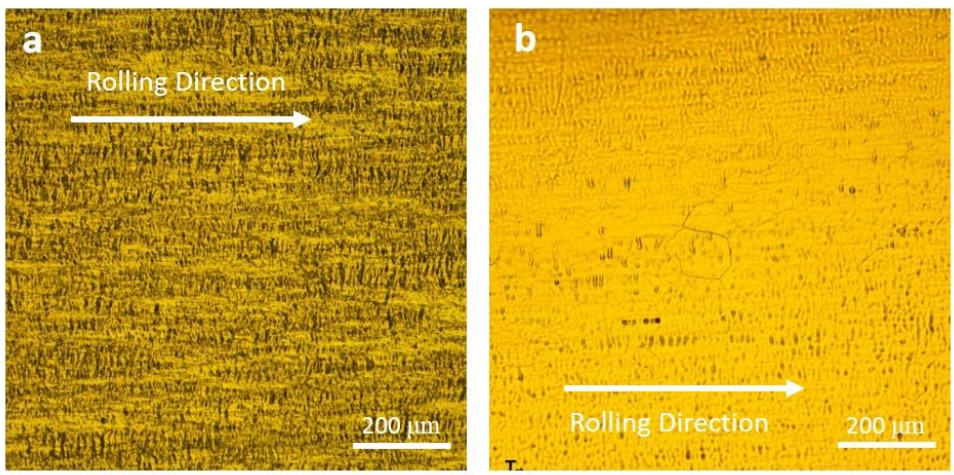

Figure 11 Optical microscope images of bare Cu foil and graphene grown Cu foil at low magnification. Optical microscope image of the a. bare Cu and b. graphene grown Cu. The direction of the rolling mark is expressed in figures.

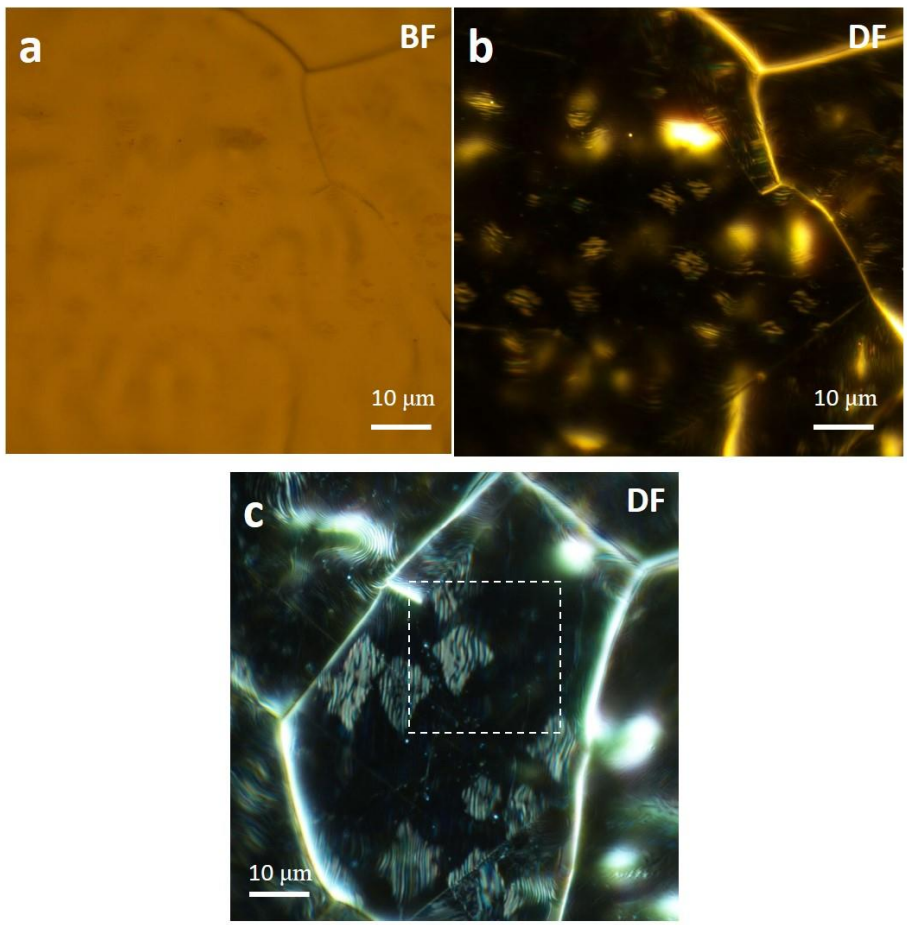

Figure 12 Optical microscope images of the graphene grown Cu surface at high magnification. a. Bright field image and b. dark field image of the graphene grown sample. c. The dark field image of the sample grown in other batch.

2.3 Atomic force microscopy

To investigate the morphology of the Cu surface more precisely, surface was imaged by atomic force microscopy (AFM). All images were taken by non-contact mode (XEI-100, Park System) using silicon nitride tip.

To ensure the feature observed by the optical microscope is due to morphology of the Cu surface, AFM image was taken with large scan size of $35\times35\ \mu m^2$ which is marked as white dashed box in Figure 12c (Figure 13). The topology of the area measured by AFM was exactly same with the image of the dark field microscope. The hills and valleys up to ~ 100 nm was exist which would be the result of the sublimation of Cu, and wave-like structure clearly formed in 4-fold shaped area. The topography and phase image of the smaller scan area showed the difference in background area and 4-fold shaped area (Figure 14). The wave-like structure was formed in both region, but wavelength and the intensity at the 4-fold shaped area was obviously larger than at the background region. The structure was coherently transitioned at the boundary. The wavelength at the 4-fold shaped area was ~ 500 nm and the intensity was ~ 20 nm, which is almost double of the wavelength and intensity at the background (Figure 14e). To give rough intuition, we will introduce the surface area ratio, which is determined as

$$\text{(Surface area ratio)} = [\text{(Surface area)}/\text{(Geometric area)}]\times100\ (\%)$$

The surface area ratio calculated from the Figure 14a was slightly higher inside the 4-fold shaped region (~ 0.75%) than the background region (~ 0.49%). As a result, the surface area of the both region is almost same.

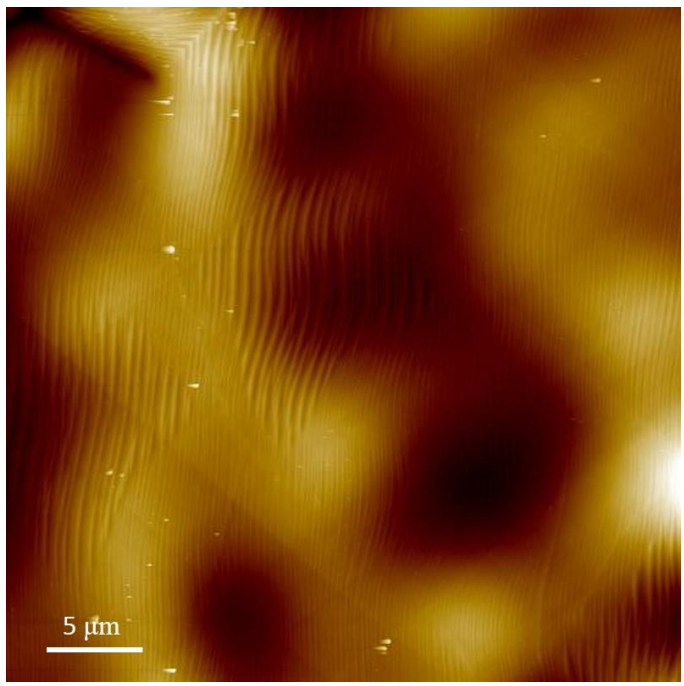

Figure 13 Atomic force microscope (AFM) image of the region which is assigned in Figure 5.

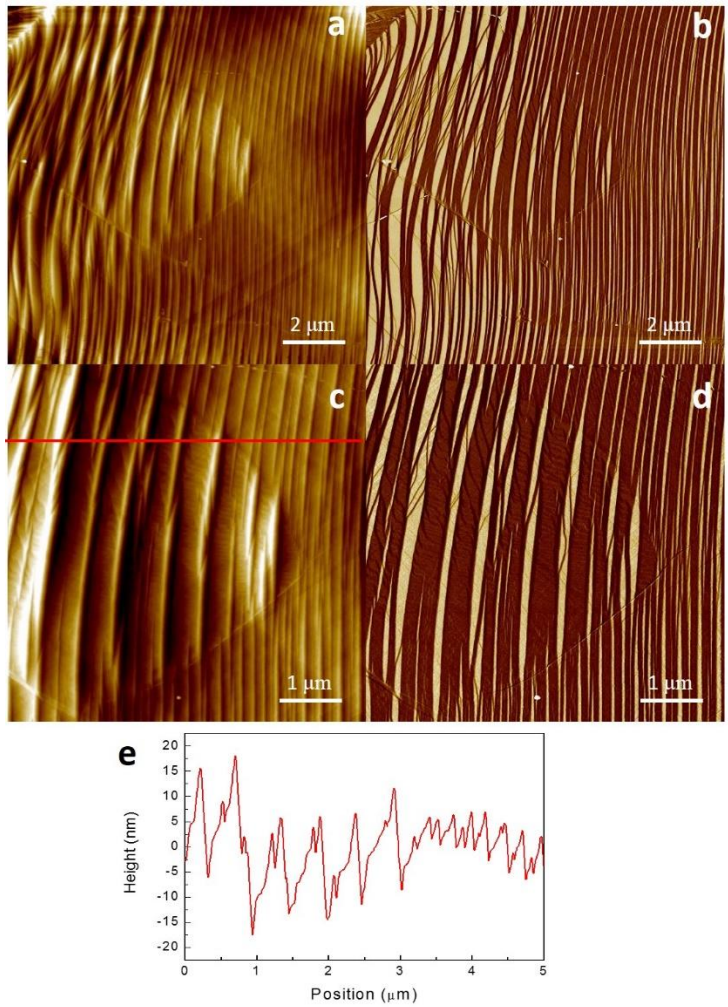

Figure 14 Detailed AFM images of the 4-fold shaped region. a. Topography and b. phase image of the 4-fold shaped region with scan size 10×10 μm^2. c. Topography and d. phase image of the 4-fold shaped region with scan size 5×5 μm^2. The scan rate of all images was 0.5 Hz. e. Line profile of along the red line assigned in c.

2.4 Discussion

The wave-like structure that was mainly observed in our experiments has been reported. In previous reports, the wave-like structure was called ripple or wrinkle, thus we will use these terms to keep coherence with other works. The origin of the ripples of graphene synthesized by CVD method has been observed and explained as several ways. During the annealing of Cu foil and growth of graphene, the temperature inside the chamber is up to 1000℃, which is close to the melting point of the Cu (1084℃). In this high temperature, although bulk copper is not melted, the surface can be pre-melted due to the less bonded unstable surface atoms, resulting thin mobilized Cu film outside of the bulk Cu. In the low pressure under 10^{-3} mbar, the pre-melted Cu film more dominates the surface property, so vaporized or sublimated Cu may change the surface morphology of the Cu. Surprisingly, tendency of the surface reconstruction when graphene was covered on Cu surface is far different than the case of Cu surface uncovered with graphene [36,37,55]. This surface reconstruction of Cu is suggested by the deceleration/pinning of mobile Cu atoms under graphene [36, 55], or the different thermal expansion coefficient between graphene and Cu [37,56]. In addition, the instability on the interface of Cu-C alloy system was also suggested as a responsible factor of the ripple formation [41].

Each of the suggestion may explain the surface reconstruction of Cu under graphene, however, once the graphene film is grown and emerged making entirely connected film, the situation would be little different. When the graphene covered

the entire Cu surface, the fast Cu atoms on surface may be absence because most of the surface Cu atoms interact with graphene. Therefore, the interaction between Cu surface and graphene would be the more important factor for Cu surface morphology evolution. In recent, the surface reconstruction under graphene is observed *in situ* by environmental scanning electron microscope (ESEM) [43]. The *in situ* observation clearly showed that the reconstruction of copper surface is occurred during the cooling step, not during the growth step. This result might confirm the surface reconstruction of Cu is the result of the interaction between graphene and Cu, specifically the stress relaxation due to the lattice mismatch [42]. However, the precise origin of the surface reconstruction seems remained in question yet.

As we used relatively low purity copper than pure copper (99.999%), our system might resemble with the work by Paronyan *et al*. [43] However, although we found that the either vermicular ripple or cell were formed inside several Cu grain similar as the previous report, the transition of wavelength and intensity was clearly occurred in the 4-fold shape region (Figure 15). Therefore, the transition of the wrinkle under the specific area would be the universal phenomena in our system.

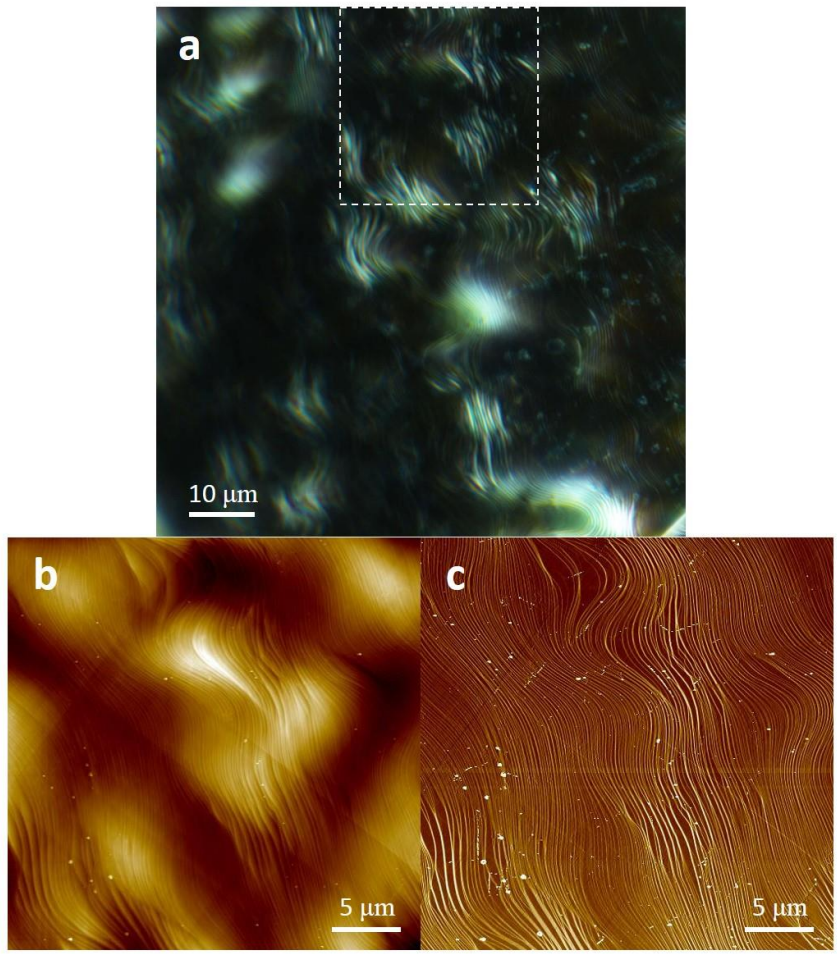

Figure 15 Morphology of Cu at other grain. a. Dark field optical microscope image of the field. The vermicular ripple (wrinkle) was observed in this grain. b. Topography and c. phase image of the area marked in a (white dashed box). The vermicular ripple and the transition of ripple (wrinkle) in the 4-fold shaped region was clearly observed. The scan area of the b and c was 30×30 μm^2, and scan rate was 0.2 Hz.

Chapter 3

Raman Spectroscopy Study

3.1 Characterizing the number of layers of graphene

The Raman spectroscopy is a promising tool for characterizing the graphene as we discussed in the earlier section. The number of the layers of graphene can be determined by two ways. First is the deconvolution of the 2D peak, and second is the comparing the ratio of the intensity of the G peak and the 2D peak. Either methods can determine the number of layers of graphene precisely.

Before the spectrum collection with detailed spatial correlation, the morphology of the field was determined by the optical microscope and AFM. Both bright field and dark field optical microscope images showed the wave-like structure that we found in the earlier section, and the AFM topology image confirms the wrinkle of the surface (Figure 16). The transition of the wrinkle was coherent (Figure 16c), and the line profile shows the wavelength and the intensity was significantly increased at the 4-fold region (Figure 16d). To determine the layer number of the graphene, Raman spectrum was obtained at the each region marked as yellow a, b in Figure 1c. The Raman spectrum was collected with a WITEC confocal spectrometer through X100 objective lens which has numerical aperture of 0.95. The wavelength of the laser was 532 nm (2.43 eV), and laser power was kept under 2 mW to avoid local heating. The spectral resolution was determined by fitting the Rayleigh scattering line to a Gaussian function, and the spectral resolution was 12.6 cm^{-1}. The spectra obtained at a, b show different features with each other (Figure 17). To compare with unstrained, and charge neutral graphene, spectra obtained from the exfoliated graphene on SiO_2 were also

presented in Figure 2 c, d for monolayer and bilayer graphene. The spectrum acquired from the exfoliated monolayer graphene showed intense peak around 2680 cm^{-1}, and single Lorentzian function was fitted (Figure 17c). The FWHM of the peak was about 30 cm^{-1}, which is the well adapted to the undoped monolayer graphene [47]. On the other hand, the spectrum of the exfoliated bilayer graphene showed intense peak around 2700 cm^{-1} with broader FWHM (Figure 17d). This upshifts and broadening of the 2D band is due to the change of the electronic band structure of the bilayer graphene, which splits the 2D peak into 4 components [47]. The peak was well fitted with four Lorentzian peaks and the linewidth of the each peak was around 20~30 cm^{-1} as similar to the result reported previously. The spectrum acquired from the graphene grown graphene, specifically at region a shows similar feature of the exfoliated sample (FWHM ~ 30 cm^{-1}), except the blue shift of the peak. This blue shift of the 2D peak without broadening indicates the phonon stiffening without significant symmetry breaking of the graphene lattice. Therefore, the Raman spectrum clearly indicates the graphene lattice was compressed biaxially [57]. On the other hand, the spectrum acquired at region b shows broaden peak which is clearly split into four Lorentzian peaks, indicating the bilayer structure. The linewidths of the peak were around 20~30 cm^{-1}, similar to mechanically exfoliated bilayer graphene sample. The peak position was located around 2710 cm^{-1}, and four peaks were upshifted around 10 cm^{-1} than exfoliated sample, without significant broadening. Thus, bilayer graphene was also biaxailly compressed. By comparing the frequency and the linewidths of graphene 2D band, the layer number can be determined. In summary, the monolayer graphene is grown

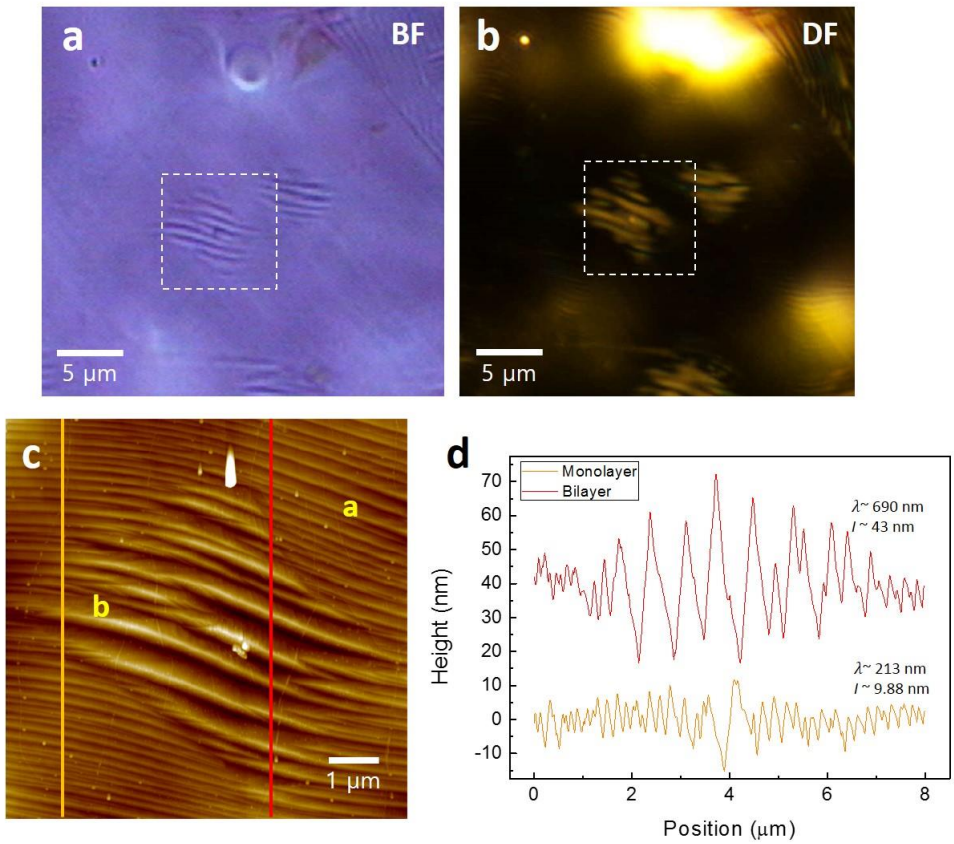

Figure 16 Surface morphology of the field. a. Bright field and b. dark field optical microscope images of the field. c. AFM topology image of the area marked as white dashed box in a and b. the scan size was 8×8 μm^2 and the scan rate was 0.2 Hz. d. Line profiles of the orange and red line in the c.

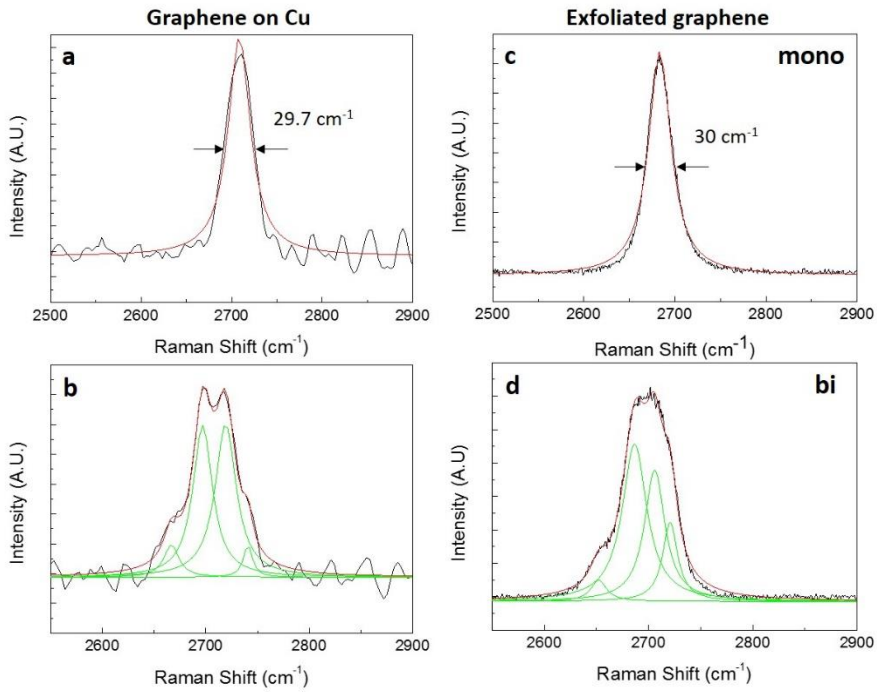

Figure 17 The 2D peak of the graphene on Cu and exfoliated samples. a. b. was collected spectrum at point marked in Figure 1c. The Raman spectrum of a. monolayer and b. bilayer prepared by mechanical exfoliation of graphite. The source wavelength was 532 nm.

in region a and the bilayer graphene is grown in region b in the Figure 1c. In this stage, we can find that the surface geometry and the layer number of the graphene should be closely related to each other.

To determine the geometry of the graphene, spectrum was obtained with exact spatial coordinate using microstage. The spectra were obtained in white dashed box shown in Figure 18 a, b. Acquired spectra were fitted with Lorentzian to precisely determine the position, intensity and FWHM of the peaks. After the data processing, the Raman map was plotted for the FWHM of the 2D peak (Figure 18c), and the intensity ratio I(G)/I(2D) (Figure 18d). Because either the FWHM of the 2D peak and I(G)/I(2D) is sensitive to the number of layers, the number of layers of graphene can be determined with these factors. The FWHM of the 2D peak at narrow wrinkle region (a in Figure 16c) is distributed around 30 cm^{-1}, and the FWHM of the 2D peak at wider wrinkle region (b in Figure 16c) is distributed around 48 cm^{-1} (Figure 18c). The value is well matched with FWHM(2D) of monolayer graphene (~ 30 cm^{-1}) and the bilayer graphene (~ 50 cm^{-1}) by fitting of single Lorentzian function. The Raman map gives distinctive feature of the FWHM(2D) change, and the shape of the Raman map is closely correlated with the shape observed by optical microscopy and AFM. Therefore, the region a, b in Figure 16 are revealed as monolayer and bilayer graphene as we first studied by point spectrum. In addition, there are FWHM up to 60 cm^{-1} in the center of the bilayer graphene. This would indicate the existence of the graphene with number of layers over three, due to additional 2D modes than bilayer graphene. On the other hand, the intensity ratio I(G)/I(2D) was also gradually increased in monolayer

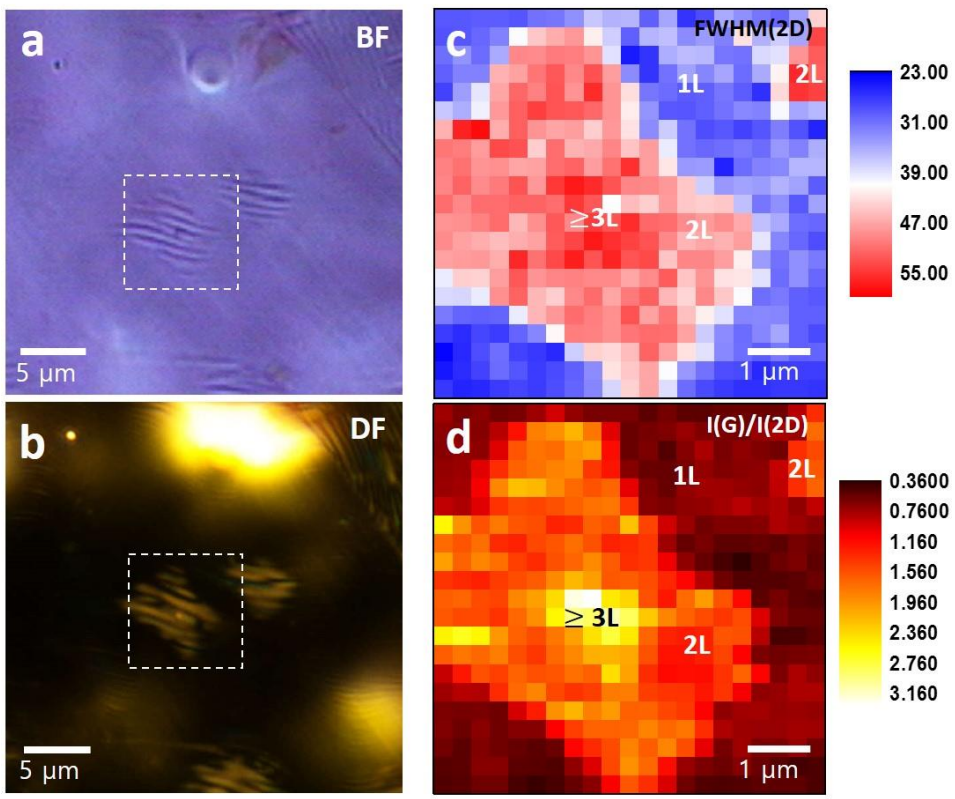

Figure 18 Raman map indicating layer number of the graphene on Cu. a. Bright field and b. dark field optical microscope images of the field. Raman map composed of c. Full width of half maximum (FWHM) of the 2D peak, and the d. intensity ratio I(G)/I(2D). the distance between the pixel is about 0.3 nm. The unit of the scale in c is cm^{-1}.

graphene, bilayer graphene, and the center of the bilayer graphene (Figure 3d). This Raman map also gives clear distinctive feature. To give relation between these two factors (FWHM(2D) and I(G)/I(2D)) and the number of layers of graphene clearly, values from all points were extracted and averaged (Figure 19). The value of the average and the standard deviation is given in Table 1. By combining these two Raman map, we can conclude the monolayer graphene was grown in the entire surface with narrow wrinkle structure, whereas the bilayer graphene is grown on wider wrinkle structure.

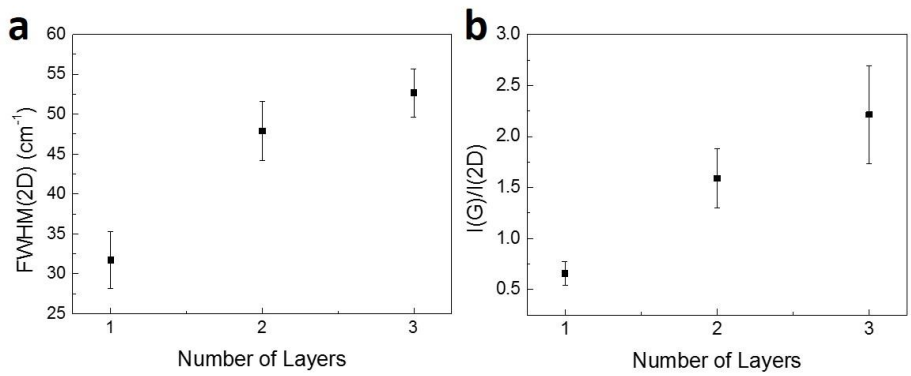

Figure 19 The average of the FWHM(2D) and the I(G)/I(2D). a. Average value of FWHM(2D) and b. I(G)/I(2D) to the layer number of graphene. The data points of the each layer number were collected from the map, and were sorted by referring the feature of the Raman map. The values at the boundary was rejected to calculate the value accurately.

Table 1 The value of the FWHM(2D) and the I(G)/I(2D) in Figure

Number of Layers	Avg. FWHM(2D) (cm^{-1})	Standard dev. FWHM(2D) (cm^{-1})	Avg. I(G)/I(2D)	Standard dev. I(G)/I(2D)
1	31.7	3.55	0.66	0.12
2	47.9	3.68	1.59	0.29
3	52.7	3.03	2.21	0.48

3.2 Strain estimation via peak shift

The phonon frequency of the graphene can be modulated by the external strain. As the tensile strain makes the lattice equilibrium distance longer, phonon will be softened, while the compressive strain makes phonon stiff due to shortened lattice equilibrium distance. The change of the phonon frequency can be detected using Raman spectroscopy. The characteristic peaks of the graphene (the G peak and the 2D peak) is shifted when graphene is under tensile/compressive strain, as the phonon softening/stiffening changes the scattering energy for phonon excitation in Raman scattering process.

The graphene can have residual strain after the synthesis. The large different thermal expansion behavior introduces the strain in graphene lattice. The negative thermal expansion coefficient of the graphene at room temperature and one order larger thermal expansion coefficient of Cu expect the total compression of graphene would be about 1.8 % in thermal quenching process starts from 1200 K to 300 K [58.59]. Several works suggested the ripples and wrinkles are formed to release this large strain [56]. However, the graphene-metal interaction is still not fully understood yet. In example, the biaxial compressive strain was linearly increased within increasing growth temperature from 900℃ to 1100℃ in the demonstration by Yu *et al*., but the compressive strain range is between 0.1% to 0.5% which is smaller than expected compression [60]. This reason of this result would be the stress relaxation by ripple or wrinkle formation and the defect pinning at the high temperature, but not exact reason has been revealed.

To investigate the relation between the number of layers of graphene and the residual strain after the synthesis, we compared the shift of the G peak and the 2D peak. The sensitivity of the phonon frequency to the strain is described by Grüneisen parameter. The Grüneisen parameter γ is defined for uniaxial strain ε as

$$\gamma_{\mathrm{uni}} = -\frac{1}{\omega_0}\frac{\partial\omega}{\partial\varepsilon}$$

where ω_0 is the Raman frequency at zero strain [61]. Under biaxial strain, due to the same amount of the strain in longitudinal and transverse direction, Grüneisen parameter is

$$\gamma_{\mathrm{bi}} = -\frac{1}{2\omega_0}\frac{\partial\omega}{\partial\varepsilon}$$

The Grüneisen parameters have been measured for both uniaxial strain and biaxial strain [61-64]. Reported Grüneisen parameters are different in each study, ranging from 1.8 to 2.4 for G peak, and 2.6 to 3.8 for 2D peak (Table 2). We first hypothesized the strain resides in graphene is biaxial strain, so the values of Raman peak shift to the applied biaxial strain from the reference [62] ($\partial\omega_{\mathrm{G}}/\partial\varepsilon \sim -57.3$ and $\partial\omega_{2\mathrm{D}}/\partial\varepsilon \sim -160.3$) were adapted first.

Table 2 The Grüneisen parameters for the biaxial strain

Reference	$\Delta(2D/G)$	$\gamma(G)$	$\gamma(2D)$
[61] exp.	3.03	1.99	3.55
[61] calculated	2.48	1.8	2.7
[62]	2.8	1.8	2.98
[63]	2.63	2.4	3.8
[64] monolayer	2.45	1.8	2.6
[64] bilayer	1.9-2.5		

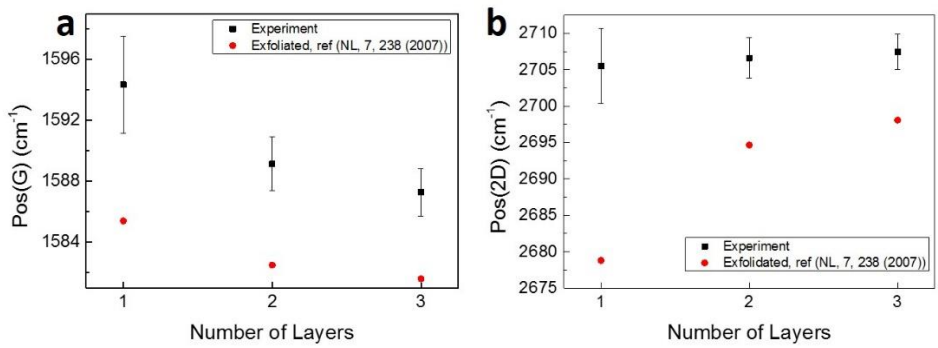

Figure 20 The average of the position shifts of the G peak and the 2D peak. a. G peak position and b. 2D peak position shift of the data collected from the Raman map. The reference position of the G peak and the 2D peak of mechanically exfoliated graphene using 532 nm excitation was plotted together (red circle).

Table 3 The shift of the peaks and the estimated biaxial strain

Number of layers	$\Delta\omega_G$ (cm^{-1})	$\Delta\omega_{2D}$ (cm^{-1})	Predicted strain (%)	Predicted strain (%)
1	8.95	26.7	-0.156	-0.167
2	6.63	11.95	-0.116	-0.075
3	5.67	9.38	-0.099	-0.059

To estimate the strain on graphene, the peak shift of the G peak and 2D peak was plotted (Figure 20). The data was sorted by the number of the layers, which was clarified by the Raman map of the FWHM(2D) and the I(G)/I(2D). In addition, the position of the G peak and the 2D peak of the exfoliated graphene acquired using laser excitation of 532 nm wavelength was collected from the reference [65] to compare data with the unstrained neutral graphene. The average of the position of the G peak and the 2D peak were all significantly upshifted as expected to compressive biaxial strain (Figure 20a,b). Using the value for the Raman G peak shift to the applied strain adapted from [62], the applied biaxial strain on monolayer/bilayer/trilayer graphene were -0.156%, -0.116% and -0.099%. On the other hand, by using the value of 2D peak shift to strain, $\partial\omega_{2D}/\partial\varepsilon \sim -160.3$, the applied biaxial strain on monolayer/bilayer/trilayer graphene were -0.167%, -0.075% and -0.059%. The discrepancy between the each estimation of biaxial strain is not known yet, but the charge doping on the graphene due to the charge transfer between the graphene/ Cu or spatially non-uniform strain might be responsible for the results, which will be discussed in the next section.

3.3 Estimation of charge doping on graphene

The shift of the Fermi energy in the graphene induces the change of Raman scattering. First, the phonon softening/stiffening by the non-adiabatic behavior shifts the G peak and the 2D peak frequency [48]. Second, the forbidden phonon decaying into an electron-hole pair due to Pauli exclusion principle sharpens the phonon linewidths [66]. The linewidth of the 2D peak is insensitive to the doping, while the linewidth of the G peak shows strong dependence on the carrier concentration[67,68]. Therefore, the charge doping on graphene can be estimated by either measuring shifts of the G peak and the 2D peak or measuring FWHM(G). Both methods will be discussed in this section.

First, the average of FWHM(G) was plotted to the number of the layers of graphene (Figure 21). The average FWHM (G) of monolayer was about 16 cm^{-1}. Comparing with the FWHM(G) of the charge neutral graphene ~ 14 cm^{-1}, the higher values of FWHM(G) can be interpreted as that the charge density of synthesized graphene on Cu is very low. The low charge doping on graphene can suggest the weak interaction between Cu and graphene in our system. This weak interaction between graphene is coherent to the first principle study, which has suggest the charge transfer between graphene and Cu causes a Fermi level upshift of graphene by 0.17 eV [69].

The reason of higher FWHM than neutral graphene was suggested that non-uniform strain can reside in graphene by the formation of the superlattice between the graphene and Cu [70]. The lattice mismatch between graphene and Cu(100) or

Cu(111) introduces non-uniform van der Waals interaction, so non-uniform biaxial strain can reside in graphene[71]. The slight broadening of FWHM(G) of our result can be interpreted as the small degree of non-uniformity in biaxial compressive strain. In addition, the FWHM(2D) of monolayer was about ~ 31 cm^{-1}, which is similar to the unstrained neutral graphene (~29 cm^{-1}). When the graphene is under uniaxial strain, the lattice symmetry breaking induces the change of the geometry of the Brillouin zone, so resonance (G peak) and double resonance process (2D peak) are split into two depends on the polarization direction of laser [57]. Therefore, negligible broadening of the G peak and the 2D peak in the monolayer region indicates the strain on graphene is almost biaxial strain.

For the bilayer graphene, the effect of charge doping on the G peak of graphene has been investigated [72-74]. Owing to the stacked geometry, non-equivalent charge doping on top layer and the bottom layer can induce the symmetry breaking, which can activate the additional G band mode [9]. There was no detectable G peak splitting in our result, so the possibility of inhomogeneous charge density between the top layer and the bottom layer was excluded. The FWHM(G) of the bilayer graphene decreases with increasing carrier concentration [73,74]. This result is due to the Pauli exclusion principle similar to the case of single layer graphene. Comparing with our result, average FWHM(G) of bilayer graphene was about 16 cm^{-1} (Figure 21). As similar to the monolayer graphene, the result can be interpreted as the charge doping on bilayer graphene is low. The FWHM(G) of the trilayer graphene was also about 16 cm^{-1} in average. The effect of carrier concentration on the G mode of trilayer graphene was also investigated,

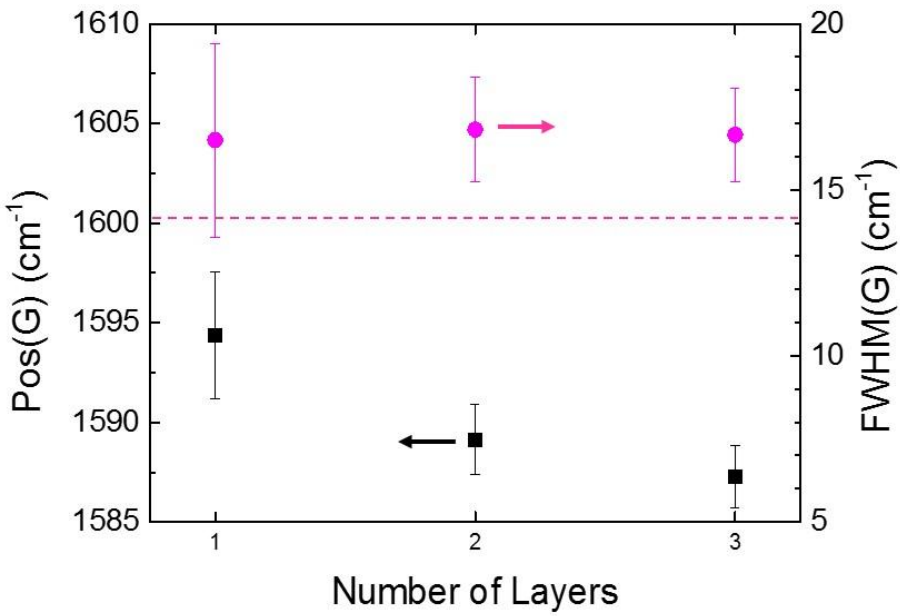

Figure 21 The position and the FWHM of the G peak. The position of the G peak was assigned as black square, and the FWHM of the G peak was assigned as magenta circle.

but the tendency of the G band linewidth is not reported [75]. Although the relation between carrier concentration and linewidth of the G mode in trilayer graphene is hard to find, the similar behavior to monolayer or bilayer graphene would be expected. Therefore, the charge density on the graphene can be determined as low in all points.

By estimating the linewidth of the G peak, the charge density on graphene was determined as very low. The Fermi level shift of the graphene also induces change of intensity of the G peak and the 2D peak. For graphene doped by electric field effect, the intensity ratio I(2D)/I(G) decreases within increasing carrier concentration [50]. This Raman peak intensity dependence of graphene on doping occurs due to electron-electron scattering [51]. For graphene with low Fermi energy ($E_F \ll 1$), the intensity of the 2D peak can be written as [51]

$$I(2D) = C(\gamma_K/\gamma)^2$$

$$\sqrt{1/I(2D)} = \frac{1}{\gamma_K\sqrt{C}}(\gamma_{ep} + f(\varepsilon)|E_F|)$$

where C is a constant, $\gamma = \gamma_{ep} + \gamma_{ee}$ and $\gamma_{ep} = \gamma_K + \gamma_\Gamma$ are the emission rate of the total scattering and the electron-phonon scattering. The $f(\varepsilon)$ is a function depends on the dielectric environment. Since I(G) is insensitive to the doping, I(G)/I(2D) can be used to derive γ_{ep}

$$\sqrt{I(G)/I(2D)} = C'(\gamma_{ep} + f(\varepsilon)|E_F|)$$

In our experiment, the dielectric environment is air ($\varepsilon = 1$), so using the equation and the relation for dimensionless Coulomb coupling constant $r = e^2/(\varepsilon v_F)$ from reference [51], $f \sim 0.11$. This relation is proved by the experiments in the low Fermi energy bound [51,52].

To determine the Fermi level of the monolayer graphene in sample, experimental relation between I(2D)/I(G) and carrier concentration from reference [75] was used. The I(2D)/(G) ratio was directly converted to the carrier concentration using the empirical data, and the carrier concentration was converted to Fermi energy by the relation [76,77]

$$E_F(n) = \hbar|v_F|\sqrt{\pi n}$$

where $|v_F| = 1.1 \times 10^6\ ms^{-1}$ is the Fermi velocity. The average Fermi energy of the monolayer was 0.34 eV $\pm$ 0.9 eV varied from ~0.14 eV to ~0.5 eV, which is corresponding to the carrier concentration of ~ 1.0 $\times$ 10^{12} cm^{-2} to ~ 1.5 $\times$ 10^{13} cm^{-2}. The result is consistent with the weak interaction between graphene and Cu. By converting the I(2D)/I(G) to Fermi energy, the map for monolayer graphene can be plotted to estimate the spatial variation of the charge doping on graphene monolayer (Figure 22). As clearly seen, the Fermi energy of monolayer graphene is varied in space, and the strongly doped domain is up to 1.5 μm.

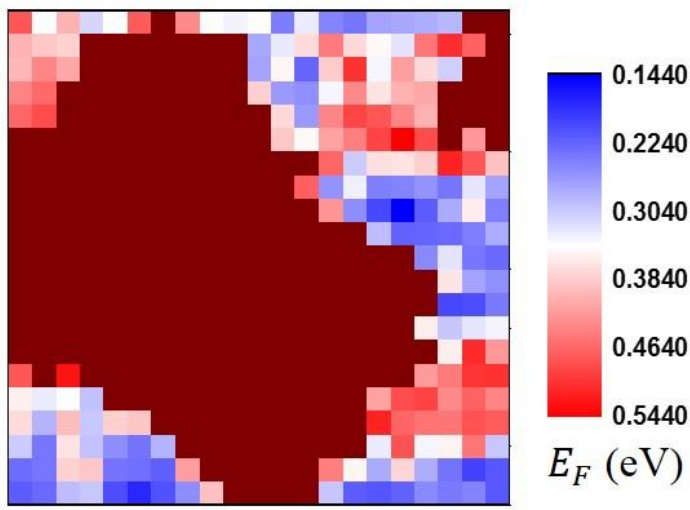

Figure 22 Fermi energy of the monolayer graphene. Data was converted from the I(G)/I(2D).

3.4 Separation of the strain from charge doping effect

The spatial map of the Fermi energy of monolayer graphene reveals the inhomogeneous charge density on graphene. However, since the peak intensity ratio I(2D)/I(G) decreases within increasing concentration of either electron or hole [50-52], so the exact doping type is hard to be derived from the Raman map. However, strain effects can be separated from charge doping effects. Both strain and charge doping on graphene can shift the G and 2D peak [50,62], but those effects can be separated by comparing the $\Delta\omega_G$ and $\Delta\omega_{2D}$ owing to the different peak shift behavior. Lee *et al*. separated the Raman peak shift to two components and successfully estimated the strain and charge doping on graphene [78]. Plotting $\Delta\omega_G$ - $\Delta\omega_{2D}$ graph with spatially resolved Raman data, we can see the distinguishing tendency of the peak position shift. We note that our data is well fitted with charge neutral line which has slope of 2.8. The value of $\Delta\omega_{2D}/\Delta\omega_G$ for strained graphene was reported previously, ranging 2.02 ~ 2.44 for uniaxially strained graphene [61,79,80] and 2.25 ~ 3.03 for biaxially strained graphene [61-64]. Because there are no noticeable Raman peak splitting in either G or 2D band, biaxial strain is dominant in our sample. This relation indicates the graphene lattice compression would be introduced after the Cu step formation. Since the wrinkle structure is aligned to the one direction, no noticeable uniaxial strain indicates that the periodic structure is not formed by stress release to specific direction. The graphene would be mainly compressed on the flat terrace of Cu.

Data collected from monolayer graphene is scattered above that of

bilayer/trilayer graphene, which indicates that monolayer graphene is more compressed than the bilayer and trilayer graphene. The data points are not exactly on the charge neutral line, but scattered to tight side of the line. This is due to the charge doping effects, which induce almost horizontal shift of the points in both n-type and p-type doping cases. The inhomogeneous doping effects on graphene would be induced by spatially different charge transfer between Cu and graphene which induces n-type doping [69,81], or adsorbents from ambient air which possibly induce p-type doping [82]. It is hard to distinguish exact type of doping, but we can separate the strain effect from the charge doping effect because 2D peak shifts more sensitively to the strain than doping effect.

Figure 23 shows compressive strain map converted from the Raman data. As inferred from the $\Delta\omega_G - \Delta\omega_{2D}$ plot, biaxial compressive strain on monolayer graphene was higher than those of bilayer/trilayer graphene, which is matched with the AFM image of Cu step edge. Biaxial strain varies -0.1 % ~ -0.2 % on monolayer graphene, -0.05 % ~ -0.1 % on bi/trilayer graphene. From the comparison between the compressive strain map in Fig. 4b and surface morphology in Fig. 1c, we notice that periodicity of the Cu step edges is related to the strain on graphene. Cu step edges were narrower under strongly compressed monolayer graphene, whereas Cu step edges were broadened under less compressed bilayer/trilayer graphene. The results suggest that periodicity of the Cu step edges are changed by the different degree of stress relaxation of graphene/Cu interface.

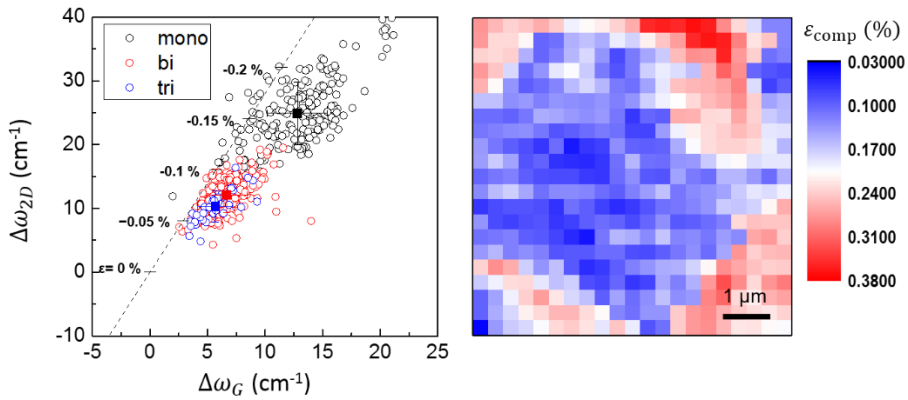

Figure 23 $\Delta\omega_G$-$\Delta\omega_{2D}$ correlation and compressive strain map. (a) $\Delta\omega_G$-$\Delta\omega_{2D}$ correlation of the monolayer/bilayer/trilayer graphene. Dashed line is charge neutral line which is assumed from the values of $\partial\omega_G/\partial\varepsilon$ ~ -57.3 and $\partial\omega_{2D}/\partial\varepsilon$ ~ -160.3 from the reference 62. (b) Compressive strain map converted from the spatially resolved Raman data.

The origin of the wrinkle-like periodic Cu step formation has been remained in question. In our observation, Cu steps were formed in one direction with periodicity, but biaxial strain on graphene cannot explain the dramatic transition of Cu step periodicity. Rather, by obtaining high-resolution topographic AFM image, Cu step termination at the boundary and distinguishing facet evolution under the bilayer graphene implies other effect. The reconstructed surface shows similar behavior observed by Wang *et al.*, which identical facets were exposed under the different graphene sheets in same Cu grain [43]. The surface reconstruction is a result of interface energy minimization of Cu/graphene during cooling started from the liquid-like premelted Cu surface layer at high temperature [42,43]. Although interaction between Cu and graphene shows very weak physisorption at room temperature [69], but interaction between Cu and graphene is important at high temperature [83]. Similarly, our observation would be interpreted as the result of the energy minimization at graphene/Cu interface during cooling, but graphene with different layer numbers gives which has different degree of interaction with Cu surface induces distinctive surface structure.

3.5 Conclusion

In summary, we study the effect of graphene layer numbers on Cu surface reconstruction. The AFM and Raman spectroscopy show that periodic ripple-like Cu step edge is formed under graphene, and its periodicity is noticeably increased under bilayer/trilayer graphene (trilayer > bilayer > monolayer). In addition,

Raman G and 2D peaks of graphene are generally less blue-shifted with increasing graphene layers, which indicates that graphene is more compressed with decreasing layer numbers. The results show that the Cu surface reconstruction under graphene is clearly affected by the different interaction between Cu and graphene layers.

References

[1] Neto, A. H. C.; Guinea, F.; Peres, N. M. R.; Novoselov, K. S.; Geim, A. K. *Rev. Mod. Phys.* **2009**, *81*, 109.

[2] Marder, M. P. *Condensed Matter Physics*, 2nd ed., Wiley, **2010**.

[3] S. Reich, J. Maultzsch, C. Thomsen and P. Ordejón, *Phys. Rev. B* **2002**, *66*, 035412.

[4] P. R. Wallace, *Phys. Rev.* **1947**, *71*, 622.

[5] Geim, A. K.; Novoselov, K. S. *Nat. Mater.* **2007**, *6*, 183.

[6] Berger, C.; Song, Z.; Li, T.; Li, X.; Ogbazghi, A. Y.; Feng, O.; Dai, Z.; Marchenkov, A. N.; Conrad, E. H., First, P. N.; de Heer, W. A. *J. Phys. Chem. B* **2004**, *108*, 19912.

[7] Rutter, G. M.; Crain, J. N.; Guisinger, N. P.; Li, T.; First, P. N.; Stroscio, J. A. *Science* **2007**, *317*, 219.

[8] Vaari, J.; Lahrinen, J.; Hautojärvi, P. *Catal. Lett.* **1997**, *44*, 43.

[9] Gamo, Y.; Nagashima, A.; Wakabayashi, M.; Terai, M.; Oshima, C. *Surf. Sci.***1997**, *374*, 61.

[10] Kawano, T.; Kawaguchi, M.; Okamoto, Y.; Enomoto, H.; Bando, H.; *Solid State Sci.* **2002**, *4*, 1521.

[11] Starodubov, A. G.; Medvetskii, M. A.; Shikin, A. M.; Adamchuk, V. K. *Phys.*

Solid State **2004**, *46*, 1340.

[12] Land, T. A.; Michely, T.; Behm, R. J.; Hemminger, J. C.; Comsa, G. *Surf. Sci.***1992**, 264, 261.

[13] Ueta, J.; Saida, M.; Nakai, C.; Yamada, Y.; Sasaki, M.; Yamamoto, S. *Surf. Sci.* **2004**, *560*, 183.

[14] Starr, D. E.; Pazhetnov, E. M.; Stadnichenko, A. I.; Boronin, A. I.; Shaikhutdinov, S. K. *Surf. Sci.* **2006**, *600*, 2688.

[15] Oshima, J.; Nagashima, A. *J. Phys.: Condens. Matter* **1997**, *9*, 1.

[16] Marchini, S.; Günther, S.; Wintterlin, J. *Phys. Rev. B* **2007**, *76*, 075429.

[17] de Parga, A. L. V.; Calleja, F.; Borca, B.; Passeggi, J. M. C. G.; Hinarejos, J. J.; Guinea, F.; Miranda, R. *Phys. Rev. Lett.* **2008**, *100*, 056807.

[18] Sutter, P. W.; Flege, J.-I.; Sutter, E. A. *Nat. Mater.* **2008**, *7*, 406.

[19] Gall, N. R.; Rutkov, E. V.; Tontegode, A. Y. *Phys. Solid State* **2004**, *46*, 371.

[20] N'Diaye, A. T.; Bleikamp, S.; Feibelman, P.; Michely, T. *Phys. Rev. Lett.* **2006**, *97*, 2315501.

[21] Makarenko, I. V.; Titkov, A. N.; Waqar, Z.; Dumas, P.; Rutkov, E. V.; Gall, N. R. *Phys. Solid State* **2007**, *49*, 371.

[22] Li, X.; Cai, W.; An, J.; Kim, S.; Nah, J.; Yang, D.; Piner, R.; Velamakanni, A.; Jung, I.; Tutuc, E.; Banerjee, S. K.; Colombo, L.; Ruoff, R. S. **2009**, *324*, 1312.

[23] Srivastava, A.; Galande, C.; Ci, L.; Song, L.; Rai, C.; Jariwala, D.; Kelly, K. F.; Ajayan, P. M. *Chem. Mater*. **2010**, *22*, 3457.

[24] Voloshina, E.; Dedkov, Y. *Phys. Chem. Chem. Phys.* **2012**, *14*, 13502.

[25] McCann, E. *Phys. Rev. B* **2006**, *74*, 161403.

[26] Novoselov, K. S.; Geim, A. K.; Morozov, S. V.; Jiang, D.; Katsnelson, M. I.; Grigorieva, I. V.; Dubonos, S. V.; Firsov, A. A. *Nature* **2005**, *438*, 197.

[27] Bolotin, K. I.; Sikes, K. J.; Jiang, Z.; Fudenberg, G.; Hone, J.; Kim, P.; Stormer, H. L. *Solid State Commun*. **2008**, *146*, 351.

[28] Sabio, J.; Seoanez, C.; Fratini, S.; Guinea, F.; Neto, A. H. C.; Sols, F. *Phys. Rev. B* **2008**, *77*, 235430.

[29] Leenaerts, O.; Partoens, B.; Peeters, F. M. *Phys. Rev. B* **2008**, *77*, 125416.

[30] Lee, E. J. H.; Balasubramanian, K.; Weitz, R. T.; Burghard, M.; Kern, K. *Nat. Nanotechnol.* **2008**, *3*, 486.

[31] Reina, A.; Jia, X.; Ho, J.; Nezich, D.; Son, H.; Bulovic, V.; Dresselhaus, M.; Kong, J. *Nano Lett.* **2009**, *9*, 30.

[32] Li, X.; Cai, W.; An, J.; Kim, S.; Nah, J.; Yang, D.; Piner, R.; Velamakanni, A.; Jung, I.; Tutuc, E.; Banerjee, S. K.; Colombo, L.; Ruoff, R. S. **2009**, *324*, 1312.

[33] Liu, N.; Fu, L.; Dai, B.; Yan, K.; Liu, X.; Zhao, R.; Zhang, Y.; Liu, Z. *Nano Lett.* **2011**, *11*, 297.

[34] Guinea, F.; Katsnelson, M. I.; Vozmediano, M. A. H. *Phys. Rev. B* **2008**, *77*,

075422.

[35] Obraztsov, A.; Obraztsova, E.; Tyurnina, A.; Zolutukhin, A. *Carbon* **2007**, *45*, 2017.

[36] Tian, J.; Cao, H.; Wu, W.; Yu, Q.; Guisinger, N. P.; Chen, Y. P. *Nano Lett.* **2012**, *12*, 3893.

[37] Hayashi, K.; Sato, S.; Yokoyama, N. *Nanotechnology* **2013**, *24*, 025603.

[38] Ni, G.-X.; Zheng, Y.; Bae, S.; Kim, H. R.; PAchoud, A.; Kim, Y. S.; Tan, C.-L.; Im, D.; Ahn, J.-H.; Hong, B. H.; Ö zyilmaz, B. *ACS Nano* **2012**, *6*, 1158.

[39] Liu, N.; Pan, Z.; Fu, L.; Zhang, C.; Dai, B.; Liu, Z. *Nano Res.* **2011**, *4*, 996.

[40] Pan, Z.; Liu, N.; Fu, L.; Liu, Z. *J. Am. Chem. Soc.* **2011**, *133*, 17578.

[41] Paronyan, T. M.; Pigos, E. M.; Chen, G.; Harutyunyan, A. R. *ACS Nano* **2011**, *5*, 9619.

[42] Kim, D. W.; Lee, J.; Kim, S. J.; Jeon, S.; Jung, H.-T. *J. Mater Chem. C* **2013**, *1*, 7819.

[43] Wang, Z.-J.; Weinberg, G.; Zhang, Q.; Lunkenbein, T.; Klein-Hoffmann, A.; Kurnatowska, M.; Plodinec, M.; Li, Q.; Chi, L.; Schloegl, R.; Willinger, M.-G. *ACS Nano* **2015**, *9*, 1506.

[44] Malard, L. M.; Pimenta, M. A.; Dresselhaus, G.; Dresselhaus, M. S. *Phys. Rep.* **2009**, *473*, 51.

[45] Beams, R.; Cançado, L. G.; Novotny, L. *J. Phys.: Condens. Matter* **2015**, *27*,

083002.

[46] Park, J. S.; Cecco, A. R.; Saito, R.; Jiang, J.; Dresselhaus, G.; Dresselhaus, M. S. *Carbon* **2009**, *47*, 1303.

[47] Ferrari, A. C.; Meyer, J. C.; Scardaci, V.; Casiraghi, C.; Lazzeri, M.; Mauri, F.; Piscanec, S.; Jiang, D.; Novoselov, K. S.; Roth, S.; Geim, A. K. *Phys. Rev. Lett.* **2006**, *97*, 187401.

[48] Pisana, S.; Lazzeri, M; Casiraghi, C.; Novoselov, K. S.; Geim, A. K.; Ferrari, A. C.; Mauri, F. *Nat. Mater.* **2007**, *6*, 198.

[49] Lazzeri, M.; Mauri, F. *Phys. Rev. Lett.* **2006**, *97*, 266407.

[50] Das, A.; Pisana, S.; Charkraborty, B.; Piscanec, S.; Saha, S. K.; Waghmare, U. V.; Novoselov, K. S.; Krishnamurthy, H. R.; Geim, A. K.; Ferrari, A. C.; Sood, A. K. *Nat. Nanotechnol.* **2008**, *3*, 210.

[51] Basko, D. M.; Piscanec, S.; Ferrari, A. C. *Phys. Rev. B* **2009**, *80*, 165413.

[52] Casiraghi, C. *Phys. Rev. B* **2009**, *80*, 233407.

[53] Li, X.; Magnusoin, C. W.; Venugopal, A.; Tromp, R. M.; Hannon, J. B.; Vogel, E. M.; Colombo, L.; Ruoff, R. S. *J. Am. Chem. Soc.* **2011**, *133*, 2816.

[54] Havener, R. W.; Zhuang, H.; Brown, L.; Hennig, R.; Park, J. *Nano Lett.* **2012**, *12*, 3162.

[55] Wofford, J. M.; Nie, S.; McCarty, K. F.; Bartelt, N. C.; Dubon, O. D. *Nano Lett.* **2010**, *10*, 4890-4896.

[56] Zhang, Y.; Gao, T.; Gao, Y.; Xie, S.; Ji, Q.; Yan, K.; Peng, H.; Liu, Z. *ACS Nano* **2011**, *5*, 4014-4022.

[57] Frank, O.; Mohr, M.; Maultzsch, J.; Thomsen, C.; Riaz, I.; Jalil, R.; Novoselov, K. S.; Tsoukleri, G.; Parthenios, J.; Papagelis, K.; Kavan, L.; Galiotis, C. *ACS Nano* **2011**, *5*, 2231.

[58] Jian, J.-W.; Wang, J.-S.; Li, B. *Phys. Rev. B* **2009**, *80*, 205429.

[59] Nix, F. C.; MacNair, D. *Phys. Rev.* **1941**, *60*, 597.

[60] Yu, V.; Whiteway, E.; Maassen, J.; Hilke, M. *Phys. Rev. B* **2011**, *84*, 205407.

[61] Mohiuddin, T. M. G.; Lombardo, A.; Nair, R. R.; Bonetti, A.; Savini, G.; Jalil, R.; Bonini, N.; Basko, D. M.; Galiotis, C.; Marzari, N.; Novoselov, K. S.; Geim, A. K.; Ferrari, A. C. *Phys. Rev. B* **2009**, *79*, 205433.

[62] Ding, F.; Ji, H.; Chen, Y.; Herklotz, A.; Dörr, K.; Mei, Y.; Rastelli, A.; Schmidt, I. G. *Nano Lett.*, **2010**, *10*, 3453.

[63] Metzger, C.; Rémi, S.; Liu, M.; Kusminskiy, S. V.; Neto, A. H. C.; Swan, A. K.; Goldberg, B. B. *Nano Lett.* **2010**, *10*, 6.

[64] Zabel, J.; R. R. Nair,; Ott, A.; Gerogiu, T.; Geim, A. K.; Novoselov, K. S.; Casiraghi, C. *Nano Lett.* **2012**, *12*, 617.

[65] Graf, D.; Molitor, F.; Ensslin, K.; Stampfer, C.; Jungen, A.; Hierold, C.; Wirtz, L. *Nano Lett.* **2007**, *7*, 238.

[66] Lazzeri, M.; Piscanec, S.; Mauri, F.; Ferrari, A. C.; Robertson, J. *Phys. Rev. B*

2006, *73*, 155426.

[67] Yan, J.; Zhang, Y.; Kim, P.; Pinczuk, A. *Phys. Rev. Lett.* **2007**, *98*, 166802.

[68] Stampfer, C.; Molitor, F.; Graf, D.; Ensslin, K.; Jungen, A.; Hierold, C.; Wirtz, L. *Appl. Phys. Lett.* **2007**, *97*, 241907.

[69] Khomyakov, P. A.; Giovannetti, G.; Rusu, P. C.; Brocks, G.; van den Brink, J.; Kelly, P. J. *Phys. Rev. B* **2009**, *79*, 195425.

[70] He, R.; Zhao, L.; Petrone, N.; Kim, K. S.; Roth, M.; Hone, J.; Kim, P.; Pasupathy, A.; Pinczuk, A. *Nano Lett.* **2012**, *12*, 2408.

[71] Aitken, Z. H.; Huang, R. *J. Appl. Phys.* **2010**, *107*, 123531

[72] Malard, L. M.; Elias, D. C.; Alves, E. S.; Pimenta, M. A. *Phys. Rev. Lett.* **2008**, *101*, 257401.

[73] Yan, J.; Henriksen, E. A.; Kim, P.; Pinczuk, A. *Phys. Rev. Lett.* **2008**, *101*, 136804.

[74] Das, A.; Chakraborty, B.; Piscanec, S.; Pisana, S.; Sood, A. K.; Ferrari, A. C. *Phys. Rev. B* **2009**, *79*, 155417.

[75] Lui, C. H.; Cappelluti, E.; Li, Z.; Heinz, T. F. *Phys. Rev. Lett.* **2013**, *110*, 185504.

[76] Novoselov, K. S.; Geim, A. K.; Morozov, S. V.; Jiang, D.; Katsnelson, M. I.; Grigorieva, I. V.; Dubonos, S. V.; Firsov, A. A. *Nature* **2005**, *438*, 197.

[77] Zhang, Y.; Tan, Y.-W.; Stormer, H. L.; Kim, P. *Nature* **2005**, *438*, 201.

[78] Lee, J. E.; Ahn, G.; Shim, J.; Lee, Y. S.; Ryu, S. *Nat. Commun.* **2012**, *3*, 1024.

[79] Huang, M.; Yan, H.; Chen, C.; Song, D.; Heinz, T. F.; Hone, J. *Proc. Natl. Acad. Sci. USA* **2009**, *106*, 7304.

[80] Yoon, D.; Son, Y. W.; Cheong, H. *Phys. Rev. Lett.* **2011**, *106*, 155502.

[81] Zheng, J.; Wang, Y.; Wang, L.; Quhe, R.; Ni, Z.; Mei, W.-N.; Gao, Z.; Yu, D.; Shi, J.; Lu, J. *Sci. Rep.* **2013**, *3*, 2081.

[82] Li, Z.; Wang, Y.; Kozbial, A.; Shenoy, G.; Zhou, F.; McGinley, R.; Ireland, P.; Morganstein, B.; Kunkel, A.; Surwade, S. P.; Li, L.; Liu, J. *Nat. Mater.* **2013**, *12*, 925.

[83] Wood, J. D.; Schmucker, S. W.; Lyons, A. S.; Pop, E.; Lyding, J. W. *Nano Lett.* **2011**, *11*, 4547.

국문 초록

화학 기상 증착법 (chemical vapor deposition)을 이용하여 그래핀을 구리 표면에 합성하게 되면 구리의 표면 형상이 변화하게 된다. 이러한 현상은 구리와 그래핀의 열팽창 계수가 다르기 때문이라고 알려져 있지만 그래핀이 구리 표면의 재구성에 대하여 어떠한 관계를 가지고 있는지에 대해서는 아직 밝혀지지 않고 있다. 본 논문에서는 화학 기상 증착법으로 가스 유량과 합성시간 등을 조절하여 다른 층수의 그래핀을 구리 표면에 합성하였다. 원자 힘 현미경 (atomic force microscopy) 이미지와 그래핀의 라만 분광 신호를 분석한 결과 구리 표면의 계단형 모서리들이 그래핀의 층수가 증가할수록 확연하게 증가하는 것을 확인할 수 있었다. 더 나아가 라만 G, 2D 피크의 변화를 통해 단층 그래핀의 압축 변형도가 이중층, 삼중층 그래핀 보다 높다는 것을 밝혀내었다. 이러한 결과들은 그래핀의 층수가 구리 표면 형상의 재구성에 대해 큰 영향을 가진다는 것을 제안한다.

주요어: 그래핀, 표면 재구성, 원자힘 현미경, 라만 분광법

학 번: 2013-20251

이학석사학위논문

Raman Spectroscopy Study on the Graphene Induced Surface Reconstruction

그래핀에 의해 유도된 표면 재구성에 대한 라만 분광 연구

2015 년 8 월

서울대학교 대학원

화학부 물리화학 전공

강 진 현

M. S. Thesis

Raman Spectroscopy Study on the Graphene Induced Surface Reconstruction

Advisor: Prof. Byung Hee Hong

Major: Physical Chemistry

Jin Hyoun Kang

Department of Chemistry

Graduate School of Seoul National University

August 2015

Abstract

Jin Hyoun Kang
Department of Chemistry
The Graduate School of Seoul National University

The surface morphology of copper (Cu) often changes during graphene synthesis by chemical vapor deposition (CVD); the change is attributed to the thermal expansion coefficient mismatch between graphene and Cu. However, the obvious relationship between the reconstructed Cu surface and graphene is not totally understood yet. Here we synthesized graphene with different layer numbers using a CVD system by controlling the gas flow and time. Atomic force microscopy (AFM) images and the Raman G and 2D peaks show that Cu step edges became noticeably broader with increasing graphene layer number. Furthermore, $\Delta\omega\_G–\Delta\omega\_2D$ plot indicates that the biaxial compressive strain on monolayer graphene was higher than that on bi/trilayer graphene, which agrees overall with topographic AFM images. Our results suggest that stress relaxation from the less strained bi/trilayer graphene crucially affects Cu surface reconstruction.

Keywords: Graphene, Surface reconstruction, Atomic force microscopy, Raman spectroscopy

Student number: 2013-20251

Contents

Chapter 1. Introduction

Chapter 2. Synthesis of Graphene on Cu Foil and Morphology Evolution

Chapter 3. Raman Spectroscopy Study

List of Figures

Chapter 1

Chapter 2

List of Tables and Scheme

Chapter 3

Chapter 1

Introduction

1.1 Brief Introduction of Graphene

Graphene is composed of carbon atoms in 2-dimensional honeycomb structure. Graphene is distinct with graphite, because the partial overlaps between interlayer π-orbitals are absence in graphene. In the view as a chemist, graphene resembles the polyaromatic hydrocarbons with infinite number of interconnected rings. By applying the secular determinants with Hückel approximation resembled with tight-binding approximation in physics, the energy level of π-electronic system could be obtained. To consider lattice symmetry, we need to introduce the tight-binding approach.

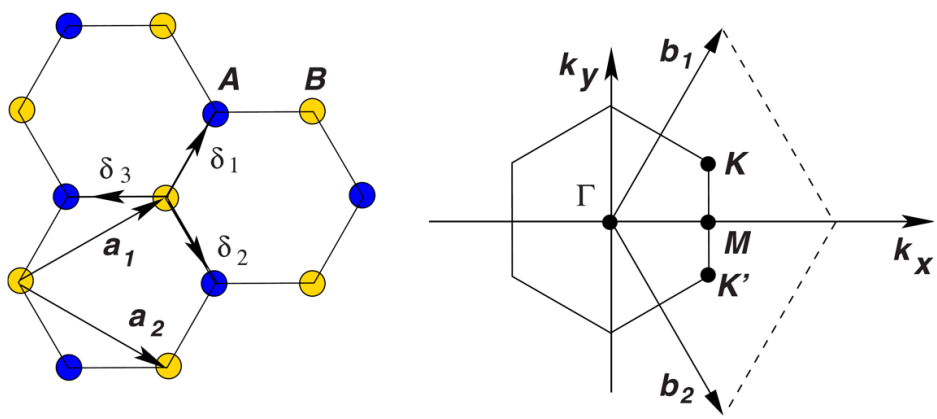

Figure 1 Honeycomb lattice and its reciprocal lattice (first Brillouin zone). The image was adapted from Neto [1].

The honeycomb lattice structure of graphene is triangular lattice with two-atom basis (left, Figure 1)[1]. The lattice vectors and reciprocal vectors are written

as

$$\boldsymbol{a}_1 = \frac{a}{2}(3, \sqrt{3}), \qquad \boldsymbol{a}_2 = \frac{a}{2}(3, -\sqrt{3})$$

$$\boldsymbol{b}_1 = \frac{2\pi}{3a}(1, \sqrt{3}), \qquad \boldsymbol{b}_2 = \frac{2\pi}{3a}(1, -\sqrt{3})$$

where $a =$ 1.42 Å. The corner of the first Brillouin zone of graphene labeled as *K* and *K′*, are specified

$$\boldsymbol{K} = \left(\frac{2\pi}{3a}, \frac{2\pi}{3\sqrt{3}a}\right), \qquad \boldsymbol{K}' = \left(\frac{2\pi}{3a}, -\frac{2\pi}{3\sqrt{3}a}\right)$$

The Hamiltonian for tight-binding model considers the electron hoping to the nearest neighbor atoms (similar to Hückel approximation). If the electron is hopping from *A* site, the nearest atom is located at *B* site. Thus tight-binding Hamiltonian can be expressed simply as[2]

$$H = -t \sum_{\langle i,j \rangle, \sigma} (a^{\dagger}_{\sigma,i} b^{\dagger}_{\sigma,j} + \text{H. c.})$$

where $a_{\sigma,i}$ is annihilation operator for electron with spin configuration σ, and *t* is the nearest neighbor hopping energy. The eigenfunction of the Hamiltonian is Bloch function, and the energy can be obtained by applying the Hamiltonian on eigenfunction. However, rather than, solving the secular equation would give similar result intuitively. The secular equation expressed with tight-binding Hamiltonian *H*, eigenvalue *E*, and overlap matrix *S* is,

$$\begin{vmatrix} H_{AA}(\boldsymbol{k}) - E(\boldsymbol{k}) S_{AA}(\boldsymbol{k}) & H_{AB}(\boldsymbol{k}) - E(\boldsymbol{k}) S_{AB}(\boldsymbol{k}) \\ H^*_{AB}(\boldsymbol{k}) - E(\boldsymbol{k}) S^*_{AB}(\boldsymbol{k}) & H_{AA}(\boldsymbol{k}) - E(\boldsymbol{k}) S_{AA}(\boldsymbol{k}) \end{vmatrix} = 0$$

If the Hamiltonian only considers the nearest neighbor interaction, the electron hopping is only allowed for $A \rightarrow B$ or the reverse. Then the diagonal component of Hamiltonian is [3],

$$H_{AA} = \frac{1}{N}\sum_{\boldsymbol{R}_A}\sum_{\boldsymbol{R}_{A'}} e^{ik(\boldsymbol{R}_{A'}-\boldsymbol{R}_A)}\langle\varphi_A(r-\boldsymbol{R}_A)|H|\varphi_A(r-\boldsymbol{R}_{A'})\rangle$$

$$= \frac{1}{N}\sum_{\boldsymbol{R}_A}\langle\varphi_A(r-\boldsymbol{R}_A)|H|\varphi_A(r-\boldsymbol{R}_A)\rangle = \varepsilon_{2p}$$

giving orbital energy of remaining $2p_z$ orbital. Similarly, from the lattice site *A*, the nearest neighbors *B* lattice sites are separated with vectors (Fig. 1),

$$\boldsymbol{\delta}_1 = a\left(\frac{1}{2},\frac{\sqrt{3}}{2}\right) \quad \boldsymbol{\delta}_2 = a\left(\frac{1}{2},\frac{\sqrt{3}}{2}\right) \quad \boldsymbol{\delta}_3 = a\left(\frac{1}{2},\frac{\sqrt{3}}{2}\right)$$

The interaction between the nearest atoms is [3],

$$H_{AB} = \frac{1}{N}\sum_{\boldsymbol{R}_A}\sum_{\boldsymbol{R}_B} e^{ik(\boldsymbol{R}_B-\boldsymbol{R}_A)}\langle\varphi_A(r-\boldsymbol{R}_A)|H|\varphi_B(r-\boldsymbol{R}_B)\rangle$$

$$= \sum_j e^{ik\boldsymbol{\delta}_j}\langle\varphi_A(r-\boldsymbol{R}_A)\big|H\big|\varphi_B\big(r-\boldsymbol{R}_A-\boldsymbol{\delta}_j\big)\rangle = \gamma_0(e^{ik\boldsymbol{\delta}_1}+e^{ik\boldsymbol{\delta}_2}+e^{ik\boldsymbol{\delta}_3})$$

$$S_{AB} = \frac{1}{N}\sum_{\boldsymbol{R}_A}\sum_{\boldsymbol{R}_B} e^{ik(\boldsymbol{R}_B-\boldsymbol{R}_A)}\langle\varphi_A(r-\boldsymbol{R}_A)|\varphi_B(r-\boldsymbol{R}_B)\rangle$$

$$= \sum_j e^{ik\boldsymbol{\delta}_j}\langle\varphi_A(r-\boldsymbol{R}_A)\big|\varphi_B\big(r-\boldsymbol{R}_A-\boldsymbol{\delta}_j\big)\rangle = s_0(e^{ik\boldsymbol{\delta}_1}+e^{ik\boldsymbol{\delta}_2}+e^{ik\boldsymbol{\delta}_3})$$

Then we can obtain energy by solving secular equation with defined components

$$E_{\pm}(\boldsymbol{k}) = \frac{\varepsilon_{2p} \mp \gamma_0\sqrt{f(\boldsymbol{k})}}{1 \mp s_0\sqrt{f(\boldsymbol{k})}}$$

where

$$f(\boldsymbol{k}) = 3 + 2\cos \boldsymbol{k} \cdot \boldsymbol{a}_1 + 2\cos \boldsymbol{k} \cdot \boldsymbol{a}_2 + 2\cos \boldsymbol{k} \cdot (\boldsymbol{a}_1 - \boldsymbol{a}_2)$$

If we express the vector $\boldsymbol{k}$ as $\boldsymbol{k} = \boldsymbol{K} + \boldsymbol{q}$, for small $\boldsymbol{q}$,

$$E_{+}(\boldsymbol{k}) \approx E_{-}(\boldsymbol{k})$$

Therefore, intrinsic graphene with tight-binding assumption has zero band gap energy. More explicitly, energy band structure around $\boldsymbol{K}$ point is [4],

$$E_{\pm}(\boldsymbol{q}) \approx \pm v_F|\boldsymbol{q}|$$

where v_F is Fermi velocity. The entire energy band can be derived by the similar method, and can be visualized as Figure 2 [1].

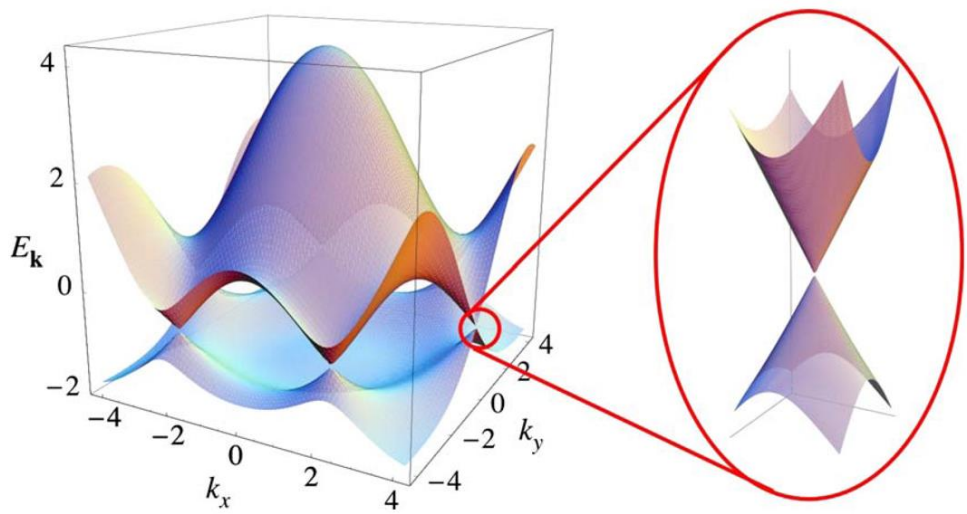

Figure 2 Schematic energy band diagram of graphene. The image was adapted from Neto [1].

1.2 Synthesis of Graphene

For electronic application, high quality graphene should be prepared by scalable method. The mechanical exfoliation of graphene from graphite produces a superior quality graphene, but the size is limited to micrometer [5]. Large scale graphene was first grown by using silicon carbide (SiC) substrate. The graphene can be epitaxially grown on Si-terminated (0001) face by successive annealing process at high temperature up to 1450℃ [6]. However, strong interaction between SiC surface and graphene introduces large density of the defects [7].

Graphene can be prepared using metal substrate through the thermal decomposition of hydrocarbons or surface segregation of carbon atoms. Graphene has been synthesized on various metals, such as Co[8], Ni[9-11], Pt[12-14], Pd[15], Ru[16-18], Ir[19-21], or Cu [22]. Among these, the polycrystalline Ni and Cu have triggered the industrial interests in these days due to the low cost and scalable production. The graphene deposition on Ni have been successfully prepared, but the main limitation of the utilizing Ni is the layer controllability. The fundamental mechanism of graphene growth on Ni substrate has been explained that the carbon segregation on the surface from bulk during cooling, owing to the stable formation of the Ni-C solution at the high temperature. Therefore rapid segregation of the carbon partially limits the layer control. On the contrary, the uniform high quality single layered graphene have been prepared on polycrystalline Cu [22]. This is due to the different mechanism of the graphene deposition, so the large area of the graphene can be prepared with layer number control. In addition, the thin copper

foil can be easily etched by chemicals, so graphene can be transferred onto desired substrates.

Graphene deposition on copper involves the decomposition of carbon precursor on a copper substrate typically held at high temperature usually up to 1000℃. The carbon precursor can be gas phase such as methane, ethylene, and acetylene, or liquid precursor such as hexane [23]. Schematically, the whole process can be divided as annealing, growth, and cooling step. The residual copper oxide on copper foil is removed at high temperature treatment under hydrogen atmosphere, and the average grain size of Cu is increased in the annealing step (Figure 3). When carbon precursor is collided on the catalysts, it is catalytically decomposed in active carbon which can be attached with other active carbon. This active carbon diffuses on surface, and successive collision with other active carbon grows the graphene lattice (Figure 3d). After the thermal quenching, the graphene can be visualized by the microscopy (Figure 3e), and finally can be transferred to the desired substrates.

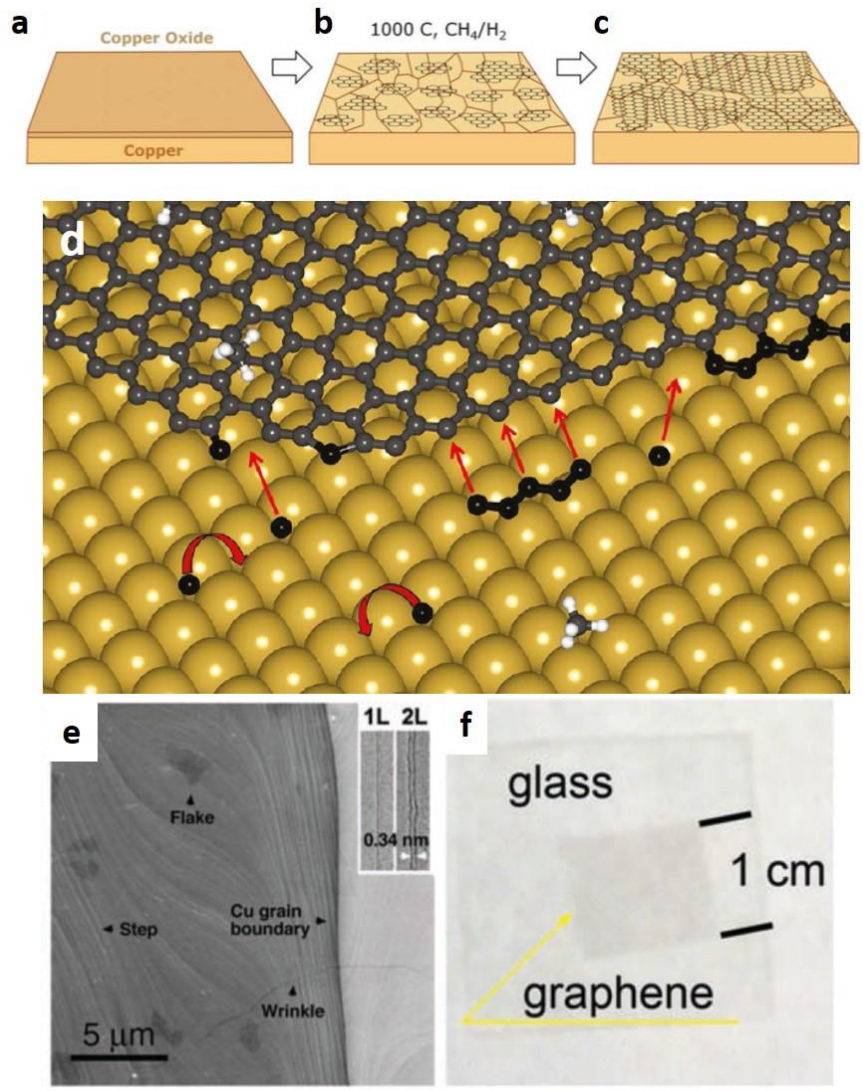

Figure 3 The overview of the graphene deposition on Cu. a-c. Schematic process of the chemical vapor deposition (CVD) of graphene. d. Schematic illustration of the graphene growth. e. Scanning electron microscope (SEM) image of the graphene grown on polycrystalline Cu foil. f. Photo of the graphene transferred on the glass substrate. The images were adapted from [22].

1.3 Interaction between Graphene and Metal substrate

1.3.1 Adsorption and charge transfer of graphene on metal

In many experimental situation, the graphene is placed on the substrate owing to the thin film structure. The atomic and the molecular impurities can induces the change of the electronic properties on the graphene sheet. The properties of the interface between graphene and the metals has been systematically investigated. For example, the transport phenomena was changed with the contact materials due to the work function difference between the graphene and metal contact, which induces the Schottky contact. The weak adsorption of graphene on Al, Ag, Cu, Au, and Pt preserves the band structure of graphene, but in contrast, the strong chemisorption of graphene on Ti, Ni, Co, Pd surfaces perturbs the electronic structure of graphene [24-30].

1.3.2. Surface Reconstruction of Metal Surfaces induced by Graphene

The transferred graphene grown on metal substrate has show the wrinkles which has height and width of several nanometer scale [31-33]. These corrugation of wrinkles strongly influences the properties of the graphene [34]. Although the origin of the wrinkles of graphene grown by CVD technique is not fully understood yet, but the compressive stress during cooling owing to the difference of the thermal expansion coefficients between graphene and metals has been regarded as a main cause of the wrinkle formation [35]. The thermal annealing of graphene sample grown on Cu surface at 400℃ in the ultrahigh vacuum (UHV) condition

induces the surface reconstruction of the Cu [36]. The authors suggested that the residual stress during cooling step after growth is released by the Cu surface atom reconstruction at the annealing, so the periodic stripe pattern was observed.

The direct observations of the wrinkle formation of graphene on Cu have been reported recently [37-40]. The detailed surface topology measured by atomic force microscope (AFM) and scanning electron microscope (SEM) revealed the periodic wrinkles were formed after the CVD synthesis of graphene on Cu foil, which is the result of the Cu step construction in graphene/Cu system [38-40]. The Cu step bunching in the graphene grown system shows significantly different surface morphology, while the Cu annealed at same temperature and cooled with same cooling rate without deposited graphene showed the smooth and flat surface [37]. The periodically formed wrinkle-like Cu step and the thermally induced graphene wrinkle which is non-parallel to the Cu step were suggested as origin of the wrinkle of graphene after transfer [39,40]. However, the mechanism of the wrinkle-like Cu step formation is not fully revealed.

Recently, several groups reported the wrinkle-like structure formation of the Cu step. The vermicular ripple formation was observed by Paronyan *et al.*, which suggests the instability of the dilute Cu-C phase during cooling starts from high temperature is the origin of the ripple-like Cu step bunches formation [41]. In addition, the grain-dependent surface step formation was observed by Kim *et al.*, who suggest that the strain relaxation between graphene and the Cu lattice induces the Cu step [42]. Considering these results, copper surface morphology would be

reconstructed by the minimizing the entire energy of the graphene-copper interface. Although surface reconstruction has been regarded to occur during cooling stage, but in recent, the surface reconstruction of graphene/Cu was directly observed by Wang *et al*. using *in situ* environmental scanning electron microscope (ESEM) [43]. The direct observation by ESEM shows the surface reconstruction of copper occurred at the temperature range of 750℃ to 520℃.

1.4 Raman Spectroscopy of Graphene

Interest in studying the fundamental properties of graphene has grown in recent years since the discovery of method to identify the structure of graphene. Raman spectroscopy in graphene has been investigated thoroughly, and as a results, the structural information and behavior of electrons and phonons in graphene can be characterized by the simple method.

The interaction between the electron-hole pair and the phonon in graphene has critical role for Raman scattering in graphene. To understand the mechanism of the Raman scattering, the phonon dispersion of graphene is essential. The unit cell of monolayer graphene contains two distinct carbon atoms, thus there are six phonon dispersion bands (Figure 4). Each phonon branch is assigned as in-plane (i) or out-of-plane (o), transverse (T) or longitudinal (L), acoustic (A) or optic (O). The Raman active modes for the planar graphene are the in-plane iTO and iLO modes, which are degenerate at the zone center (Γ). The phonon modes around the *K* are important, because the resonant Raman bands in graphene are related to

phonon modes around at *K* point [44].

The characteristic features in the Raman spectra of monolayer graphene are the *G* band located at around 1580 cm^{-1} and the 2*D* band located at about 2700 cm^{-1}. In the case of the disrupted samples with defects, the *D* band which has half of frequency of the 2*D* band (~1350 cm^{-1}) is activated (Figure 5). Each of the band is related to the different phonon modes. The *G* band is associated with the doubly degenerate phonon mode at the Brillouin zone center [44]. On the other hand, *D* and 2*D* bands are originated from a second-order process, involving two iTO phonons near the *K* point for the *2D* band or one iTO phonon and one defect in the case of the *D* band. Each process can be schematically expressed as Figure 6. In a pristine graphene without defect, the *G* and the 2*D* bands are only measurable, since the 2*D* bands can be activated without defect owing to the two iTO phonons only responsible for the scattering process [45].

The Raman process can also occur by scattering of holes. In graphene with imbalanced electron-hole density, the triple resonance condition can be achieved. The electron-hole excitation followed by the phonon scattering by both electron and holes, and finally recombination between electron and hole can also activate the 2*D* band [46] (Figure 6b bottom). The triple resonance condition might explain why the 2*D* band is more intense than the *G* band in monolayer graphene [44].

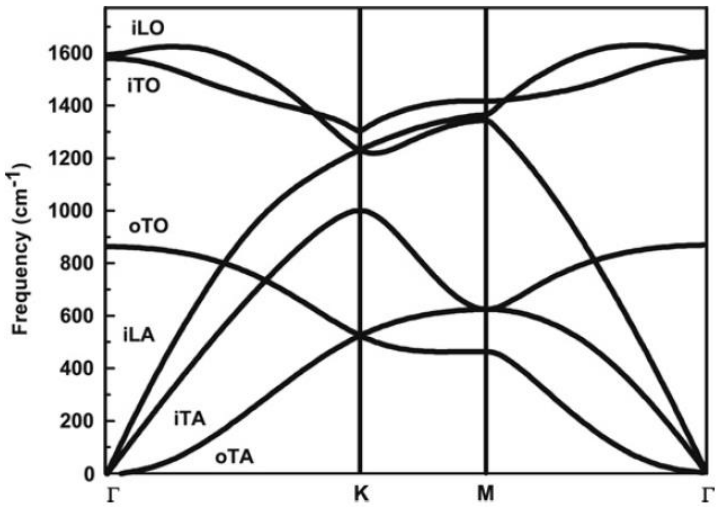

Figure 4 Calculated phonon dispersion relation of graphene. The image is adapted from the Malard *et al*. [44].

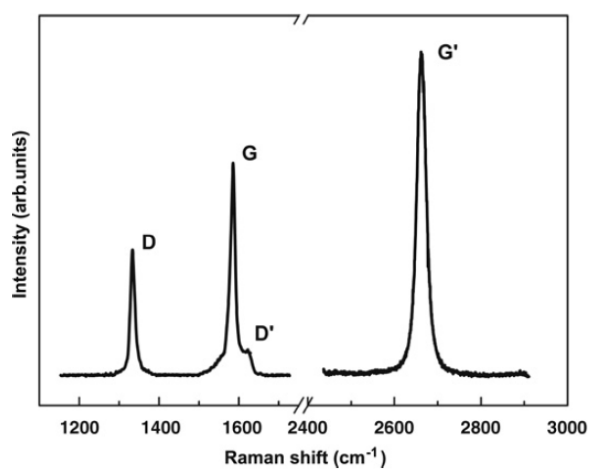

Figure 5 Characteristic Raman spectrum of a defected graphene. The spectrum was collected at the graphene edge, which has defects in lattice. The image is adapted from the Malard *et al*. [44].

1.4.1. Characterizing the number of layers

The structure information of the graphene can be investigated by the Raman spectroscopy. Starting from the monolayer graphene, the double resonance process of the monolayer graphene (Figure 6b) activates the 2*D* band of the graphene. In defect-free pristine graphene, the double resonance and the triple resonance process of the 2*D* band shows larger peak of 2*D* band than G peak, and *D* peak is not activated due to absence of the defect (Figure 7, top).

In the case of bilayer graphene, the structural difference changes the Raman scattering process. The electronic band structure of the bilayer graphene is composed of the parabolic bands, the two conduction bands and two valence bands (Figure 7, bottom). The interlayer interaction affects the electron motion, so the band split into symmetric and anti-symmetric components. As a result, the double resonance conditions are more complex than that of monolayer graphene. The schematic illustration of the double resonance process in bilayer graphene is showed in Figure 7. Owing to the split of the electronic bands, the double resonance process split into four modes. These four different process contributes each modes with different frequency, thus the 2*D* band of the bilayer graphene is composed of four peaks, which can be deconvoluted by the Lorentzian function [47].

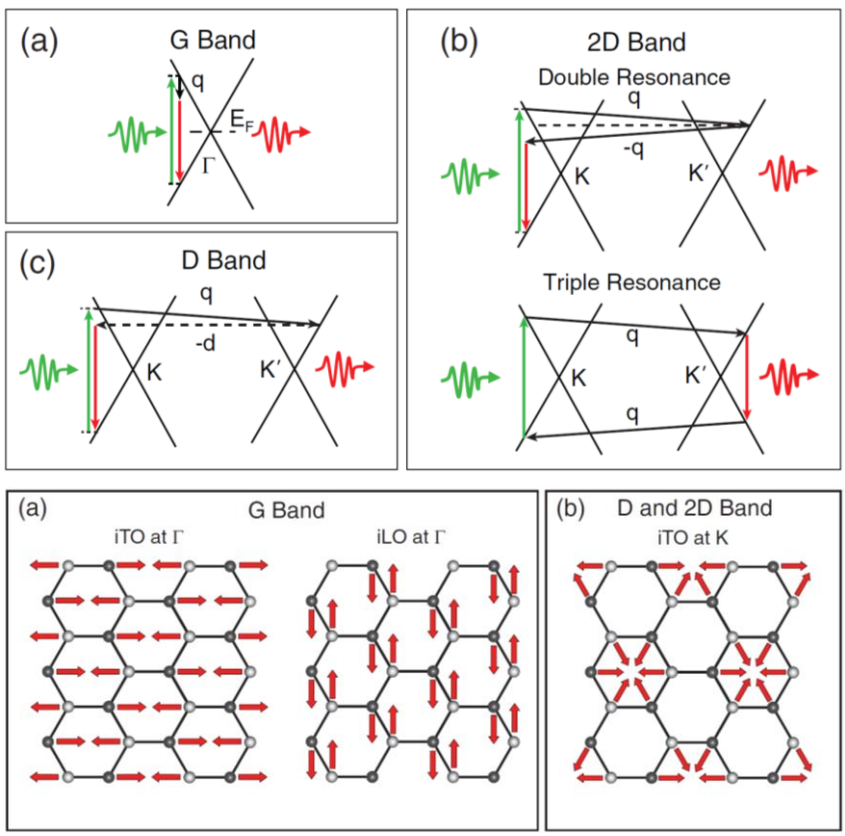

Figure 6 Schematic illustration of the Raman scattering process. a-c. the Raman process of the *G*, *2D*, and the *D* bands. (bottom) a-b. the schematic vibration modes of each band. The image is adapted from the Beams *et al*. [45].

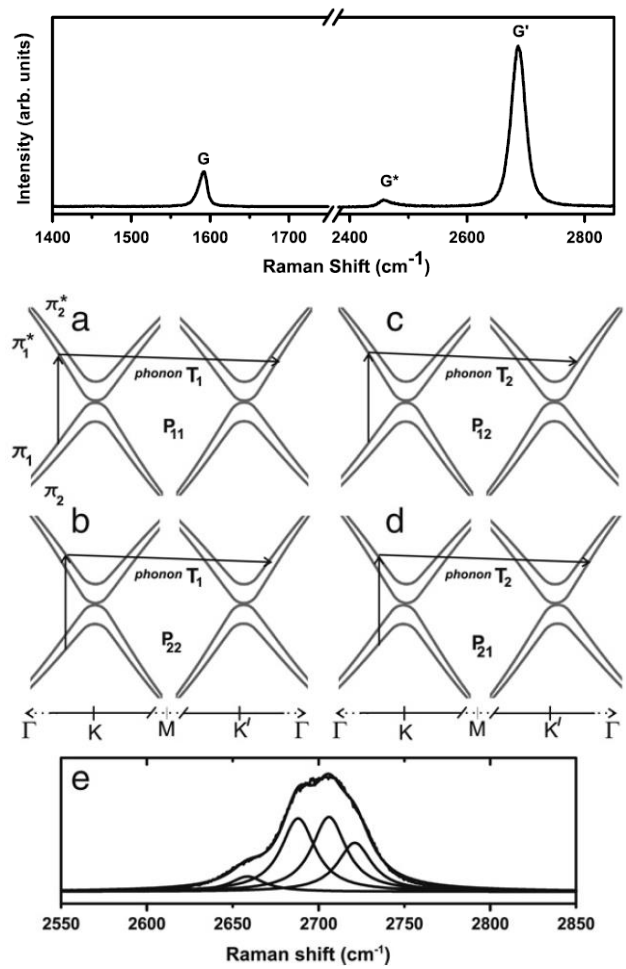

Figure 7 The spectrum of pristine monolayer graphene, and schematic illustration of the double resonance Raman process of bilayer graphene. (upper) The spectrum of defect-free monolayer graphene. (bottom) a-d. Double resonance process of bilayer graphene. e. Raman spectrum of 2*D* band of bilayer graphene. The image is adapted from the Malard *et al*. [44].

1.4.2. Estimation of charge doping on graphene

Graphene is sensitive to changes in carrier concentration owing to the linear electronic dispersion of the band structure. The doping level in graphene can be characterized by Raman spectroscopy. The G and 2D bands are both strongly depends on the carrier concentration of graphene.

The position and the width of the G band change with doping level. When the Fermi level is shifted from the origin, two effects are occurred. First, the Fermi level upshift/downshift changes the equilibrium constant, which induces the phonon stiffening and softening [48]. The second effect is related to the Kohn anomaly at the zone center of Brillouin zone in the phonon dispersion [49]. Increasing Fermi level reduces the number of electronic states that are available as decay pathways due to the Pauli exclusion principle, thus the result makes linewidth of the G band narrow [50]. The experimental demonstration by electric field effect doping clearly showed the dependence of the position and the FWHM of the G peak (Figure 8). Both electron and hole doping, the position of the G peak was upshifted, and the FWHM decreases with the increase of the carrier concentration [50].

The position of the 2D band also depends on the Fermi level. As well as the G band, the phonon stiffening/softening makes the change in the position of 2D band. The 2D band is increased for both electron and hole concentration increases, but 2D band goes soften and frequency decreased at the high electron density (Figure 8c).

In addition to the width and the position of the bands, the relative intensity of the G to 2D bands also changes. At low doping levels the G band intensity is independent of Fermi level, while the 2D band intensity decreases as Fermi level increases [51]. Since all the intermediate states of the 2D band are resonant with electronic levels, the intensity is sensitive to electron-phonon coupling [51]. Therefore, by tuning Fermi level and measuring the intensity of the 2D band, the electron-phonon scattering rate can be determined [52]. It will be discussed in more detail in chapter 3.

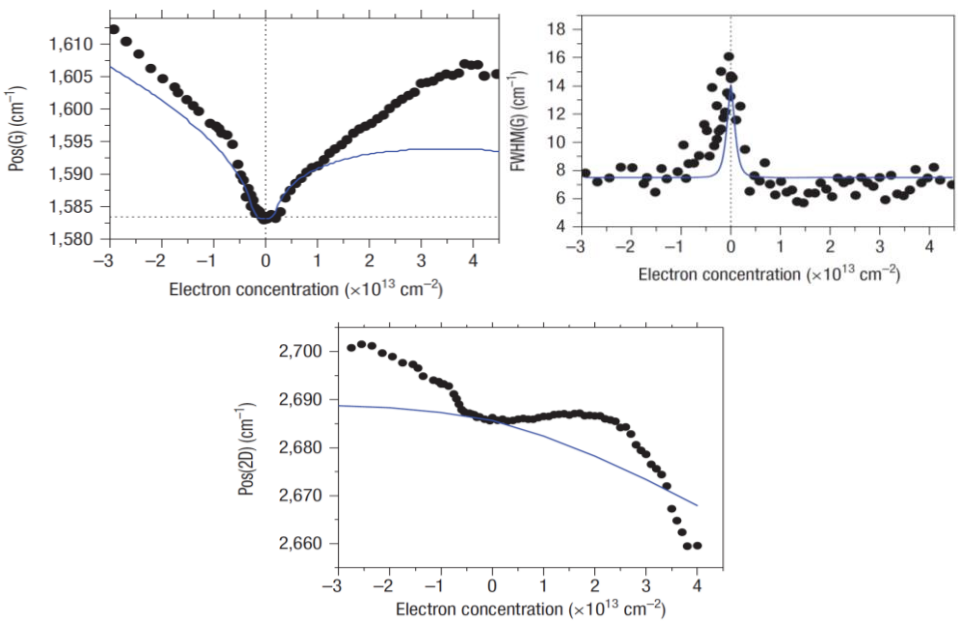

Figure 8 The position and the FWHM of the peaks to the carrier concentration. a. position and the b. FWHM of the G peak. c. position of the 2D peak. The image is adapted from the Das *et al*. [50].

Chapter 2

Synthesis of Graphene on Cu Foil and Morphology Evolution

2.1 Synthesis of graphene on Cu foil

Graphene was synthesized by CVD method using Cu foil as a catalytic substrate. The rolled Cu foil has high purity (99.9%) with dilute concentration of residual metals such as Fe, Ti, Sn, Mo, Sb, Ag. The total concentration of residual metals was under 700 ppm. The Cu foil was used as received without any treatment. The Cu foil was placed in quartz tube, and the chamber was under vacuum with background pressure under 2.3×10^{-4} Torr which is the lower bound of the pressure gauge. After that, hydrogen gas was introduced with flow rate of 5 sccm, and chamber pressure was constantly kept at 42 mTorr. The temperature of the chamber was linearly increased with programmed furnace in 1h. At the high temperature under hydrogen atmosphere reduces the residual oxide on Cu surface and grows average grain size of the Cu. The programmed final temperature of the furnace at the annealing step was 1000℃, and was kept during the growth step. After the annealing step, the flow rates of the hydrogen and the methane were 5 sccm and 35 sccm at total pressure of 5.4×10^{-1} Torr , which correspond to hydrogen partial pressure of 68 mTorr and methane partial pressure of 473 mTorr. The temperature and the flow rates were kept constant for 30 min to ensure the full growth of graphene. After the growth step, the methane flow was terminated and the furnace was slid to the other side of the chamber to cool Cu foil rapidly. The temperature and the gas composition was summarized in Figure 9.

The temperature of the chamber was measured by thermocouple. The temperature outside of the chamber was 1000℃ as we programmed, but the temperature was

about 70℃ lower at the inside of the chamber. This is because our system has large diameter of chamber, so heat loss was significant. Although the temperature significantly deviates to position, the temperature was stable ~935℃ at the center of the furnace (Figure 10a). Therefore, the Cu foil was strictly placed at the center of the furnace. The cooling rate was also measured with thermocouple, and the half of the growth temperature was reached within ~ 5 min (Figure 10b).

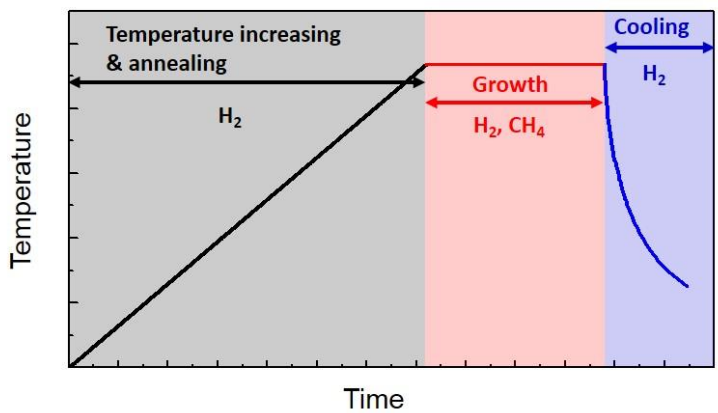

Figure 9 The temperature profile and gas composition at the annealing, growth, and the cooling step of the CVD process. Time and the temperature are expressed in arbitrary unit.

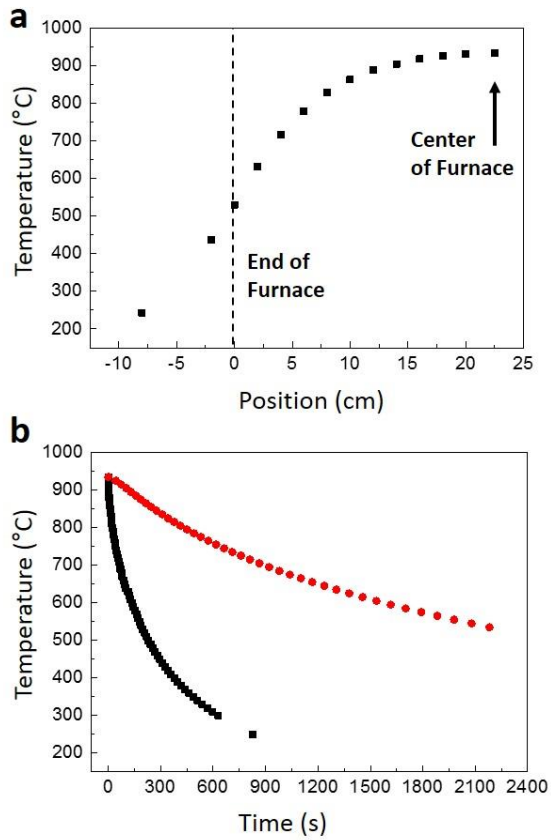

Figure 10 The temperature variation to the position and the cooling profile. a. Temperature variation was measured by thermocouple inside the chamber. At the center of the furnace, about 10 cm of the zone shows low temperature variation. b. Cooling profile of the rapidly cooled case (black dot) and the slowly cooled case (red dot).

2.2 Morphology change of the Cu foil

After the graphene synthesis, the Cu foil was shinier and softer than the untreated bare Cu foil observed with naked eye. The optical microscope images show the surface of the Cu foil has significantly changed after the graphene synthesis (Figure 11). The optical microscope image of bare Cu foil showed rolling mark and invisible grain. On the contrary, the optical microscope image of graphene grown Cu foil clearly showed enlarged Cu grain which size is up to ~ 100 μm separated by grain boundary. This is the result of the high temperature at the annealing and growth step which proceeds Cu recrystallization [37]. At the high magnification, the detailed microstructure of the Cu surface was visualized. Under the dark field microscope, the distinct feature was observed in the 4-fold shaped region (Figure 12). The size of each 4-fold shaped region was about 5 μm, and the wave-like structure was inferred by the image. The dark field optical microscope image of other sample grown in similar condition clearly confirms the wave-like structure in the 4-fold shaped region (Figure 12c). The shape of the 4-fold region is similar to the shape of the graphene islands grown in low pressure condition [53,54], so these regions might be covered with the bilayer graphene, which will be thoroughly discussed later.

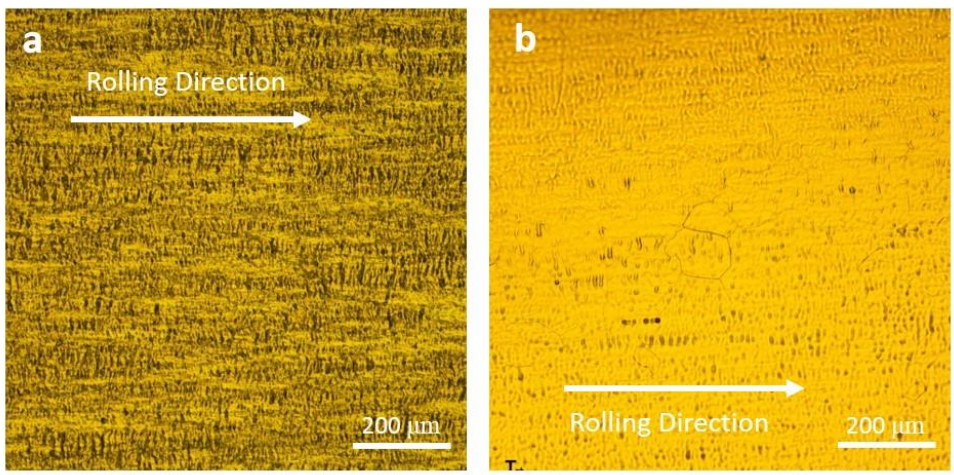

Figure 11 Optical microscope images of bare Cu foil and graphene grown Cu foil at low magnification. Optical microscope image of the a. bare Cu and b. graphene grown Cu. The direction of the rolling mark is expressed in figures.

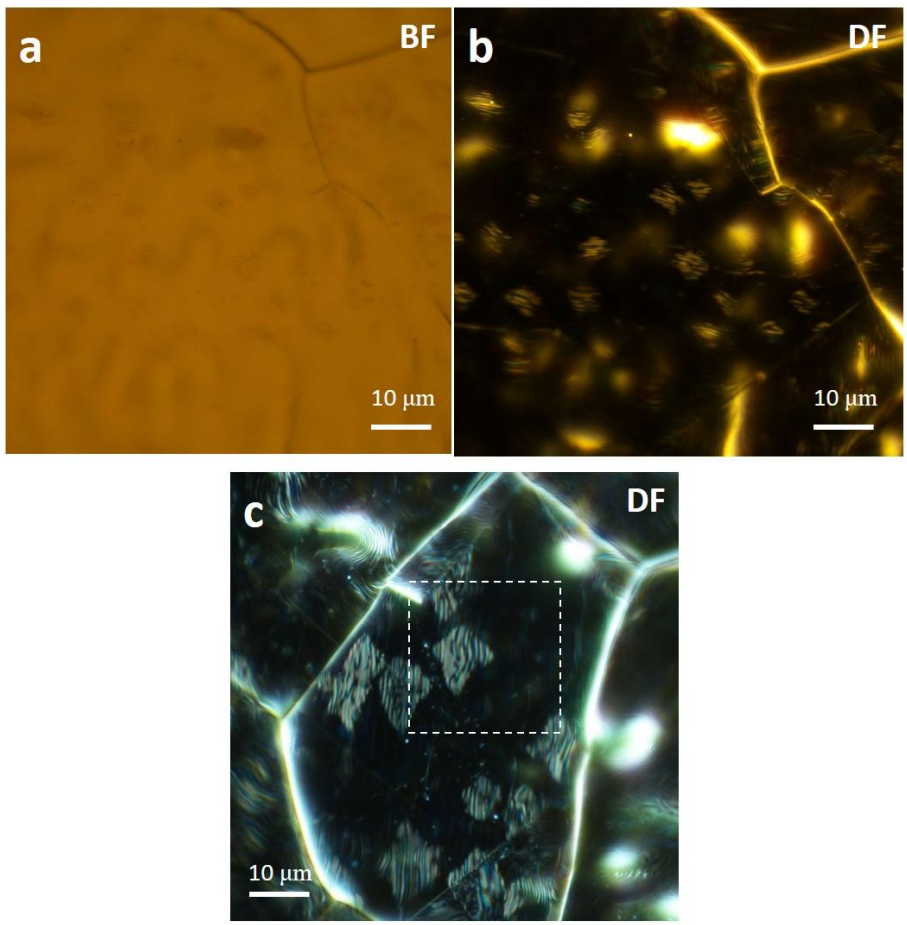

Figure 12 Optical microscope images of the graphene grown Cu surface at high magnification. a. Bright field image and b. dark field image of the graphene grown sample. c. The dark field image of the sample grown in other batch.

2.3 Atomic force microscopy

To investigate the morphology of the Cu surface more precisely, surface was imaged by atomic force microscopy (AFM). All images were taken by non-contact mode (XEI-100, Park System) using silicon nitride tip.

To ensure the feature observed by the optical microscope is due to morphology of the Cu surface, AFM image was taken with large scan size of $35\times35\ \mu m^2$ which is marked as white dashed box in Figure 12c (Figure 13). The topology of the area measured by AFM was exactly same with the image of the dark field microscope. The hills and valleys up to ~ 100 nm was exist which would be the result of the sublimation of Cu, and wave-like structure clearly formed in 4-fold shaped area. The topography and phase image of the smaller scan area showed the difference in background area and 4-fold shaped area (Figure 14). The wave-like structure was formed in both region, but wavelength and the intensity at the 4-fold shaped area was obviously larger than at the background region. The structure was coherently transitioned at the boundary. The wavelength at the 4-fold shaped area was ~ 500 nm and the intensity was ~ 20 nm, which is almost double of the wavelength and intensity at the background (Figure 14e). To give rough intuition, we will introduce the surface area ratio, which is determined as

$$\text{(Surface area ratio)} = [\text{(Surface area)}/\text{(Geometric area)}]\times100\ (\%)$$

The surface area ratio calculated from the Figure 14a was slightly higher inside the 4-fold shaped region (~ 0.75%) than the background region (~ 0.49%). As a result, the surface area of the both region is almost same.

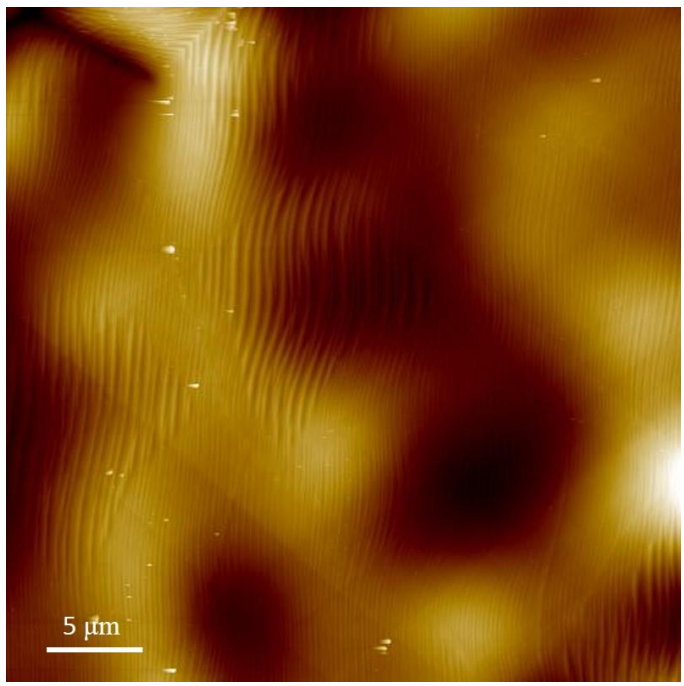

Figure 13 Atomic force microscope (AFM) image of the region which is assigned in Figure 5.

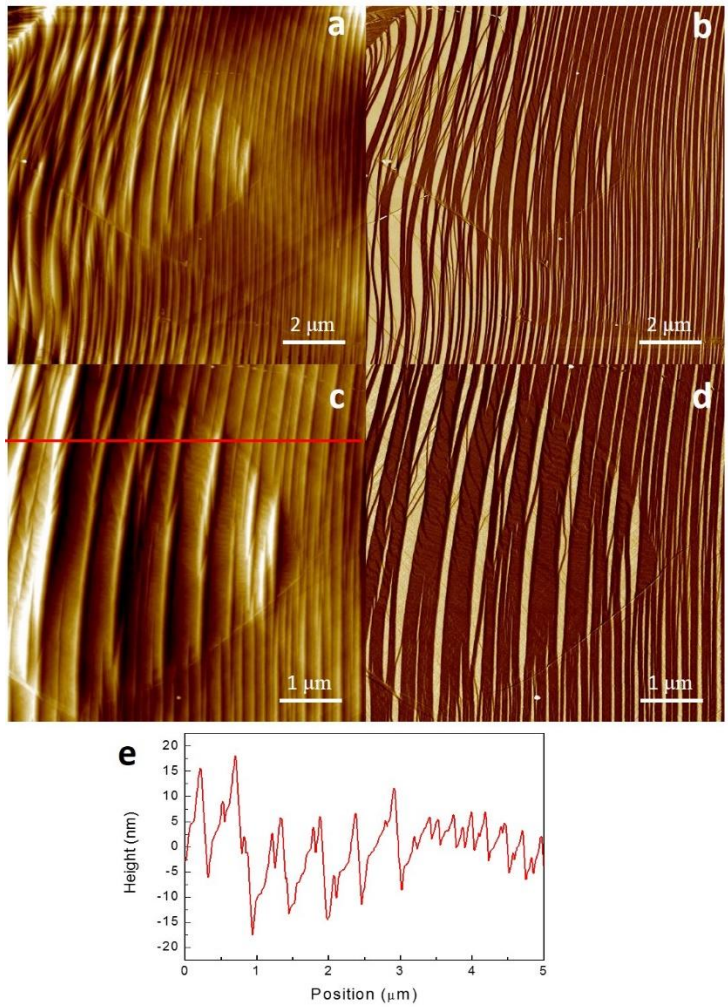

Figure 14 Detailed AFM images of the 4-fold shaped region. a. Topography and b. phase image of the 4-fold shaped region with scan size 10×10 μm^2. c. Topography and d. phase image of the 4-fold shaped region with scan size 5×5 μm^2. The scan rate of all images was 0.5 Hz. e. Line profile of along the red line assigned in c.

2.4 Discussion

The wave-like structure that was mainly observed in our experiments has been reported. In previous reports, the wave-like structure was called ripple or wrinkle, thus we will use these terms to keep coherence with other works. The origin of the ripples of graphene synthesized by CVD method has been observed and explained as several ways. During the annealing of Cu foil and growth of graphene, the temperature inside the chamber is up to 1000℃, which is close to the melting point of the Cu (1084℃). In this high temperature, although bulk copper is not melted, the surface can be pre-melted due to the less bonded unstable surface atoms, resulting thin mobilized Cu film outside of the bulk Cu. In the low pressure under 10^{-3} mbar, the pre-melted Cu film more dominates the surface property, so vaporized or sublimated Cu may change the surface morphology of the Cu. Surprisingly, tendency of the surface reconstruction when graphene was covered on Cu surface is far different than the case of Cu surface uncovered with graphene [36,37,55]. This surface reconstruction of Cu is suggested by the deceleration/pinning of mobile Cu atoms under graphene [36, 55], or the different thermal expansion coefficient between graphene and Cu [37,56]. In addition, the instability on the interface of Cu-C alloy system was also suggested as a responsible factor of the ripple formation [41].

Each of the suggestion may explain the surface reconstruction of Cu under graphene, however, once the graphene film is grown and emerged making entirely connected film, the situation would be little different. When the graphene covered

the entire Cu surface, the fast Cu atoms on surface may be absence because most of the surface Cu atoms interact with graphene. Therefore, the interaction between Cu surface and graphene would be the more important factor for Cu surface morphology evolution. In recent, the surface reconstruction under graphene is observed *in situ* by environmental scanning electron microscope (ESEM) [43]. The *in situ* observation clearly showed that the reconstruction of copper surface is occurred during the cooling step, not during the growth step. This result might confirm the surface reconstruction of Cu is the result of the interaction between graphene and Cu, specifically the stress relaxation due to the lattice mismatch [42]. However, the precise origin of the surface reconstruction seems remained in question yet.

As we used relatively low purity copper than pure copper (99.999%), our system might resemble with the work by Paronyan *et al*. [43] However, although we found that the either vermicular ripple or cell were formed inside several Cu grain similar as the previous report, the transition of wavelength and intensity was clearly occurred in the 4-fold shape region (Figure 15). Therefore, the transition of the wrinkle under the specific area would be the universal phenomena in our system.

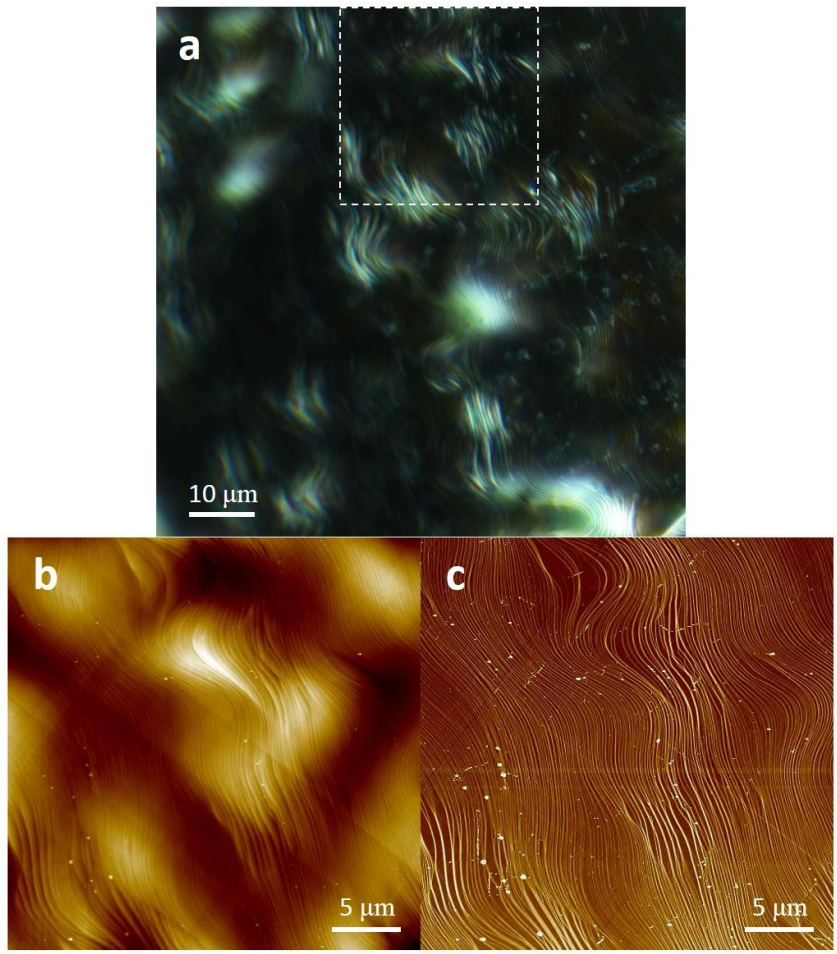

Figure 15 Morphology of Cu at other grain. a. Dark field optical microscope image of the field. The vermicular ripple (wrinkle) was observed in this grain. b. Topography and c. phase image of the area marked in a (white dashed box). The vermicular ripple and the transition of ripple (wrinkle) in the 4-fold shaped region was clearly observed. The scan area of the b and c was 30×30 μm^2, and scan rate was 0.2 Hz.

Chapter 3

Raman Spectroscopy Study

3.1 Characterizing the number of layers of graphene

The Raman spectroscopy is a promising tool for characterizing the graphene as we discussed in the earlier section. The number of the layers of graphene can be determined by two ways. First is the deconvolution of the 2D peak, and second is the comparing the ratio of the intensity of the G peak and the 2D peak. Either methods can determine the number of layers of graphene precisely.

Before the spectrum collection with detailed spatial correlation, the morphology of the field was determined by the optical microscope and AFM. Both bright field and dark field optical microscope images showed the wave-like structure that we found in the earlier section, and the AFM topology image confirms the wrinkle of the surface (Figure 16). The transition of the wrinkle was coherent (Figure 16c), and the line profile shows the wavelength and the intensity was significantly increased at the 4-fold region (Figure 16d). To determine the layer number of the graphene, Raman spectrum was obtained at the each region marked as yellow a, b in Figure 1c. The Raman spectrum was collected with a WITEC confocal spectrometer through X100 objective lens which has numerical aperture of 0.95. The wavelength of the laser was 532 nm (2.43 eV), and laser power was kept under 2 mW to avoid local heating. The spectral resolution was determined by fitting the Rayleigh scattering line to a Gaussian function, and the spectral resolution was 12.6 cm^{-1}. The spectra obtained at a, b show different features with each other (Figure 17). To compare with unstrained, and charge neutral graphene, spectra obtained from the exfoliated graphene on SiO_2 were also

presented in Figure 2 c, d for monolayer and bilayer graphene. The spectrum acquired from the exfoliated monolayer graphene showed intense peak around 2680 cm^{-1}, and single Lorentzian function was fitted (Figure 17c). The FWHM of the peak was about 30 cm^{-1}, which is the well adapted to the undoped monolayer graphene [47]. On the other hand, the spectrum of the exfoliated bilayer graphene showed intense peak around 2700 cm^{-1} with broader FWHM (Figure 17d). This upshifts and broadening of the 2D band is due to the change of the electronic band structure of the bilayer graphene, which splits the 2D peak into 4 components [47]. The peak was well fitted with four Lorentzian peaks and the linewidth of the each peak was around 20~30 cm^{-1} as similar to the result reported previously. The spectrum acquired from the graphene grown graphene, specifically at region a shows similar feature of the exfoliated sample (FWHM ~ 30 cm^{-1}), except the blue shift of the peak. This blue shift of the 2D peak without broadening indicates the phonon stiffening without significant symmetry breaking of the graphene lattice. Therefore, the Raman spectrum clearly indicates the graphene lattice was compressed biaxially [57]. On the other hand, the spectrum acquired at region b shows broaden peak which is clearly split into four Lorentzian peaks, indicating the bilayer structure. The linewidths of the peak were around 20~30 cm^{-1}, similar to mechanically exfoliated bilayer graphene sample. The peak position was located around 2710 cm^{-1}, and four peaks were upshifted around 10 cm^{-1} than exfoliated sample, without significant broadening. Thus, bilayer graphene was also biaxailly compressed. By comparing the frequency and the linewidths of graphene 2D band, the layer number can be determined. In summary, the monolayer graphene is grown

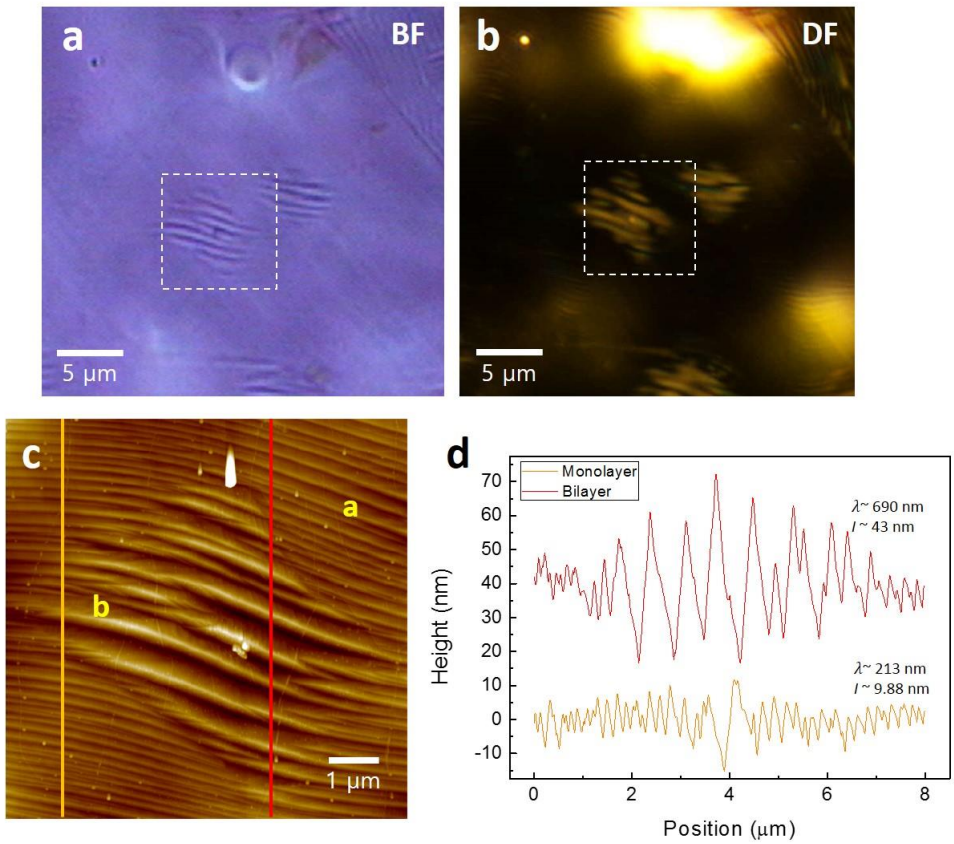

Figure 16 Surface morphology of the field. a. Bright field and b. dark field optical microscope images of the field. c. AFM topology image of the area marked as white dashed box in a and b. the scan size was 8×8 μm^2 and the scan rate was 0.2 Hz. d. Line profiles of the orange and red line in the c.

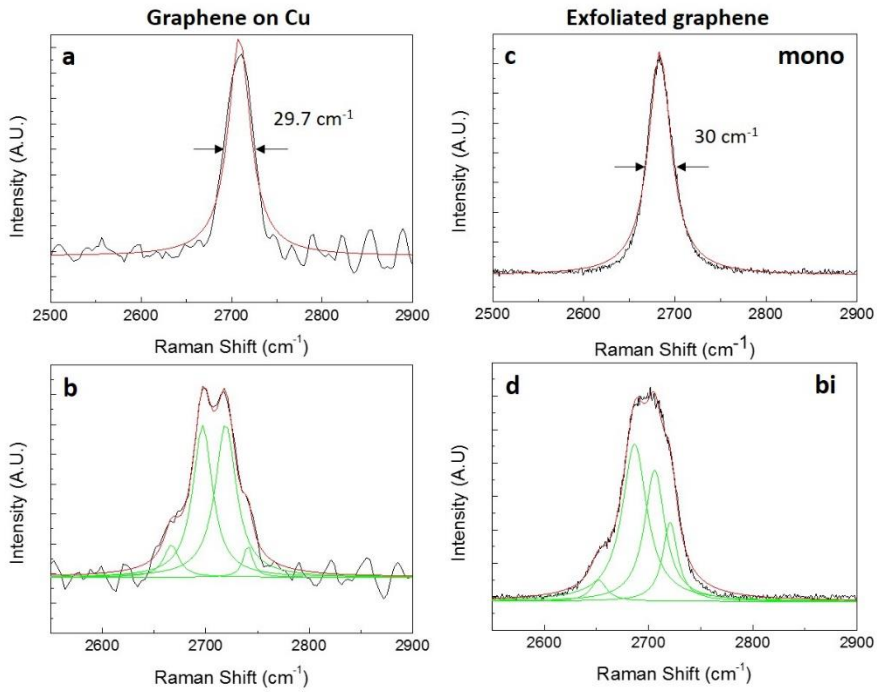

Figure 17 The 2D peak of the graphene on Cu and exfoliated samples. a. b. was collected spectrum at point marked in Figure 1c. The Raman spectrum of a. monolayer and b. bilayer prepared by mechanical exfoliation of graphite. The source wavelength was 532 nm.

in region a and the bilayer graphene is grown in region b in the Figure 1c. In this stage, we can find that the surface geometry and the layer number of the graphene should be closely related to each other.

To determine the geometry of the graphene, spectrum was obtained with exact spatial coordinate using microstage. The spectra were obtained in white dashed box shown in Figure 18 a, b. Acquired spectra were fitted with Lorentzian to precisely determine the position, intensity and FWHM of the peaks. After the data processing, the Raman map was plotted for the FWHM of the 2D peak (Figure 18c), and the intensity ratio I(G)/I(2D) (Figure 18d). Because either the FWHM of the 2D peak and I(G)/I(2D) is sensitive to the number of layers, the number of layers of graphene can be determined with these factors. The FWHM of the 2D peak at narrow wrinkle region (a in Figure 16c) is distributed around 30 cm^{-1}, and the FWHM of the 2D peak at wider wrinkle region (b in Figure 16c) is distributed around 48 cm^{-1} (Figure 18c). The value is well matched with FWHM(2D) of monolayer graphene (~ 30 cm^{-1}) and the bilayer graphene (~ 50 cm^{-1}) by fitting of single Lorentzian function. The Raman map gives distinctive feature of the FWHM(2D) change, and the shape of the Raman map is closely correlated with the shape observed by optical microscopy and AFM. Therefore, the region a, b in Figure 16 are revealed as monolayer and bilayer graphene as we first studied by point spectrum. In addition, there are FWHM up to 60 cm^{-1} in the center of the bilayer graphene. This would indicate the existence of the graphene with number of layers over three, due to additional 2D modes than bilayer graphene. On the other hand, the intensity ratio I(G)/I(2D) was also gradually increased in monolayer

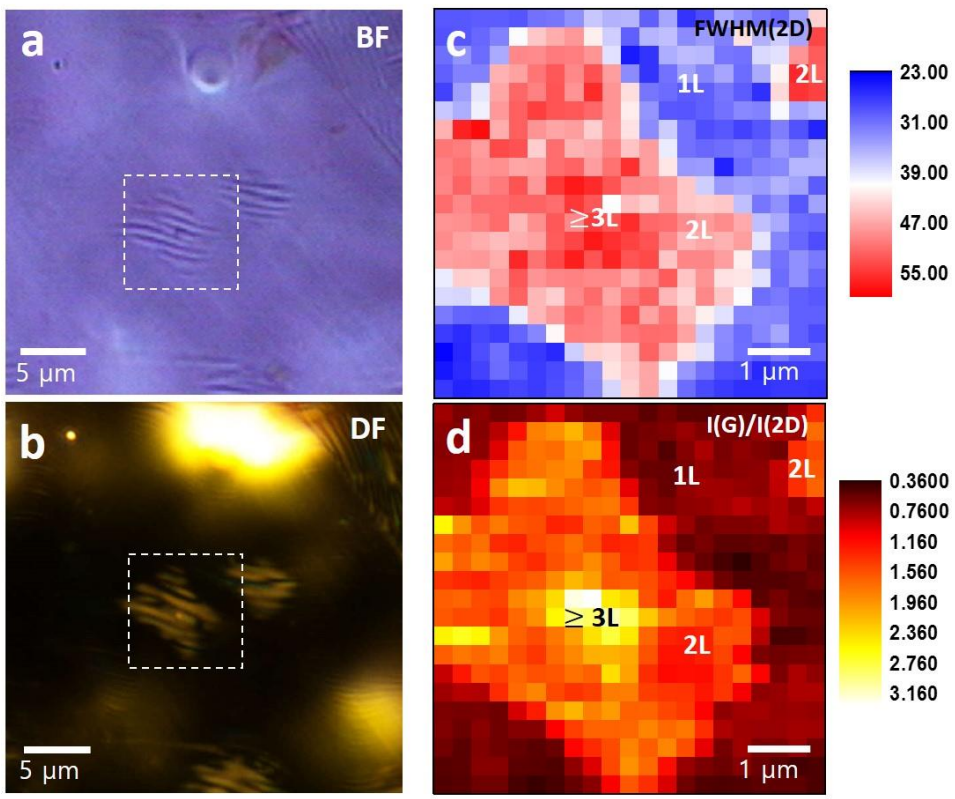

Figure 18 Raman map indicating layer number of the graphene on Cu. a. Bright field and b. dark field optical microscope images of the field. Raman map composed of c. Full width of half maximum (FWHM) of the 2D peak, and the d. intensity ratio I(G)/I(2D). the distance between the pixel is about 0.3 nm. The unit of the scale in c is cm^{-1}.

graphene, bilayer graphene, and the center of the bilayer graphene (Figure 3d). This Raman map also gives clear distinctive feature. To give relation between these two factors (FWHM(2D) and I(G)/I(2D)) and the number of layers of graphene clearly, values from all points were extracted and averaged (Figure 19). The value of the average and the standard deviation is given in Table 1. By combining these two Raman map, we can conclude the monolayer graphene was grown in the entire surface with narrow wrinkle structure, whereas the bilayer graphene is grown on wider wrinkle structure.

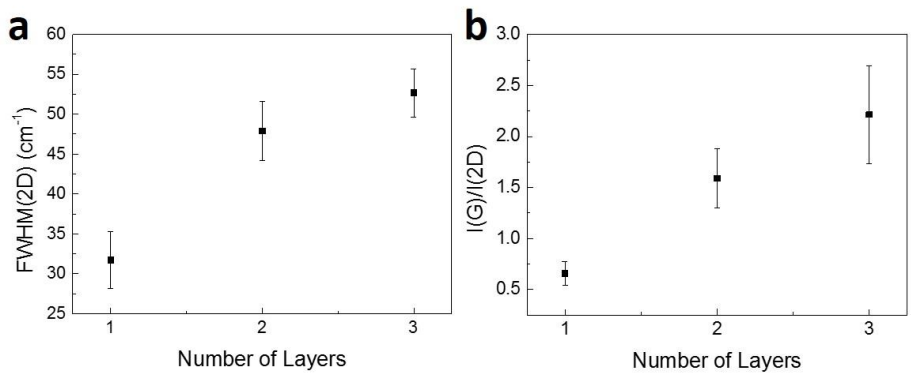

Figure 19 The average of the FWHM(2D) and the I(G)/I(2D). a. Average value of FWHM(2D) and b. I(G)/I(2D) to the layer number of graphene. The data points of the each layer number were collected from the map, and were sorted by referring the feature of the Raman map. The values at the boundary was rejected to calculate the value accurately.

Table 1 The value of the FWHM(2D) and the I(G)/I(2D) in Figure

Number of Layers	Avg. FWHM(2D) (cm^{-1})	Standard dev. FWHM(2D) (cm^{-1})	Avg. I(G)/I(2D)	Standard dev. I(G)/I(2D)
1	31.7	3.55	0.66	0.12
2	47.9	3.68	1.59	0.29
3	52.7	3.03	2.21	0.48

3.2 Strain estimation via peak shift

The phonon frequency of the graphene can be modulated by the external strain. As the tensile strain makes the lattice equilibrium distance longer, phonon will be softened, while the compressive strain makes phonon stiff due to shortened lattice equilibrium distance. The change of the phonon frequency can be detected using Raman spectroscopy. The characteristic peaks of the graphene (the G peak and the 2D peak) is shifted when graphene is under tensile/compressive strain, as the phonon softening/stiffening changes the scattering energy for phonon excitation in Raman scattering process.

The graphene can have residual strain after the synthesis. The large different thermal expansion behavior introduces the strain in graphene lattice. The negative thermal expansion coefficient of the graphene at room temperature and one order larger thermal expansion coefficient of Cu expect the total compression of graphene would be about 1.8 % in thermal quenching process starts from 1200 K to 300 K [58.59]. Several works suggested the ripples and wrinkles are formed to release this large strain [56]. However, the graphene-metal interaction is still not fully understood yet. In example, the biaxial compressive strain was linearly increased within increasing growth temperature from 900℃ to 1100℃ in the demonstration by Yu *et al*., but the compressive strain range is between 0.1% to 0.5% which is smaller than expected compression [60]. This reason of this result would be the stress relaxation by ripple or wrinkle formation and the defect pinning at the high temperature, but not exact reason has been revealed.

To investigate the relation between the number of layers of graphene and the residual strain after the synthesis, we compared the shift of the G peak and the 2D peak. The sensitivity of the phonon frequency to the strain is described by Grüneisen parameter. The Grüneisen parameter γ is defined for uniaxial strain ε as

$$\gamma_{\mathrm{uni}} = -\frac{1}{\omega_0}\frac{\partial\omega}{\partial\varepsilon}$$

where ω_0 is the Raman frequency at zero strain [61]. Under biaxial strain, due to the same amount of the strain in longitudinal and transverse direction, Grüneisen parameter is

$$\gamma_{\mathrm{bi}} = -\frac{1}{2\omega_0}\frac{\partial\omega}{\partial\varepsilon}$$

The Grüneisen parameters have been measured for both uniaxial strain and biaxial strain [61-64]. Reported Grüneisen parameters are different in each study, ranging from 1.8 to 2.4 for G peak, and 2.6 to 3.8 for 2D peak (Table 2). We first hypothesized the strain resides in graphene is biaxial strain, so the values of Raman peak shift to the applied biaxial strain from the reference [62] ($\partial\omega_{\mathrm{G}}/\partial\varepsilon \sim -57.3$ and $\partial\omega_{2\mathrm{D}}/\partial\varepsilon \sim -160.3$) were adapted first.

Table 2 The Grüneisen parameters for the biaxial strain

Reference	$\Delta(2D/G)$	$\gamma(G)$	$\gamma(2D)$
[61] exp.	3.03	1.99	3.55
[61] calculated	2.48	1.8	2.7
[62]	2.8	1.8	2.98
[63]	2.63	2.4	3.8
[64] monolayer	2.45	1.8	2.6
[64] bilayer	1.9-2.5		

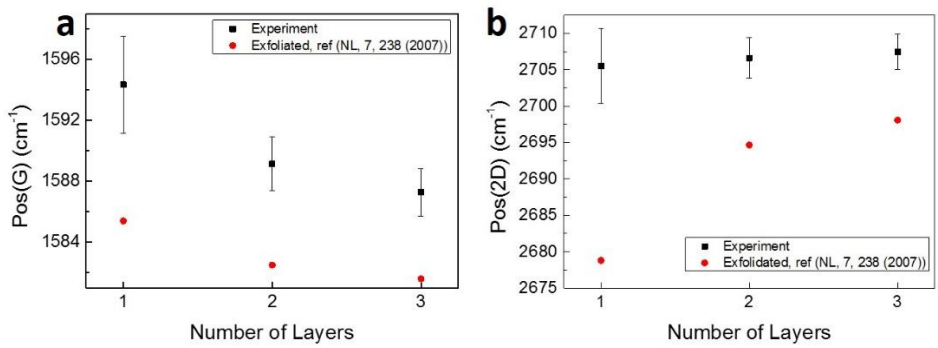

Figure 20 The average of the position shifts of the G peak and the 2D peak. a. G peak position and b. 2D peak position shift of the data collected from the Raman map. The reference position of the G peak and the 2D peak of mechanically exfoliated graphene using 532 nm excitation was plotted together (red circle).

Table 3 The shift of the peaks and the estimated biaxial strain

Number of layers	$\Delta\omega_G$ (cm^{-1})	$\Delta\omega_{2D}$ (cm^{-1})	Predicted strain (%)	Predicted strain (%)
1	8.95	26.7	-0.156	-0.167
2	6.63	11.95	-0.116	-0.075
3	5.67	9.38	-0.099	-0.059

To estimate the strain on graphene, the peak shift of the G peak and 2D peak was plotted (Figure 20). The data was sorted by the number of the layers, which was clarified by the Raman map of the FWHM(2D) and the I(G)/I(2D). In addition, the position of the G peak and the 2D peak of the exfoliated graphene acquired using laser excitation of 532 nm wavelength was collected from the reference [65] to compare data with the unstrained neutral graphene. The average of the position of the G peak and the 2D peak were all significantly upshifted as expected to compressive biaxial strain (Figure 20a,b). Using the value for the Raman G peak shift to the applied strain adapted from [62], the applied biaxial strain on monolayer/bilayer/trilayer graphene were -0.156%, -0.116% and -0.099%. On the other hand, by using the value of 2D peak shift to strain, $\partial\omega_{2D}/\partial\varepsilon \sim -160.3$, the applied biaxial strain on monolayer/bilayer/trilayer graphene were -0.167%, -0.075% and -0.059%. The discrepancy between the each estimation of biaxial strain is not known yet, but the charge doping on the graphene due to the charge transfer between the graphene/ Cu or spatially non-uniform strain might be responsible for the results, which will be discussed in the next section.

3.3 Estimation of charge doping on graphene

The shift of the Fermi energy in the graphene induces the change of Raman scattering. First, the phonon softening/stiffening by the non-adiabatic behavior shifts the G peak and the 2D peak frequency [48]. Second, the forbidden phonon decaying into an electron-hole pair due to Pauli exclusion principle sharpens the phonon linewidths [66]. The linewidth of the 2D peak is insensitive to the doping, while the linewidth of the G peak shows strong dependence on the carrier concentration[67,68]. Therefore, the charge doping on graphene can be estimated by either measuring shifts of the G peak and the 2D peak or measuring FWHM(G). Both methods will be discussed in this section.

First, the average of FWHM(G) was plotted to the number of the layers of graphene (Figure 21). The average FWHM (G) of monolayer was about 16 cm^{-1}. Comparing with the FWHM(G) of the charge neutral graphene ~ 14 cm^{-1}, the higher values of FWHM(G) can be interpreted as that the charge density of synthesized graphene on Cu is very low. The low charge doping on graphene can suggest the weak interaction between Cu and graphene in our system. This weak interaction between graphene is coherent to the first principle study, which has suggest the charge transfer between graphene and Cu causes a Fermi level upshift of graphene by 0.17 eV [69].

The reason of higher FWHM than neutral graphene was suggested that non-uniform strain can reside in graphene by the formation of the superlattice between the graphene and Cu [70]. The lattice mismatch between graphene and Cu(100) or

Cu(111) introduces non-uniform van der Waals interaction, so non-uniform biaxial strain can reside in graphene[71]. The slight broadening of FWHM(G) of our result can be interpreted as the small degree of non-uniformity in biaxial compressive strain. In addition, the FWHM(2D) of monolayer was about ~ 31 cm^{-1}, which is similar to the unstrained neutral graphene (~29 cm^{-1}). When the graphene is under uniaxial strain, the lattice symmetry breaking induces the change of the geometry of the Brillouin zone, so resonance (G peak) and double resonance process (2D peak) are split into two depends on the polarization direction of laser [57]. Therefore, negligible broadening of the G peak and the 2D peak in the monolayer region indicates the strain on graphene is almost biaxial strain.

For the bilayer graphene, the effect of charge doping on the G peak of graphene has been investigated [72-74]. Owing to the stacked geometry, non-equivalent charge doping on top layer and the bottom layer can induce the symmetry breaking, which can activate the additional G band mode [9]. There was no detectable G peak splitting in our result, so the possibility of inhomogeneous charge density between the top layer and the bottom layer was excluded. The FWHM(G) of the bilayer graphene decreases with increasing carrier concentration [73,74]. This result is due to the Pauli exclusion principle similar to the case of single layer graphene. Comparing with our result, average FWHM(G) of bilayer graphene was about 16 cm^{-1} (Figure 21). As similar to the monolayer graphene, the result can be interpreted as the charge doping on bilayer graphene is low. The FWHM(G) of the trilayer graphene was also about 16 cm^{-1} in average. The effect of carrier concentration on the G mode of trilayer graphene was also investigated,

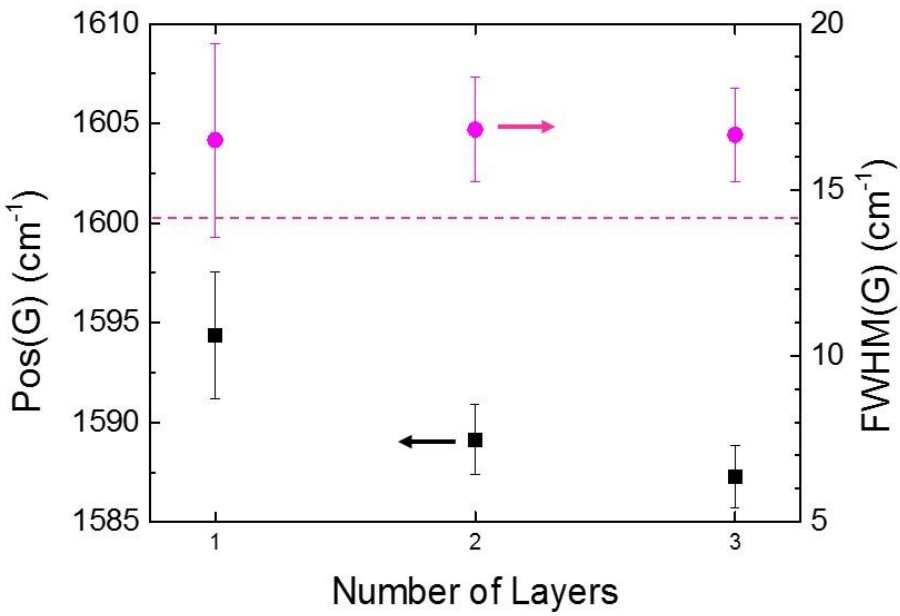

Figure 21 The position and the FWHM of the G peak. The position of the G peak was assigned as black square, and the FWHM of the G peak was assigned as magenta circle.

but the tendency of the G band linewidth is not reported [75]. Although the relation between carrier concentration and linewidth of the G mode in trilayer graphene is hard to find, the similar behavior to monolayer or bilayer graphene would be expected. Therefore, the charge density on the graphene can be determined as low in all points.

By estimating the linewidth of the G peak, the charge density on graphene was determined as very low. The Fermi level shift of the graphene also induces change of intensity of the G peak and the 2D peak. For graphene doped by electric field effect, the intensity ratio I(2D)/I(G) decreases within increasing carrier concentration [50]. This Raman peak intensity dependence of graphene on doping occurs due to electron-electron scattering [51]. For graphene with low Fermi energy ($E_F \ll 1$), the intensity of the 2D peak can be written as [51]

$$I(2D) = C(\gamma_K/\gamma)^2$$

$$\sqrt{1/I(2D)} = \frac{1}{\gamma_K\sqrt{C}}(\gamma_{ep} + f(\varepsilon)|E_F|)$$

where C is a constant, $\gamma = \gamma_{ep} + \gamma_{ee}$ and $\gamma_{ep} = \gamma_K + \gamma_\Gamma$ are the emission rate of the total scattering and the electron-phonon scattering. The $f(\varepsilon)$ is a function depends on the dielectric environment. Since I(G) is insensitive to the doping, I(G)/I(2D) can be used to derive γ_{ep}

$$\sqrt{I(G)/I(2D)} = C'(\gamma_{ep} + f(\varepsilon)|E_F|)$$

In our experiment, the dielectric environment is air ($\varepsilon = 1$), so using the equation and the relation for dimensionless Coulomb coupling constant $r = e^2/(\varepsilon v_F)$ from reference [51], $f \sim 0.11$. This relation is proved by the experiments in the low Fermi energy bound [51,52].

To determine the Fermi level of the monolayer graphene in sample, experimental relation between I(2D)/I(G) and carrier concentration from reference [75] was used. The I(2D)/(G) ratio was directly converted to the carrier concentration using the empirical data, and the carrier concentration was converted to Fermi energy by the relation [76,77]

$$E_F(n) = \hbar|v_F|\sqrt{\pi n}$$

where $|v_F| = 1.1 \times 10^6\ ms^{-1}$ is the Fermi velocity. The average Fermi energy of the monolayer was 0.34 eV $\pm$ 0.9 eV varied from ~0.14 eV to ~0.5 eV, which is corresponding to the carrier concentration of ~ 1.0 $\times$ 10^{12} cm^{-2} to ~ 1.5 $\times$ 10^{13} cm^{-2}. The result is consistent with the weak interaction between graphene and Cu. By converting the I(2D)/I(G) to Fermi energy, the map for monolayer graphene can be plotted to estimate the spatial variation of the charge doping on graphene monolayer (Figure 22). As clearly seen, the Fermi energy of monolayer graphene is varied in space, and the strongly doped domain is up to 1.5 μm.

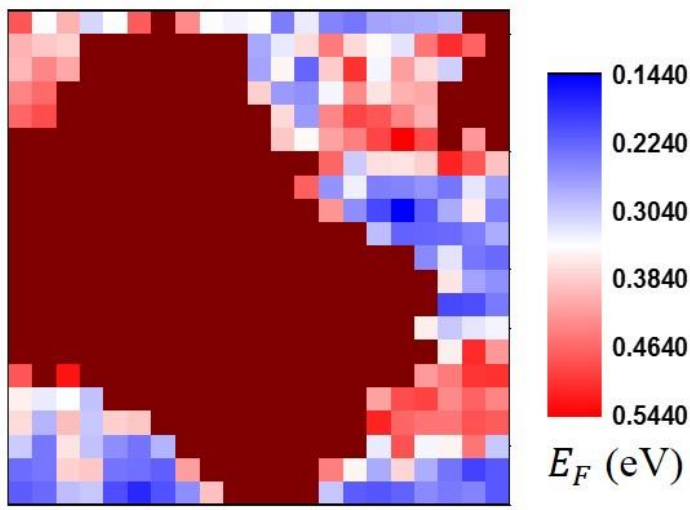

Figure 22 Fermi energy of the monolayer graphene. Data was converted from the I(G)/I(2D).

3.4 Separation of the strain from charge doping effect

The spatial map of the Fermi energy of monolayer graphene reveals the inhomogeneous charge density on graphene. However, since the peak intensity ratio I(2D)/I(G) decreases within increasing concentration of either electron or hole [50-52], so the exact doping type is hard to be derived from the Raman map. However, strain effects can be separated from charge doping effects. Both strain and charge doping on graphene can shift the G and 2D peak [50,62], but those effects can be separated by comparing the $\Delta\omega_G$ and $\Delta\omega_{2D}$ owing to the different peak shift behavior. Lee *et al*. separated the Raman peak shift to two components and successfully estimated the strain and charge doping on graphene [78]. Plotting $\Delta\omega_G$ - $\Delta\omega_{2D}$ graph with spatially resolved Raman data, we can see the distinguishing tendency of the peak position shift. We note that our data is well fitted with charge neutral line which has slope of 2.8. The value of $\Delta\omega_{2D}/\Delta\omega_G$ for strained graphene was reported previously, ranging 2.02 ~ 2.44 for uniaxially strained graphene [61,79,80] and 2.25 ~ 3.03 for biaxially strained graphene [61-64]. Because there are no noticeable Raman peak splitting in either G or 2D band, biaxial strain is dominant in our sample. This relation indicates the graphene lattice compression would be introduced after the Cu step formation. Since the wrinkle structure is aligned to the one direction, no noticeable uniaxial strain indicates that the periodic structure is not formed by stress release to specific direction. The graphene would be mainly compressed on the flat terrace of Cu.

Data collected from monolayer graphene is scattered above that of

bilayer/trilayer graphene, which indicates that monolayer graphene is more compressed than the bilayer and trilayer graphene. The data points are not exactly on the charge neutral line, but scattered to tight side of the line. This is due to the charge doping effects, which induce almost horizontal shift of the points in both n-type and p-type doping cases. The inhomogeneous doping effects on graphene would be induced by spatially different charge transfer between Cu and graphene which induces n-type doping [69,81], or adsorbents from ambient air which possibly induce p-type doping [82]. It is hard to distinguish exact type of doping, but we can separate the strain effect from the charge doping effect because 2D peak shifts more sensitively to the strain than doping effect.

Figure 23 shows compressive strain map converted from the Raman data. As inferred from the $\Delta\omega_G - \Delta\omega_{2D}$ plot, biaxial compressive strain on monolayer graphene was higher than those of bilayer/trilayer graphene, which is matched with the AFM image of Cu step edge. Biaxial strain varies -0.1 % ~ -0.2 % on monolayer graphene, -0.05 % ~ -0.1 % on bi/trilayer graphene. From the comparison between the compressive strain map in Fig. 4b and surface morphology in Fig. 1c, we notice that periodicity of the Cu step edges is related to the strain on graphene. Cu step edges were narrower under strongly compressed monolayer graphene, whereas Cu step edges were broadened under less compressed bilayer/trilayer graphene. The results suggest that periodicity of the Cu step edges are changed by the different degree of stress relaxation of graphene/Cu interface.

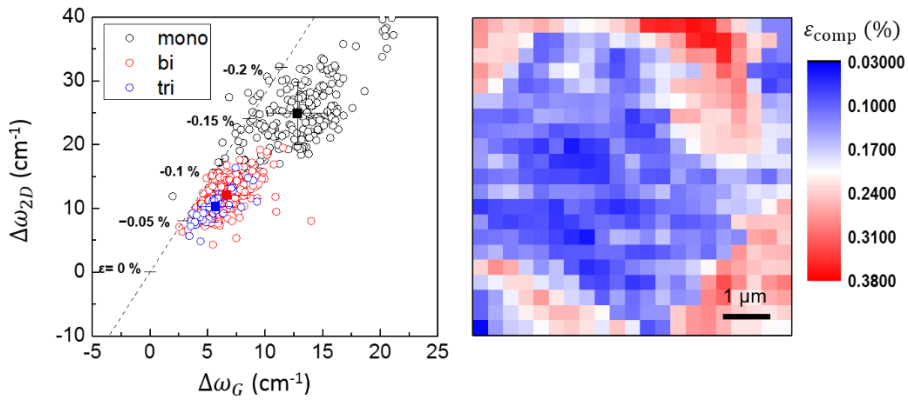

Figure 23 $\Delta\omega_G$-$\Delta\omega_{2D}$ correlation and compressive strain map. (a) $\Delta\omega_G$-$\Delta\omega_{2D}$ correlation of the monolayer/bilayer/trilayer graphene. Dashed line is charge neutral line which is assumed from the values of $\partial\omega_G/\partial\varepsilon$ ~ -57.3 and $\partial\omega_{2D}/\partial\varepsilon$ ~ -160.3 from the reference 62. (b) Compressive strain map converted from the spatially resolved Raman data.

The origin of the wrinkle-like periodic Cu step formation has been remained in question. In our observation, Cu steps were formed in one direction with periodicity, but biaxial strain on graphene cannot explain the dramatic transition of Cu step periodicity. Rather, by obtaining high-resolution topographic AFM image, Cu step termination at the boundary and distinguishing facet evolution under the bilayer graphene implies other effect. The reconstructed surface shows similar behavior observed by Wang *et al.*, which identical facets were exposed under the different graphene sheets in same Cu grain [43]. The surface reconstruction is a result of interface energy minimization of Cu/graphene during cooling started from the liquid-like premelted Cu surface layer at high temperature [42,43]. Although interaction between Cu and graphene shows very weak physisorption at room temperature [69], but interaction between Cu and graphene is important at high temperature [83]. Similarly, our observation would be interpreted as the result of the energy minimization at graphene/Cu interface during cooling, but graphene with different layer numbers gives which has different degree of interaction with Cu surface induces distinctive surface structure.

3.5 Conclusion

In summary, we study the effect of graphene layer numbers on Cu surface reconstruction. The AFM and Raman spectroscopy show that periodic ripple-like Cu step edge is formed under graphene, and its periodicity is noticeably increased under bilayer/trilayer graphene (trilayer > bilayer > monolayer). In addition,

Raman G and 2D peaks of graphene are generally less blue-shifted with increasing graphene layers, which indicates that graphene is more compressed with decreasing layer numbers. The results show that the Cu surface reconstruction under graphene is clearly affected by the different interaction between Cu and graphene layers.

References

[1] Neto, A. H. C.; Guinea, F.; Peres, N. M. R.; Novoselov, K. S.; Geim, A. K. *Rev. Mod. Phys.* **2009**, *81*, 109.

[2] Marder, M. P. *Condensed Matter Physics*, 2nd ed., Wiley, **2010**.

[3] S. Reich, J. Maultzsch, C. Thomsen and P. Ordejón, *Phys. Rev. B* **2002**, *66*, 035412.

[4] P. R. Wallace, *Phys. Rev.* **1947**, *71*, 622.

[5] Geim, A. K.; Novoselov, K. S. *Nat. Mater.* **2007**, *6*, 183.

[6] Berger, C.; Song, Z.; Li, T.; Li, X.; Ogbazghi, A. Y.; Feng, O.; Dai, Z.; Marchenkov, A. N.; Conrad, E. H., First, P. N.; de Heer, W. A. *J. Phys. Chem. B* **2004**, *108*, 19912.

[7] Rutter, G. M.; Crain, J. N.; Guisinger, N. P.; Li, T.; First, P. N.; Stroscio, J. A. *Science* **2007**, *317*, 219.

[8] Vaari, J.; Lahrinen, J.; Hautojärvi, P. *Catal. Lett.* **1997**, *44*, 43.

[9] Gamo, Y.; Nagashima, A.; Wakabayashi, M.; Terai, M.; Oshima, C. *Surf. Sci.***1997**, *374*, 61.

[10] Kawano, T.; Kawaguchi, M.; Okamoto, Y.; Enomoto, H.; Bando, H.; *Solid State Sci.* **2002**, *4*, 1521.

[11] Starodubov, A. G.; Medvetskii, M. A.; Shikin, A. M.; Adamchuk, V. K. *Phys.*

Solid State **2004**, *46*, 1340.

[12] Land, T. A.; Michely, T.; Behm, R. J.; Hemminger, J. C.; Comsa, G. *Surf. Sci.***1992**, 264, 261.

[13] Ueta, J.; Saida, M.; Nakai, C.; Yamada, Y.; Sasaki, M.; Yamamoto, S. *Surf. Sci.* **2004**, *560*, 183.

[14] Starr, D. E.; Pazhetnov, E. M.; Stadnichenko, A. I.; Boronin, A. I.; Shaikhutdinov, S. K. *Surf. Sci.* **2006**, *600*, 2688.

[15] Oshima, J.; Nagashima, A. *J. Phys.: Condens. Matter* **1997**, *9*, 1.

[16] Marchini, S.; Günther, S.; Wintterlin, J. *Phys. Rev. B* **2007**, *76*, 075429.

[17] de Parga, A. L. V.; Calleja, F.; Borca, B.; Passeggi, J. M. C. G.; Hinarejos, J. J.; Guinea, F.; Miranda, R. *Phys. Rev. Lett.* **2008**, *100*, 056807.

[18] Sutter, P. W.; Flege, J.-I.; Sutter, E. A. *Nat. Mater.* **2008**, *7*, 406.

[19] Gall, N. R.; Rutkov, E. V.; Tontegode, A. Y. *Phys. Solid State* **2004**, *46*, 371.

[20] N'Diaye, A. T.; Bleikamp, S.; Feibelman, P.; Michely, T. *Phys. Rev. Lett.* **2006**, *97*, 2315501.

[21] Makarenko, I. V.; Titkov, A. N.; Waqar, Z.; Dumas, P.; Rutkov, E. V.; Gall, N. R. *Phys. Solid State* **2007**, *49*, 371.

[22] Li, X.; Cai, W.; An, J.; Kim, S.; Nah, J.; Yang, D.; Piner, R.; Velamakanni, A.; Jung, I.; Tutuc, E.; Banerjee, S. K.; Colombo, L.; Ruoff, R. S. **2009**, *324*, 1312.

[23] Srivastava, A.; Galande, C.; Ci, L.; Song, L.; Rai, C.; Jariwala, D.; Kelly, K. F.; Ajayan, P. M. *Chem. Mater*. **2010**, *22*, 3457.

[24] Voloshina, E.; Dedkov, Y. *Phys. Chem. Chem. Phys.* **2012**, *14*, 13502.

[25] McCann, E. *Phys. Rev. B* **2006**, *74*, 161403.

[26] Novoselov, K. S.; Geim, A. K.; Morozov, S. V.; Jiang, D.; Katsnelson, M. I.; Grigorieva, I. V.; Dubonos, S. V.; Firsov, A. A. *Nature* **2005**, *438*, 197.

[27] Bolotin, K. I.; Sikes, K. J.; Jiang, Z.; Fudenberg, G.; Hone, J.; Kim, P.; Stormer, H. L. *Solid State Commun*. **2008**, *146*, 351.

[28] Sabio, J.; Seoanez, C.; Fratini, S.; Guinea, F.; Neto, A. H. C.; Sols, F. *Phys. Rev. B* **2008**, *77*, 235430.

[29] Leenaerts, O.; Partoens, B.; Peeters, F. M. *Phys. Rev. B* **2008**, *77*, 125416.

[30] Lee, E. J. H.; Balasubramanian, K.; Weitz, R. T.; Burghard, M.; Kern, K. *Nat. Nanotechnol.* **2008**, *3*, 486.

[31] Reina, A.; Jia, X.; Ho, J.; Nezich, D.; Son, H.; Bulovic, V.; Dresselhaus, M.; Kong, J. *Nano Lett.* **2009**, *9*, 30.

[32] Li, X.; Cai, W.; An, J.; Kim, S.; Nah, J.; Yang, D.; Piner, R.; Velamakanni, A.; Jung, I.; Tutuc, E.; Banerjee, S. K.; Colombo, L.; Ruoff, R. S. **2009**, *324*, 1312.

[33] Liu, N.; Fu, L.; Dai, B.; Yan, K.; Liu, X.; Zhao, R.; Zhang, Y.; Liu, Z. *Nano Lett.* **2011**, *11*, 297.

[34] Guinea, F.; Katsnelson, M. I.; Vozmediano, M. A. H. *Phys. Rev. B* **2008**, *77*,

075422.

[35] Obraztsov, A.; Obraztsova, E.; Tyurnina, A.; Zolutukhin, A. *Carbon* **2007**, *45*, 2017.

[36] Tian, J.; Cao, H.; Wu, W.; Yu, Q.; Guisinger, N. P.; Chen, Y. P. *Nano Lett.* **2012**, *12*, 3893.

[37] Hayashi, K.; Sato, S.; Yokoyama, N. *Nanotechnology* **2013**, *24*, 025603.

[38] Ni, G.-X.; Zheng, Y.; Bae, S.; Kim, H. R.; PAchoud, A.; Kim, Y. S.; Tan, C.-L.; Im, D.; Ahn, J.-H.; Hong, B. H.; Ö zyilmaz, B. *ACS Nano* **2012**, *6*, 1158.

[39] Liu, N.; Pan, Z.; Fu, L.; Zhang, C.; Dai, B.; Liu, Z. *Nano Res.* **2011**, *4*, 996.

[40] Pan, Z.; Liu, N.; Fu, L.; Liu, Z. *J. Am. Chem. Soc.* **2011**, *133*, 17578.

[41] Paronyan, T. M.; Pigos, E. M.; Chen, G.; Harutyunyan, A. R. *ACS Nano* **2011**, *5*, 9619.

[42] Kim, D. W.; Lee, J.; Kim, S. J.; Jeon, S.; Jung, H.-T. *J. Mater Chem. C* **2013**, *1*, 7819.

[43] Wang, Z.-J.; Weinberg, G.; Zhang, Q.; Lunkenbein, T.; Klein-Hoffmann, A.; Kurnatowska, M.; Plodinec, M.; Li, Q.; Chi, L.; Schloegl, R.; Willinger, M.-G. *ACS Nano* **2015**, *9*, 1506.

[44] Malard, L. M.; Pimenta, M. A.; Dresselhaus, G.; Dresselhaus, M. S. *Phys. Rep.* **2009**, *473*, 51.

[45] Beams, R.; Cançado, L. G.; Novotny, L. *J. Phys.: Condens. Matter* **2015**, *27*,

083002.

[46] Park, J. S.; Cecco, A. R.; Saito, R.; Jiang, J.; Dresselhaus, G.; Dresselhaus, M. S. *Carbon* **2009**, *47*, 1303.

[47] Ferrari, A. C.; Meyer, J. C.; Scardaci, V.; Casiraghi, C.; Lazzeri, M.; Mauri, F.; Piscanec, S.; Jiang, D.; Novoselov, K. S.; Roth, S.; Geim, A. K. *Phys. Rev. Lett.* **2006**, *97*, 187401.

[48] Pisana, S.; Lazzeri, M; Casiraghi, C.; Novoselov, K. S.; Geim, A. K.; Ferrari, A. C.; Mauri, F. *Nat. Mater.* **2007**, *6*, 198.

[49] Lazzeri, M.; Mauri, F. *Phys. Rev. Lett.* **2006**, *97*, 266407.

[50] Das, A.; Pisana, S.; Charkraborty, B.; Piscanec, S.; Saha, S. K.; Waghmare, U. V.; Novoselov, K. S.; Krishnamurthy, H. R.; Geim, A. K.; Ferrari, A. C.; Sood, A. K. *Nat. Nanotechnol.* **2008**, *3*, 210.

[51] Basko, D. M.; Piscanec, S.; Ferrari, A. C. *Phys. Rev. B* **2009**, *80*, 165413.

[52] Casiraghi, C. *Phys. Rev. B* **2009**, *80*, 233407.

[53] Li, X.; Magnusoin, C. W.; Venugopal, A.; Tromp, R. M.; Hannon, J. B.; Vogel, E. M.; Colombo, L.; Ruoff, R. S. *J. Am. Chem. Soc.* **2011**, *133*, 2816.

[54] Havener, R. W.; Zhuang, H.; Brown, L.; Hennig, R.; Park, J. *Nano Lett.* **2012**, *12*, 3162.

[55] Wofford, J. M.; Nie, S.; McCarty, K. F.; Bartelt, N. C.; Dubon, O. D. *Nano Lett.* **2010**, *10*, 4890-4896.

[56] Zhang, Y.; Gao, T.; Gao, Y.; Xie, S.; Ji, Q.; Yan, K.; Peng, H.; Liu, Z. *ACS Nano* **2011**, *5*, 4014-4022.

[57] Frank, O.; Mohr, M.; Maultzsch, J.; Thomsen, C.; Riaz, I.; Jalil, R.; Novoselov, K. S.; Tsoukleri, G.; Parthenios, J.; Papagelis, K.; Kavan, L.; Galiotis, C. *ACS Nano* **2011**, *5*, 2231.

[58] Jian, J.-W.; Wang, J.-S.; Li, B. *Phys. Rev. B* **2009**, *80*, 205429.

[59] Nix, F. C.; MacNair, D. *Phys. Rev.* **1941**, *60*, 597.

[60] Yu, V.; Whiteway, E.; Maassen, J.; Hilke, M. *Phys. Rev. B* **2011**, *84*, 205407.

[61] Mohiuddin, T. M. G.; Lombardo, A.; Nair, R. R.; Bonetti, A.; Savini, G.; Jalil, R.; Bonini, N.; Basko, D. M.; Galiotis, C.; Marzari, N.; Novoselov, K. S.; Geim, A. K.; Ferrari, A. C. *Phys. Rev. B* **2009**, *79*, 205433.

[62] Ding, F.; Ji, H.; Chen, Y.; Herklotz, A.; Dörr, K.; Mei, Y.; Rastelli, A.; Schmidt, I. G. *Nano Lett.*, **2010**, *10*, 3453.

[63] Metzger, C.; Rémi, S.; Liu, M.; Kusminskiy, S. V.; Neto, A. H. C.; Swan, A. K.; Goldberg, B. B. *Nano Lett.* **2010**, *10*, 6.

[64] Zabel, J.; R. R. Nair,; Ott, A.; Gerogiu, T.; Geim, A. K.; Novoselov, K. S.; Casiraghi, C. *Nano Lett.* **2012**, *12*, 617.

[65] Graf, D.; Molitor, F.; Ensslin, K.; Stampfer, C.; Jungen, A.; Hierold, C.; Wirtz, L. *Nano Lett.* **2007**, *7*, 238.

[66] Lazzeri, M.; Piscanec, S.; Mauri, F.; Ferrari, A. C.; Robertson, J. *Phys. Rev. B*

2006, *73*, 155426.

[67] Yan, J.; Zhang, Y.; Kim, P.; Pinczuk, A. *Phys. Rev. Lett.* **2007**, *98*, 166802.

[68] Stampfer, C.; Molitor, F.; Graf, D.; Ensslin, K.; Jungen, A.; Hierold, C.; Wirtz, L. *Appl. Phys. Lett.* **2007**, *97*, 241907.

[69] Khomyakov, P. A.; Giovannetti, G.; Rusu, P. C.; Brocks, G.; van den Brink, J.; Kelly, P. J. *Phys. Rev. B* **2009**, *79*, 195425.

[70] He, R.; Zhao, L.; Petrone, N.; Kim, K. S.; Roth, M.; Hone, J.; Kim, P.; Pasupathy, A.; Pinczuk, A. *Nano Lett.* **2012**, *12*, 2408.

[71] Aitken, Z. H.; Huang, R. *J. Appl. Phys.* **2010**, *107*, 123531

[72] Malard, L. M.; Elias, D. C.; Alves, E. S.; Pimenta, M. A. *Phys. Rev. Lett.* **2008**, *101*, 257401.

[73] Yan, J.; Henriksen, E. A.; Kim, P.; Pinczuk, A. *Phys. Rev. Lett.* **2008**, *101*, 136804.

[74] Das, A.; Chakraborty, B.; Piscanec, S.; Pisana, S.; Sood, A. K.; Ferrari, A. C. *Phys. Rev. B* **2009**, *79*, 155417.

[75] Lui, C. H.; Cappelluti, E.; Li, Z.; Heinz, T. F. *Phys. Rev. Lett.* **2013**, *110*, 185504.

[76] Novoselov, K. S.; Geim, A. K.; Morozov, S. V.; Jiang, D.; Katsnelson, M. I.; Grigorieva, I. V.; Dubonos, S. V.; Firsov, A. A. *Nature* **2005**, *438*, 197.

[77] Zhang, Y.; Tan, Y.-W.; Stormer, H. L.; Kim, P. *Nature* **2005**, *438*, 201.

[78] Lee, J. E.; Ahn, G.; Shim, J.; Lee, Y. S.; Ryu, S. *Nat. Commun.* **2012**, *3*, 1024.

[79] Huang, M.; Yan, H.; Chen, C.; Song, D.; Heinz, T. F.; Hone, J. *Proc. Natl. Acad. Sci. USA* **2009**, *106*, 7304.

[80] Yoon, D.; Son, Y. W.; Cheong, H. *Phys. Rev. Lett.* **2011**, *106*, 155502.

[81] Zheng, J.; Wang, Y.; Wang, L.; Quhe, R.; Ni, Z.; Mei, W.-N.; Gao, Z.; Yu, D.; Shi, J.; Lu, J. *Sci. Rep.* **2013**, *3*, 2081.

[82] Li, Z.; Wang, Y.; Kozbial, A.; Shenoy, G.; Zhou, F.; McGinley, R.; Ireland, P.; Morganstein, B.; Kunkel, A.; Surwade, S. P.; Li, L.; Liu, J. *Nat. Mater.* **2013**, *12*, 925.

[83] Wood, J. D.; Schmucker, S. W.; Lyons, A. S.; Pop, E.; Lyding, J. W. *Nano Lett.* **2011**, *11*, 4547.

국문 초록

화학 기상 증착법 (chemical vapor deposition)을 이용하여 그래핀을 구리 표면에 합성하게 되면 구리의 표면 형상이 변화하게 된다. 이러한 현상은 구리와 그래핀의 열팽창 계수가 다르기 때문이라고 알려져 있지만 그래핀이 구리 표면의 재구성에 대하여 어떠한 관계를 가지고 있는지에 대해서는 아직 밝혀지지 않고 있다. 본 논문에서는 화학 기상 증착법으로 가스 유량과 합성시간 등을 조절하여 다른 층수의 그래핀을 구리 표면에 합성하였다. 원자 힘 현미경 (atomic force microscopy) 이미지와 그래핀의 라만 분광 신호를 분석한 결과 구리 표면의 계단형 모서리들이 그래핀의 층수가 증가할수록 확연하게 증가하는 것을 확인할 수 있었다. 더 나아가 라만 G, 2D 피크의 변화를 통해 단층 그래핀의 압축 변형도가 이중층, 삼중층 그래핀 보다 높다는 것을 밝혀내었다. 이러한 결과들은 그래핀의 층수가 구리 표면 형상의 재구성에 대해 큰 영향을 가진다는 것을 제안한다.

주요어: 그래핀, 표면 재구성, 원자힘 현미경, 라만 분광법

학 번: 2013-20251